Quantitative Scanning Transmission Electron Microscopy of Electronic and Nanostructured Materials

By
Andrew B. Yankovich

A dissertation submitted in partial fulfillment of the requirements for the degree of

Doctor of Philosophy
(Materials Science)

at the
University of Wisconsin – Madison
2015

Date of final oral examination: May 7th 2015

This dissertation is approved by the following members of the Final Oral Committee:
Paul M. Voyles, Professor, Materials Science and Engineering
Dane Morgan, Professor, Materials Science and Engineering
Thomas Kuech, Professor, Chemical and Biological Engineering
Huifang Xu, Associate Professor, Geology
Xudong Wang, Associate Professor, Materials Science and Engineering

Table of Contents:

Acknowledgments		iii
Abstract		v
Chapter 1	Introduction	1
Chapter 2	Characterization Techniques	5
2.1	Introduction	5
2.2	TEM Specimen Preparation	5
2.3	High-Resolution TEM	6
2.4.	Aberration-corrected STEM Imaging	7
2.5	Position Averaged Convergent Beam Electron Diffraction	16
2.6	Frozen Phonon Multislice Simulations	17
2.7	EDS Spectrum Imaging	18
2.8	Electron Energy Loss Spectroscopy	19
Chapter 3	Ga-doped ZnO Thin Films	22
3.1	Introduction	22
3.2	Material Synthesis	24
3.3	Procedures	25
3.4	Defects in Ga-doped ZnO Thin Films	26
3.5	Conclusions	40
Chapter 4	Sb-doped ZnO Nanowires	43
4.1	Introduction	43
4.2	Material Synthesis	50
4.3	Procedures	50
4.4	Defects Responsible for *p*-type Conduction in ZnO NWs	51
4.5	Conclusions	62
Chapter 5	Composition Variation in InGaN Quantum Well LEDs	63
5.1	Introduction	63
5.2	Material Synthesis	64
5.3	Procedures	65
5.4	In Composition Variation in InGaN QW LED Structures	66
5.5	Conclusions	74
Chapter 6	Extended Defects in InGaN Quantum Well LEDs	76
6.1	Introduction	76
6.2	Material Synthesis	77
6.3	Procedures	78
6.4	Void Defect in InGaN and GaN	79
6.5	Conclusions	89
Chapter 7	Non-Rigid Registration and Image Analysis Tools	90
7.1	Introduction	90
7.2	Non-Rigid Registration Technique	92
7.3	Validation of Non-Rigid Registration on Simulated STEM Data	95
7.4	Image Analysis Tools Development	98

Chapter 8	High Precision Imaging of Single Crystal Materials	100
8.1	Introduction	100
8.2	Material Synthesis	101
8.3	Sub-pm Precision Imaging of Single Crystal GaN and Si	102
8.4	Dynamic Scattering Limits to Precision in HAADF & ABF STEM Images	111
8.5	Conclusions	122
Chapter 9	Surface Atom Bond Length Variation and 3D Structure Determination of Pt and Au Nanoparticles	123
9.1	Introduction	123
9.2	Material Synthesis	126
9.3	Pt Nanocatalyst Atomic Surface Structure	126
9.4	Au Nanoparticle Atomic Surface Structure	136
9.5	Conclusions	141
Chapter 10	Atomic Resolution EDX on Ca-doped $NdTiO_3$	143
10.1	Introduction	143
10.2	Material Synthesis	147
10.3	NRR of EDS Spectrum Images	147
10.4	Conclusions	154
Appendix 1: Wedge Polishing Manual		156
Appendix 2: NRR and Quantitative STEM Manual		159
References		166

Acknowledgments:

I cannot take credit for all the work presented in this dissertation. It is a product of many brilliant people who I have collaborated with, worked alongside, and been instructed by over the course of my Ph.D. studies. I cannot give enough thanks to those people who have supported me along my Ph.D. journey, both professionally and personally. Notable acknowledgements are:

1) My research and academic adviser, Paul M. Voyles, for his patience and passion for teaching. I cannot thank you enough for providing me with this opportunity.
2) All the collaborators I have had the pleasure to work with and learn from. Xing Li, Fan Zhang, Vitaliy Avrutin, Huiyong Liu, Natalia Izyumskaya, Ümit Özgür, and Hadis Morkoç from Virginia Commonwealth University. Steven Bradley and Sergio Sanchez from UOP Honeywell. Benjamin Berkels, Niklas Mevenkamp, Wolfgang Dahmen, and Peter Binev from the University of South Carolina and Germany. Thomas Slater and Sarah Haigh from the University of Manchester in the United Kingdom. Fei Wang, Brian Puchala, Ao Li, Min Yu, Jie Feng, Alex Kvit, Izabela Szlufarska, Dane Morgan, and Xudong Wang from the University of Wisconsin-Madison.
3) Professors Dane Morgan, Thomas Kuech, Xudong Wang, and Huifang Xu for serving on my Ph.D. committee. Thank you for providing valuable discussions, constructive criticism, and positive attitudes.
4) The UW-Madison Materials Science Center instrument support staff. Especially Alex Kvit, for providing me many hours of instrument training, discussions, and

collaborative research.

5) All the past and present Voyles Group members for your insightful comments, questions, training, and help. This includes Jinwoo Hwang, Feng Yi, Dylan Schweiss, Fengyuan Shi, Eric Cambell, Derek Landwehr, Michael Lee, Alex Gunstensen, Max Burton, Li He, Pei Zhang, Zhai Yizhang, Jason Maldonis, Congli Sun, Ashutosh Rath, Min Yu, Chenyu Zhang, Jie Feng, Xing Wang, and Sachin Muley.
6) Diana Rhoads, for all your behind the scenes efforts in keeping the program running smoothly. Your help is very much appreciated.
7) My friends, for always giving me things to do when I needed to get my mind off of my studies. Thank you for the relentless and morale-boosting support.
8) My girlfriend and partner, Teaona Hasbrouck. Thank you for putting up with my Ph.D. dreams and making sacrifices for me. I truly appreciate all that you do for me. I love you.
9) My family. This thesis would not have been possible without everything you have taught me. Thank you for all of the years filled with never ending support, love, and guidance.
10) Last but not least, the United States Department of Energy for your financial support during my graduate studies. (DE-FG02-08ER46547)

Abstract:

This thesis reports studies of electronic and nanostructured materials by advanced electron microscopy (EM) techniques, including scanning transmission electron microscopy (STEM), position averaged convergent beam electron diffraction (PACBED), X-ray energy dispersive spectroscopy (EDS), and electron energy loss spectroscopy (EELS). This work enhanced the understanding of the microstructure, defects, and composition of Ga-doped ZnO thin films, Sb-doped ZnO nanowires, and InGaN quantum well (QW) based light emitting diode (LED) structures, and helped develop structure – property relationships for these materials. A new technique, non-rigid registration of STEM images, was developed and applied to make high-precision measurements of the atomic structure of Pt nanocatalysts and Au nanoparticles, and to improve the quality of STEM EDS spectrum images.

ZnO is the first major topic. Ga-doped ZnO is a candidate transparent conducting oxide material. The microstructure of GZO thin films grown by molecular beam epitaxy under metal-rich conditions on sapphire, O-rich conditions on sapphire, and metal-rich conditions on GaN were examined using various EM techniques. The microstructure, prevalent defects, and polarity in these films strongly depend on the growth conditions and substrate. In ZnO nanowires, collaborators have demonstrated the first stable *p*-type ZnO using Sb doping. Using Z-contrast STEM, we showed that an unusual microstructure of Sb-decorated head-to-head inversion domain boundaries and internal voids contain all the Sb in the nanowires and cause the *p*-type conduction.

InGaN thin films and InGaN / GaN quantum wells (QW) for light emitting diodes are the second major topic. Low-dose Z-contrast STEM, PACBED, and EDS on InGaN QW LED structures grown by metal organic chemical vapor phase deposition show no evidence for nanoscale composition variations, contradicting previous reports. However, a new extended defect in GaN and InGaN was discovered. The defect consists of a faceted pyramid-shaped void that produces a threading dislocation along the [0001] growth direction, and is likely caused by carbon contamination during growth.

Non-rigid registration and high-precision STEM of nanoparticles is the final topic. Non-rigid registration (NRR) is a new image processing technique that corrects distortions arising from the serial nature of STEM acquisition that previously limited the precision of locating atomic columns and counting the number of atoms in each column in STEM images. NRR was used to demonstrate sub-picometer precision in STEM images of single crystal Si and GaN, the best reported in EM. NRR was then used to measure the atomic surface structure of Pt nanoacatalysts and Au nanoparticles which revealed new bond length variation phenomenon of surface atoms. In addition, NRR allowed for measuring the 3D atomic structure of the nanoparticles with less than 1 atom uncertainty, a long standing problem in electron microscopy. Finally, NRR was adapted to EDS spectrum images, significantly enhancing the signal to noise ratio and resolution of an EDS spectrum image of Ca-doped $NdTiO_3$ compared to conventional methods.

Chapter 1: Introduction

An increasing number of technologies rely on the atomic-scale control of materials enabled by advances in materials science and engineering. Examples of this include controlling the structure of nanomaterial surfaces and defects(*1*), atomically abrupt interfaces(*2*), and point defects(*3*). Atomic-scale material structures can only be understood and controlled if they can be accurately characterized, highlighting the importance for the development of accurate, atomic-scale characterization techniques. Transmission electron microscopy (TEM) and scanning transmission electron microscopy (STEM) have been used for over a half a century for materials characterization(*4–8*) and are currently at the forefront of atomic-scale structural and chemical characterization in crystalline materials. The recent commercialization of aberration-correctors (AC) for TEM and STEM instruments has shown the world previously unattainable views of the structure and composition of materials by making <1 Å image resolution and single-atom sensitivity regularly achievable(*9–16*), and 0.5 Å spatial resolution possible(*17*).

Chapters 3 through 6 of this dissertation discuss the use of various TEM and STEM techniques (introduced in Chapter 2) to characterize defects and composition variation in materials used in optoelectronic applications. They also include discussion of how the measured structures affect the material's properties. Understanding and controlling crystallographic defects is a cornerstone in semiconductor materials science and engineering because defects provide major contributions to the electronic and optical behavior of crystalline semiconductors. These 3-D, 2-D, 1-D, and point defects can be detrimental to a material's properties, causing efforts to eliminate them, or they can be

beneficial, causing efforts to introduce them with desired concentrations using the easiest and cheapest method possible. For example, semiconductor doping introduces impurity atoms into the material host lattice, creating point defects that can stay isolated, cluster together, or segregate at other larger defects, interfaces, or surfaces, all of which can alter the materials electronic, optical, and conduction properties differently. Chapter 3 reviews the use of TEM and STEM to characterize Ga-doped ZnO thin films that show promise for transparent conducting oxide applications. Chapter 4 discusses the long-standing problem of making ZnO display *p*-type conduction and shows how *p*-type ZnO can be realized by Sb-doping ZnO nanowire structures. Chapter 5 discusses how composition variation in InGaN quantum well (QW) light emitting diodes (LEDs) can affect the efficiency of the devices, and shows experimental TEM and STEM data supporting various compositional variations in InGaN quantum wells. Chapter 6 discusses crystallographic defects present in GaN and InGaN QW structures, and the discovery of a new 3-D nano-sized pyramid void defect in GaN and InGaN that hinders LED performance.

Thanks to improved electron optics, the quality of the information accessed by AC-TEMs and STEMs is often limited by experimental and environmental factors, and not by imperfections or shortcomings of the instrument. However, collecting and processing data using novel techniques from data science can help overcome these limitations, opening the door to new atomic-scale materials information. STEM is widely used over TEM because of its well-established interpretability, quantifiability, and analytical capability(*18*), but it has three notable limitations (amongst a larger list) caused

by environmental factors. First, the spatial precision of STEM is inherently worse than that of TEM and is not good enough to observe pm-scale atom displacements. Second, it is difficult to resolve structural information along the electron beam direction through the material to give 3D material information, due to the projection nature of TEM/STEM images. Third, the long dwell times required for STEM energy dispersive spectroscopy (EDS) composition mapping combined with environmental instabilities reduce the quality of atomic-scale EDS composition data. These three limitations can be overcome by using a new non-rigid registration (NRR) technique I collaborated on developing, as discussed in Chapters 7 through 10.

Chapter 7 reviews the development and application of NR registration for STEM images to enable extremely high signal to noise ratio (SNR) STEM images that are free of image distortions caused by environmental instabilities. Chapter 7 also summarizes the development of image analysis tools that allow for extraction of quantitative information from atomic-resolution STEM images. Chapter 8 shows that NRR allows for sub-picometer spatial precision in STEM images of single crystal materials, the best reported for any electron microscopy technique. Chapter 9 discusses the use of NR registration to measure pm-scale bond length variations of surface atoms on a Pt nanocatalyst and Au nanoparticle, providing high precision surface structure information that is important in understanding catalyst active sites. In addition, Chapter 9 demonstrates that NR registration allows the determination of 3D atomic structure information using the standardless atom counting(*19*) with better uncertainty than previously allowed. In theory, unique atom counting is now possible using NR

registration and standardless atom counting, but experimental limitations, such as sample preparation artifacts, make this challenging. Chapter 10 shows that EDS spectrum image quality is significantly improved by using NRR compared to two other common acquisition techniques. NRR reduces the spatial distortions present in spectrum images and improves atomic column contrast and resolution.

Chapter 2: Characterization Techniques

2.1. Introduction

Various transmission electron microscopy (TEM) techniques served as my platform to characterize the structure of materials. This chapter introduces these various techniques to provide background about the techniques' basic physics, general limitations, and important considerations. TEM utilizes a controlled electron beam with a velocity larger than half the speed of light that is transmitted through an electron transparent sample. The electron beam interacts with the sample, producing different types of scattering events and signals that can be collected using various detectors. Primarily, the transmitted electrons and the excited x-rays are used to create images, diffraction patterns, and characteristic energy spectra that are widely useful in materials science research. The TEM toolbox provides many different characterization techniques, and the research presented in this thesis utilized the following techniques discussed in the following sections: TEM specimen preparation, high resolution TEM (HRTEM), aberration-corrected (AC) scanning transmission electron microscopy (STEM), position averaged convergent beam electron diffraction (PACBED), frozen phonon multislice simulations, STEM x-ray energy dispersive spectroscopy (EDS) spectrum imaging, and STEM electron energy loss spectroscopy (EELS).

2.2. TEM Specimen Preparation

The primary technique for sample preparation of thin film and bulk single crystal TEM samples was wedge polishing using the MultiPrep polishing system made by Allied

High Tech Products Inc. The general instructions for this technique are as listed in Appendix 1.

Depending on material hardness, the desired weight setting of the polishing head will vary. Harder materials require more weight, and as the procedure progresses for polishing each side, the weight should be decreased. The weight at the last step should be near 0. After wedge polishing, samples were usually ion milled in a Fischione 1010 ion mill and then a Fischione NanoMill for final thinning and cleaning. The parameters for ion milling are giving in each chapter because each material system required different ion milling conditions.

2.3. High Resolution Transmission Electron Microscopy

High Resolution TEM (HRTEM) utilizes the interference of excited Bragg diffraction beams and the transmitted beam to create coherent phase contrast images(*20*, *21*). HRTEM is widely used for materials research of thin films(*22*), nanostructures(*23*, *24*), and bulk samples to provide information about sample morphology, composition, interface structure, and defect structure from the micron down to the atomic scale(*25*, *26*).

Bright field TEM (BFTEM) allows for atomically resolved images, but interpreting the images is not simple due to image contrast reversals caused by sample thickness changes and dynamical scattering. As discussed in Chapter 2.4, this is one disadvantage of HRTEM compared to HRSTEM. Dark field (DF) TEM allows for images that are only produced using specific diffracted beams. This helps identify which areas of an image are produced by certain features in the diffraction pattern, for example

with grain orientation and phase mapping. Because HRTEM relies on coherent phase contrast, it is beneficial for determining different microstructural features including extended defect. The work presented here primarily utilized BF and DF HRTEM for determining the epitaxial relationships between thin films and substrates, phase identification, and extended defect identification.

2.4 Aberration-corrected STEM Imaging

Atomic-resolution scanning transmission electron microscopy (STEM) utilizes a focused electron probe (typically 20-25 mrad convergence semi-angle) smaller than the distance between atoms with a current large enough to produce meaningful signal at high angles in the diffraction plane. The STEM image is produced by scanning the probe across an electron transparent sample, causing scattering of electrons to all angles in the diffraction plane and creating a convergent beam electron diffraction (CBED) pattern. Electrons are integrated over a certain region in the CBED pattern to give the intensity in one image pixel, therefore producing an incoherent image(*27*).

Integrating the electrons incident in different regions in the diffraction pattern gives rise to different STEM imaging techniques. The techniques used in this research are high angle annular dark field (HAADF), medium angle annular dark field (MAADF), and annular bright field (ABF) STEM. Figure 2.1 shows a simulated Si [111] CBED pattern using an 8 mrad semi-convergence angle probe(*28*). Superimposed over the CBED pattern are three detector ranges that represent the HAADF (green), MAADF (blue), and ABF (red) detectors.

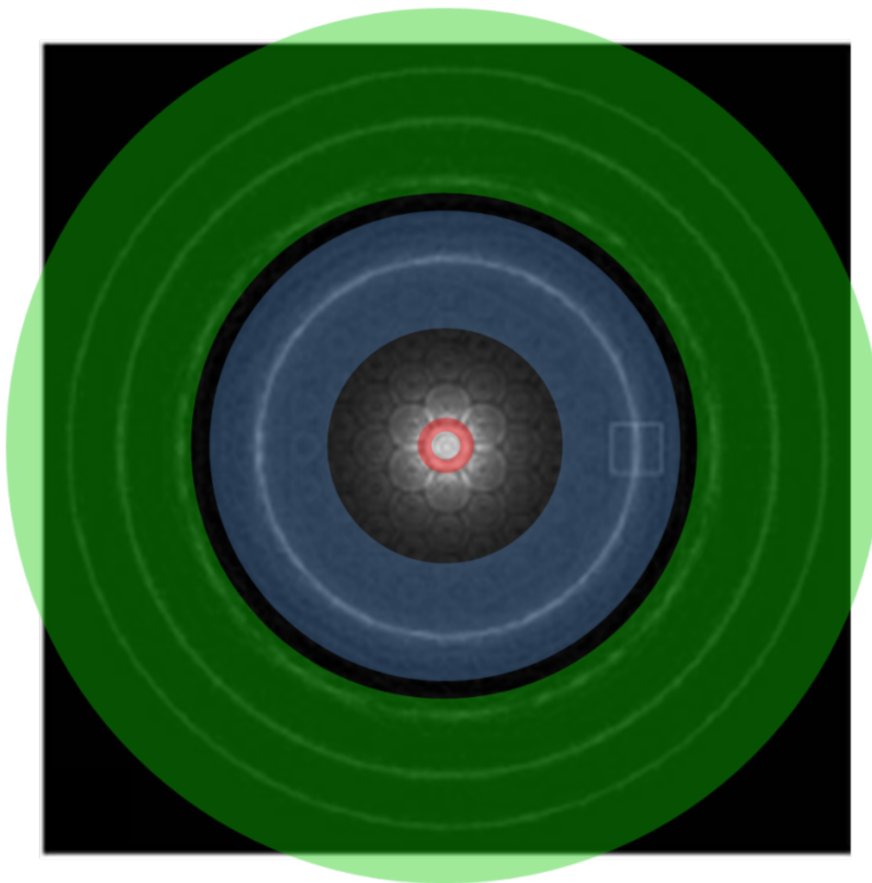

Figure 2.1: A multislice simulated Si [111] CBED pattern using an 8 mrad sem convergence angle probe(*28*). Superimposed over the CBED pattern are three detect ranges used for HAADF (green), MAADF (blue), and ABF (red) STEM.

Electrons that are collected by the HAADF detector in the regions of the CBED pattern outside the zero order Laue zone (typically >54 to 270 mrad) produce a signal that depends strongly on the atomic number (Z) of the atoms under the electron beam and give this technique its name, Z-contrast imaging(*29*). In the simplest model, the intensity is proportional to Z^{α}, where α is in the range 1.6 - 1.9 and Z is the atomic number of the atoms under the beam(*30*), but in real experiments this is modified by dynamical diffraction(*31*) and strain(*32*). The divergence of HAADF STEM imaging from normal

Z-contrast due to specimen strain is displayed in Figure 2.2. Figure 2.2 shows annular dark field STEM images of InGaN quantum wells in GaN with a top layer of Ga-doped ZnO acquired using various annular detector angles, with the detector inner angle displayed on each image. Figure 2.2(e) shows the STEM image produced using the most common HAADF detector angles does not display the predicted Z-contrast. The top Ga-doped ZnO layer should have a lower intensity than the GaN if this image were purely Z-contrast. Because there are various defects causing strain contrast in the Ga-doped ZnO, the layer appears brighter than the GaN. To achieve true Z-contrast with this sample, a detector angle as large as 143 mrad must be used to suppress the strain contrast. The scattering mechanisms responsible for the HAADF signal are elastic nuclear scattering and thermal diffuse scattering (TDS)(*30*).

Unlike conventional TEM, HAADF STEM has the advantage of being easily interpretable by giving a faithful representation of the sample structure that is preserved over a wide range of TEM sample thickness and defocus. However, HAADF STEM has two notable disadvantages compared to conventional TEM. First, when using multi-component samples with a large atomic number difference between constituents, the lighter elements are often invisible because the heavier atoms dominate the scattered intensity at large angles. Second, due to the serial acquisition nature of STEM imaging, instrument and environmental instabilities increase image distortions compared to the parallel acquisition of conventional TEM, causing an inherent disadvantage in image spatial precision.

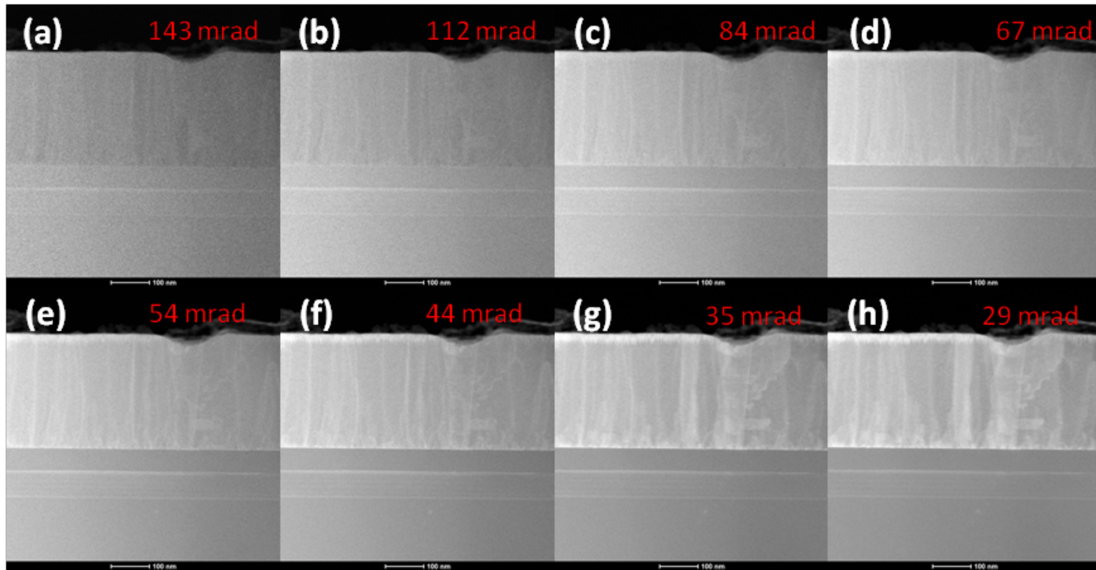

Figure 2.2: ADF STEM image of InGaN QWs in GaN with a top Ga-doped ZnO layer acquired using various detector angles. The detector inner angle is displayed on each Figure. With this material system, the normal HAADF detector angles (e) do not show pure Z-contrast because the Ga-doped ZnO appears brighter than GaN. To suppress the strain contrast in the Ga-doped ZnO enough to get true Z-contrast, a detector inner angle of 143 mrad (a) must be used.

Electrons that are collected at angles inside the HAADF region and outside the bright field disc in the diffraction pattern center (zero order Laue zone dark field) produce MAADF images, which enhance diffraction contrast and emphasize sample strain. This strain enhancement is displayed by the grain boundaries and other extended defects in Figures 2.2 (f)-(h). The scattering mechanism responsible for MAADF STEM is primarily elastic Bragg scattering, but if the sample is thick enough, inelastic TDS can contribute.

ABF STEM is a recently developed imaging technique where only electrons in the outer annular region of the bright field disc (typically 11 to 24 mrad) are

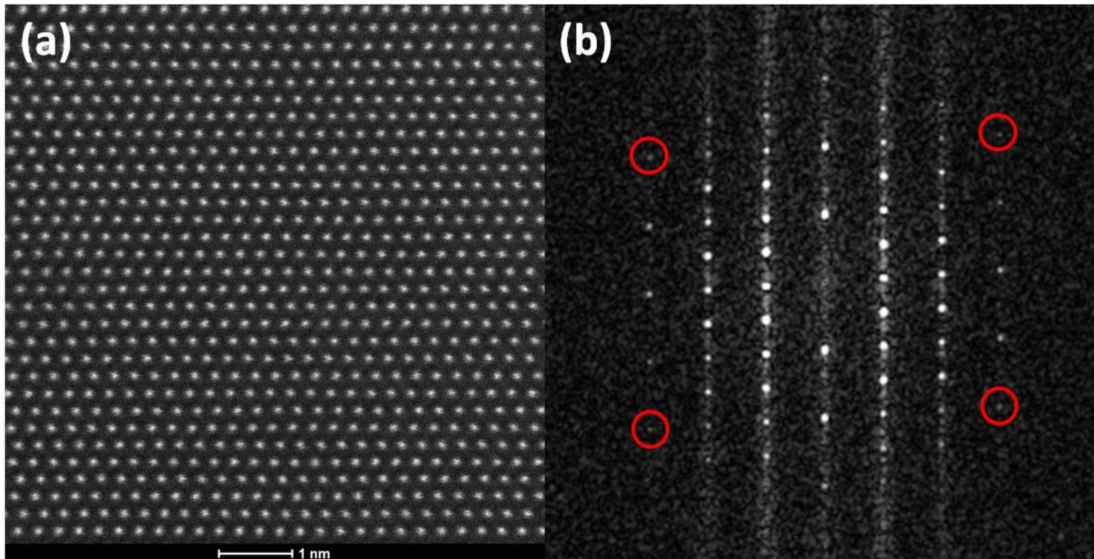

Figure 2.3: (a) A HAADF STEM image of GaN. (b) Fourier transform of the image in (a) showing that spatial frequencies of 1.35 $Å^{-1}$ are present (circled), which means the STEM image has a resolution down to 0.74 Å.

collected(*33–37*). In this region, elastically Bragg scattered electrons dominate image formation, although TDS does contribute slightly and should be considered if images are to be analyzed quantitatively. ABF STEM allows for the detection of light and heavy elements in the same image like in bright field STEM, but generally preserves the interpretability over thickness and defocus like Z-contrast STEM imaging. Because ABF and HAADF can be acquired simultaneously, it helps ease the first disadvantage of HAADF STEM mentioned above.

All electromagnetic lenses have unavoidable aberrations that distort the electron beam and reduce the achievable resolution. Two aberrations in STEM that are most important are chromatic (C_C) and spherical (C_S) aberrations. The unequal focusing of electrons with different energies by the lenses creates C_C. C_S is created by the unequal

lens strength experienced by electrons that travel at different angles with respect to the optical axis. These aberrations cause electrons to not focus to a point, but a disc of least confusion(*20*, *21*), reducing the image resolution. Scherzer proved that any electron optical system will suffer from C_S and C_C if simultaneously 4 characteristics were true: 1) the optical system is rotationally symmetric, 2) the system creates a real image, 3) the fields of the system do not vary with time, 4) there is no charge on the optical axis(*12*). In order to create a system that is free of C_S, one of these four characteristics must be broken. To date, the most practical way is to break the rotational symmetry, which can be done through the use of multipole lenses(*12*, *38*). The probe spherical aberration corrector is positioned above the objective lens and utilizes multipole lenses to create a negative C_S, which, when combined with the positive C_S of the objective lens, creates close to net zero C_S. Aberration correctors allow for larger probe convergence angles, which has the advantage of making more compact and larger current probes(*11*, *13*, *39*). The C_S-corrector on UW-Madison's FEI Titan allows for partial correction of lens aberrations, leaving the remaining aberrations limited by C_C. This allows the system's resolution to be limited by the electron emitter source size and not the lens aberrations, making possible 0.8Å resolution Z-contrast STEM images. Figure 2.3(a) shows an atomic-resolution HAADF STEM image of GaN. Figure 2.3(b) is the Fourier transform (FT) of the STEM image, which represents the spatial frequencies that create the STEM image in (a). Figure 2.3(b) shows that spatial frequencies of 1.35 $Å^{-1}$ are present (circled) in the FT, meaning the STEM image has a resolution down to 0.74 Å.

In recent years, the ability to quantitatively compare experimental and simulated STEM image intensities has been developed in order to provide materials information that cannot be directly gained from experimental images alone. One of these "quantitative STEM" techniques is the standard-less atom counting method which is used to count the number of atoms in the atom columns in HAADF STEM images(*19*). In order for the simulated image intensities (determined from the multislice method discussed in section 2.6 below) to accurately mimic the experiments, certain experimental parameters need to be measured. These include putting each experimental image on an absolute intensity scale(*40*, *41*), measuring the experimental sample thickness, measuring the electron probe aberrations, and determining the incoherent electron emitter source size.

To put images on an absolute intensity scale(*42*), the intensity must be normalized to the full, unscattered electron probe intensity, giving intensity values between 0 and 1(*40*, *41*). The simulated image intensities are calculated in this fractional electron count because they are calculated using a normalized quantum mechanical wave function for the electron wave. The square of that wave function predicts the probability density for electron scattering. The experiments measure discrete scattering events for a large number of electrons and that distribution follows the simulation. Therefore, the experimental distribution must be normalized like the simulation to make a quantitative comparison. To normalize the experiment, for each experiment a reproducible HAADF STEM dark reference intensity value and un-scattered probe reference intensity value is determined, representing the intensity values of 0 and 1 respectively. The dark reference

intensity value is determined by setting the HAADF STEM image brightness such that the image has a small (about 1/3 of the intensity range) but measurable number of counts when no electron scattering occurs to the HAADF detector (blank beam). The un-scattered probe reference intensity value is determined by setting the HAADF STEM image contrast such that the image is not saturated (about 2/3 of the intensity range) when the full un-scattered electron probe is steered onto the HAADF detector. Both the image contrast and brightness values are held constant throughout the experiment, so the absolute intensity scale is preserved. More detailed instruction on how to set up absolute intensity scales can be found in Appendix 2. The sensitivity of the HAADF detector is non-uniform and will cause minor errors when comparing simulated and experimental image intensities(*41–45*). This effect has not been incorporated into this work, but it is in the process of being integrated into the process for future studies.

The aberrations present in the convergent electron probe are hard to measure accurately. However, they can be measured roughly using the software responsible for correcting them on UW-Madison's FEI Titan microscope using a special standard sample. This method has limited accuracy because aberrations can drift throughout an experiment, possibly changing the magnitude of the aberration coefficients between when they are measured and when data is acquired. This could affect the accuracy of comparing the experimental and simulated atom shape and size in images. To ease this problem, the atomic column shape in experimental images could be compared to simulated images with varied aberration values to try to pinpoint the aberrations present

during data acquisition(*46*). However, this adds complexity that has not been done in any of this work.

The incoherent source size of the electron emitter must be accurately characterized to quantitatively compare experimental and simulated STEM images(*40*). The Gaussian full width at half maximum(*47*) was determined for the UW Madison Titan microscope's electron emitter by comparing a single experimental HAADF STEM image of GaN $[11\bar{2}0]$ to frozen phonon multislice simulations as a function of the diameter of the Gaussian source function. An experimental position averaged convergent beam electron diffraction (PACBED) pattern (discussed in the next section) acquired at the same location as the experimental HAADF STEM image was compared to frozen phonon multislice simulated PACBED patterns to determine the experimental sample thickness. In 2012, a source full width at half maximum of 88.2 pm minimized the χ^2 between the experimental and simulated Ga columns in GaN images. Our measured value is similar to the source full width at half maximum of previous measurements on similar instruments(*40*, *48*), even though our method of minimizing χ^2 is more quantitative than the previous methods.

Unless otherwise stated, all STEM experiments were performed on UW-Madison's FEI Titan microscope equipped with a CEOS probe aberration-corrector. STEM images were collected with a 24.5 mrad probe semi-angle, 25pA probe current, STEM resolution of 0.9 Angstroms, and electron beam energy of 200 keV. HAADF images were acquired with a detector in the range of 54 to 270 mrad and ABF STEM images were collected with a detector in the range of 11 to 24.1 mrad.

2.5. Position Averaged Convergent Beam Electron Diffraction

Often, accurate sample thickness measurements are necessary to interpret S/TEM data. For example, to quantitatively compare the atomic column intensities in STEM images, the sample thickness must be well known because the intensity depends non-linearly on sample thickness. Three common approaches to measure sample thickness are electron energy loss spectroscopy (EELS) log ratio method(*21*), two-beam CBED(*21*), and position averaged CBED (PACBED)(*49*). The log-ratio EELS method has historically been the primary way of estimating sample thickness. It can be accurate to within ±10% if the inelastic mean free path is known(*50*). However, if the samples are thin, EELS has been shown to systematically overestimate the sample thickness due to surface plasmon scattering(*51*). Two-beam CBED can be accurate down to the unit cell for thick samples >50 nm(*52*), but these thicknesses are unsuitable for high resolution STEM. Two-beam CBED is also limited to smaller convergence angles than those used in atomic resolution AC STEM, is highly sensitive to the position of the electron probe within the unit cell(*49*), and needs tilting away from the zone axis orientation required for high resolution imaging, making it hard to perform the thickness measurement exactly on the imaged area.

PACBED is a recently developed technique in which a pattern is created by scanning a convergent incident electron probe over multiple positions inside at least one unit cell of the sample on a zone axis(*49*). Throughout the duration of the scan, a convergent beam electron diffraction pattern is recorded, creating a PACBED pattern from the incoherently position averaged CBED patterns. Comparing the resulting

experimental PACBED patterns to multislice simulated PACBED patterns, the local sample thickness can be measured to within 1 nm(*49*), and possibly better if better pattern comparison methods are developed. This is the most accurate way to determine local TEM specimen thickness between 0 and 100 nm, and allows for sample thicknesses measurements without having to change the microscopes optical conditions away from those used for atomic resolution STEM. In addition, PACBED pattern symmetry is sensitive to and can be used to determine the local material polarity(*53*), ferroelectric distortions, and octahedral rotations in perovskites(*54*).

2.6. Frozen Phonon Multislice Simulations

The frozen phonon multislice method can be used to simulate TEM/STEM images by calculating the propagation of an electron wave function through a sample while including the effects of specimen thickness and dynamical scattering. It is regularly used to simulate HRTEM images by using a simple plane wave as the incident wave function, as well as CBED patterns and STEM images by using a convergent focused probe as the incident wave function. It is the most accurate method of simulating dynamical scattering of electrons for periodic structures. The multislice method breaks the sample up along the beam direction into slices that are periodic layers of the material. The image is produced by treating each sample slice as a phase grating and diffracting the wave function off each slice. Then the wave function is propagated using a Fresnel propagator to the next slice, and the whole process is repeated all the way through the model. The wave function that results after all the propagation and diffraction steps

represents the wave function at the sample exit surface, and this produces the image and/or diffraction pattern(*55*).

The frozen phonon method is required to accurately simulate the thermal diffuse scattering of electrons from phonons. A typical phonon period is 10^{-13} s, while the typical time for an electron to pass through the sample is 10^{-16} s and the time between electrons is 10^{-9} s. These time scales reveal that each electron that passes through the sample sees a frozen atom slightly shifted off its lattice position due to phonon vibrations and that each electron sees a new phonon configuration. The frozen phonon method simulates multiple results using multiple randomized phonon configurations and averages the results to imitate many electrons seeing many phonon configurations(*55*, *56*). The frozen phonon method uses the Einstein phonon model, which assumes phonons are uncorrelated vibrations of every atom in a harmonic potential. Real phonons have correlated motion and these correlated motions affect the CBED pattern. However, they do not affect the STEM image due to annular averaging(*56*). The Debye-Waller (DW) factor is the measure of the thermal motion of atoms in a solid that is used in the simulations. The frozen phonon multislice simulations presented in this report utilized the Kirkland frozen phonon multislice algorithm(*55*) adapted by Paul M. Voyles for computing clusters on the UW – Madison campus.

2.7. EDS Spectrum Imaging

X-ray energy dispersive spectroscopy (EDS) is used to gain composition information about materials. It relies on ionization events where primary beam electrons

inelasticly transferring energy to electrons bound to atoms within the sample and exciting them to higher energy levels. When electrons relax back to the lower energy states, they can release X-rays with energies that are characteristic of the atoms they came from, therefore supplying composition information about the material. EDS supplies spectra of X-ray intensity vs. energy, with an energy resolution of around 100 eV(*57*). The peaks present in the spectrum can be used to qualitatively and quantitatively analyze the composition of a material(*21*). By utilizing EDS in a STEM, it is possible to record a spectrum image (SI) where composition information is spatially resolved on length scales down to the atomic level(*58*), providing important information about composition variation and segregation. A SI is recorded by raster scanning the STEM probe around the sample and recording an EDS spectrum at each pixel in the STEM image.

2.8. Electron Energy Loss Spectroscopy

Electron energy loss spectroscopy (EELS), like EDS, utilizes the inelastic scattering events of incident primary electron. Incident electrons interact with sample electrons, transfer energy to them, and excite them above the Fermi level to empty electronic states according to Fermi's Golden Rule(*51*). Passing the electrons that exit the sample through a magnetic filter separates the electrons in an energy dispersive plane based on what energy they have transferred to the sample. These electron energy loss spectra contain peaks that correspond to the characteristic electronic energy levels of the atoms present under the electron beam and these spectra can be used to measure composition(*21*).

EELS spectra contain the zero-loss peak, plasmon-loss peaks, and core-loss peaks. The zero-loss peak contains the electrons that pass through the sample without experiencing inelastic scattering events and contains electrons that have experienced thermal diffuse scattering from phonon interactions. It is used to align the spectrometer to the zero energy position. The plasmon-loss peaks are at low energies and arise due to primary electrons exciting plasmons, which are collective oscillations of the free electrons within the sample. The chemical information from sample atoms is contained in the core-loss peaks, which occur at energies corresponding to the difference in occupied and unoccupied electronic states of the material(*21*). By utilizing EELS in a STEM, just like EDS, it is possible to record a SI where composition information is spatially resolved on length scales down to the atomic level(*59*).

Both EDS and EELS are powerful techniques to measure sample composition, but each has its own benefits and deficiencies. EDS has an energy resolution of around 100 eV and EELS can have an energy resolution down to 9 meV(*60*), so measurements of the fine electronic structure of the material can only be done with EELS. EDS is primarily used to measure heavy atoms, while measuring light atoms is better with EELS. EDS has a much higher signal to background than EELS, but the lower efficiency of collecting X-rays due to the small collection solid angles of the EDS detectors requires longer exposure times to collect the required signals. EELS has a smaller signal to background than EDS, but the high efficiency of collecting the scattering events makes the exposure times to collect the required signals smaller.(*57*)

The UW-Madison Titan microscope vacuum causes no measurable build up of

hydrocarbons on the sample even though it does not maintain ultrahigh vacuum (~7 x 10^{-8} Torr at the sample is typical). This was tested by scanning a 5.5 x 5.5 nm field of view with a 100 pA probe for 20 minutes. The EELS carbon K-edge was measured every 5 minutes, revealing no discernable carbon signal throughout. Therefore, we are confident carbon EELS mapping in our STEM reflects the state of the sample and not the state of the microscope.

Chapter 3: Ga-doped ZnO Thin Films

3.1. Introduction

Zinc oxide (ZnO) films doped with gallium (GZO) and aluminum (AZO) are materials that could replace indium tin oxide (ITO) in solar cells, flat screen displays, and light-emitting devices as a high-performance n-type transparent conducting oxide (TCO)(*61–65*). AZO is finding promise in display and solar cells partially due to its low cost and ability to be made in large areas. GZO is finding promise in solid-state optoelectronic applications due to higher performance. The Ga-O bond length (1.88 Angstroms) in GZO is very close to the Zn-O bond length (1.97 Angstroms), creating small stresses associated with Ga-doping compared to AZO and ITO(*66*), resulting in potentially higher mobility and carrier concentration. GZO and GaN have a 1.8% lattice mismatch and both have the wurtzite crystal structure(*67*). Al tends to segregate at surfaces, interfaces, and extended defects, while Ga does not(*68*). This could be crucial for applications requiring fine control over the impurity distribution, including small structures where the effect of surface layers could drastically affect performance.

The growth mechanism and adatom surface diffusion for many wurtzite materials depend on the surface polarity(*69*, *70*). Varying surface atom bond energy, depending on the material's polarity, results in different surface hardness and chemistry, and strongly affects epitaxial growth. Particularly, sublimation of Zn on the O-surface and Zn-surface takes place at 600°C and 380°C respectively(*71*). The two ZnO polar surfaces also display different electron irradiation damage(*72*). The threshold energy required to displace Zn atoms on the surface layer of the Zn-surface is 0.5 MeV lower than that on

the O-surface. The effect of surface polarity on the growth and microstructure of ZnO grown on GaN and sapphire (the two most common substrates) have been thoroughly studied(*69*, *73*). However, the effects of Ga doping and growth polarity have not been previously studied, and as I show below, this results in noticeably different crystal structure with some unusual extended defects.

In general, extended defects, ionized impurities, and native defects in AZO and GZO can be responsible for electron scattering at e^- concentrations of 10^{19}-10^{21} cm^{-3}, resulting in mobility that often depends on the crystal quality(*74*). Combining TEM microstructural characterization, XRD, and electrical measurements enable us to determine the role of various extended defects in carrier scattering in our GZO films. We previously found that the electrical properties of the same GZO layers that are studied here are strongly dependent on growth mode, which varies with Zn-rich and O-rich growth conditions(*74*). Structures grown under metal-rich conditions have excellent properties, including low resistivity ($< 3 \times 10^{-4}$ Ω cm), high carrier concentrations (up to 1.5×10^{21} cm^{-3}), high mobility (from 20 to 80 cm^2/V s depending on the carrier concentration), uniform free carrier depth distribution, and high optical transparency (>95% in the visible spectral region). Structures grown under O-rich conditions required thermal activation of the dopants and even then had relatively low carrier concentration and mobility compared to the Zn-rich structures(*75*).

Here, we have investigated the effects of Ga doping on extended defect formation in three ZnO thin film structures grown under well-controlled Zn-rich and O-rich conditions by plasma assisted molecular beam epitaxy (MBE). We have studied 1) GZO

grown with oxygen-rich conditions on ZnO seed layer/sapphire, 2) GZO grown with metal-rich conditions on ZnO seed layer/sapphire, and 3) GZO grown with metal-rich conditions on GaN. Although MBE has limited throughput, it is well suited to grow model structures under well-controlled conditions, which helps to reveal the microstructure of films grown under different growth conditions.

3.2. Material Synthesis

GZO layers were grown with a MBE system equipped with a RF oxygen plasma source and effusion cells for Zn and Ga at Virgina Commonwealth University by V. Avrutin, H. Liu, N. Izyumskaya, U. Ozgur, and H. Morkoc. GaN(0001) templates grown by metal-organic chemical vapor deposition, c-plane sapphire wafers, and a-plane sapphire wafers were used as growth substrates. The GZO layers were grown on nominally undoped ZnO seed layers(*74*). A plasma power of 400 W, Zn cell temperature of 350°C, substrate temperature (T) of 400°C, and Ga cell temperature (T_{Ga}) of 600°C were used for all the GZO layers. The effects of varying the substrate temperature(*75*, *76*) and the Ga cell temperature on electrical and structural characteristics(*77*) were published elsewhere. The flux of reactive oxygen was controlled by passing it through a mass-flow controller prior to the plasma source and measured by the corresponding pressure (P_{O2}) in the chamber during growth. Samples that are metal (Zn + Ga) rich, near stoichiometric (reactive oxygen to incorporated Zn ratio ≈ 1:1), and oxygen-rich conditions used P_{O2} = 4.5 x 10^{-6}, 8.0 x 10^{-6}, and 1.5 x 10^{-5} Torr, respectively(*74*, *75*). The growth rate vs. oxygen pressure dependence was used to determine the reactive oxygen–

to–incorporated Zn ratios. After deposition, rapid thermal annealing in nitrogen at 600°C was used to activate dopants for the oxygen-rich and stoichiometry samples.

3.3. Procedures

Alex Kvit and I conducted TEM and STEM experiments. TEM samples were prepared by mechanical polishing with diamond lapping films and dimple grinding in the $[11\bar{2}0]$ cross-section projection. All samples were ion milled in a Fischione 1010 low angle ion mill and then in a Fischione low energy Nanomill to further thin the sample. STEM experiments were performed using thetypical STEM imaging conditions discussed in Chapter 2.4, except ABF STEM images were collected with a detector in the range of 4.0 to 8.8 mrad, smaller than normal ABF STEM images(*78*). STEM electron energy loss spectroscopy (EELS) spectrum images (SIs) were acquired using a 24.5 mrad probe semi-angle, spectrometer collection angle of 82 mrad, 400 pA probe current, STEM resolution of 2.1 Angstroms, and electron beam energy of 200 keV. EDS measurements were done at probe current 800 pA. PACBED, using the STEM imaging conditions stated above, was used to confirm the polarity of the GZO films(*49*). PACBED patterns were acquired while scanning 2 nm x 2 nm image areas. Conventional TEM measurements were conducted at 200 keV on UW-Madisons' Philips CM200UT and Titan microscopes.

PACBED patterns were simulated using the frozen phonon multislice technique(*55*) in order to determine the ZnO polarity. Zn-polar ZnO PACBED patterns were calculated using Debye−Waller factors from Reid(*79*), averaged over one ZnO

$[11\bar{2}0]$ unit cell and 16 phonon configurations.

3.4. Defects in Ga-doped ZnO Thin Films

ZnO seed layer on sapphire and GaN

The main defects in the ZnO seed layer grown on a-plane sapphire are low-angle grain boundaries. The ZnO grains are mostly perpendicular to the ZnO/sapphire interface and are textured with an 8° -10° misorientation. Selected area diffraction (SAD) taken from both the substrate and ZnO seed layer indicates good epitaxial relationship between (0001) ZnO and $(11\bar{2}0)$ sapphire in the growth direction, and $[11\bar{2}0]$ ZnO and [0001] sapphire in the in-plane direction. PACBED patterns (not shown but similar to Figure 3.7) acquired from the ZnO seed layer grown on sapphire show it is O-polar, while PACBED patterns acquired from the ZnO seed layer grown on GaN shows it is Zn-polar.

Ga-doped ZnO grown with oxygen-rich conditions on ZnO seed layer/sapphire

Gallium doped ZnO grown under oxygen-rich conditions leads to a textured film and the instability of the wurtzite crystal structure. Figure 3.1 shows the switch from the wurtzite structure at the bottom of the film to zinc blend at the top of the film. The image was taken using a strong-beam condition in central dark-field mode (g,-3g) with the [111] g vector of the zinc blende structure. As seen in Figure 3.1, these conditions produce zinc blende grains with brighter intensity and wurtzite grains with darker intensity, clearly showing the 2-layer structure. The SAD patterns from these films as seen in Figure 3.1(c) show additional mirror symmetry reflections about the (220) axis

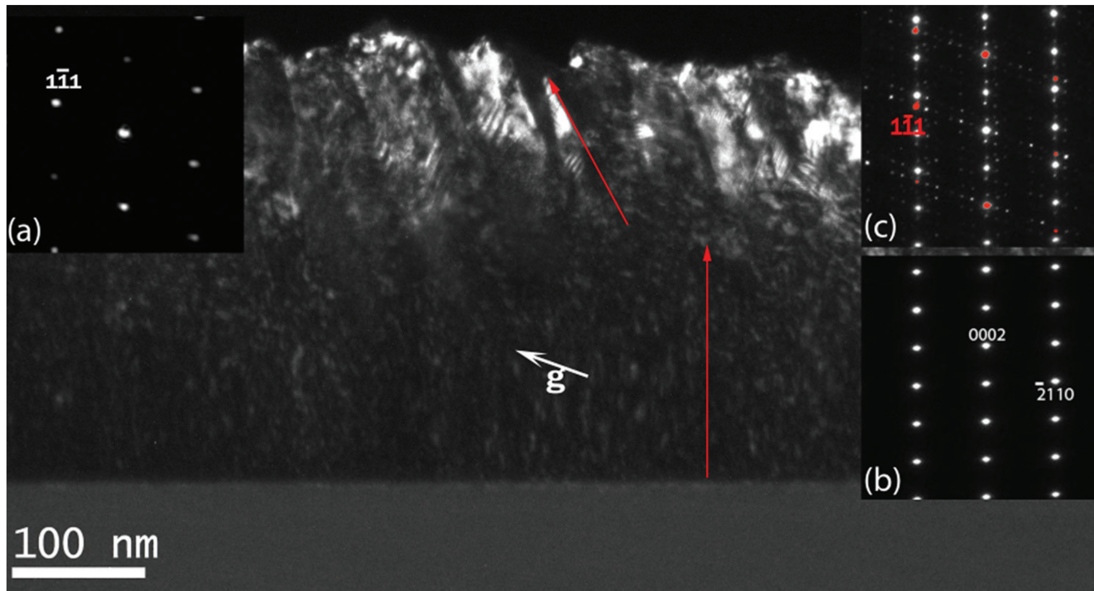

Figure 3.1: Strong beam dark-field TEM image using the [111] g vector of the GZO zinc blende structure. (a) SAD pattern of one grain in the GZO zinc blende top layer. (b) SAD pattern from the GZO wurtzite bottom layer. (c) SAD pattern from a region with both GZO wurtzite and zinc blende. Double diffraction and multiple twins within the zinc blende layer cause the additional reflections in (c). The SAD patterns are taken at the [0110] zone axis for wurtzite and the [110] zone axis for zinc blende. Image by Alex Kvit.(*68*)

corresponding to twin boundaries, and additional reflections related to multiple diffraction in the {111} directions. The SAD patterns shown in Figure 3.1(a)-(c) confirms the growth direction changes from [0001] in the wurtzite ZnO layer to [0$\bar{2}$2] in the zinc blende ZnO layer. The grain boundaries in the zinc blende GZO are tilted by 24° from the direction perpendicular to the substrate/ZnO interface, coinciding with [2$\bar{2}$0] of the zince blende structure.

Figure 3.2 (a) shows a HAADF STEM image of the GZO/ZnO/sapphire structure taken near the [1$\bar{1}$00] GZO zone axis. A 15-20 nm thick layer on top of the GZO is

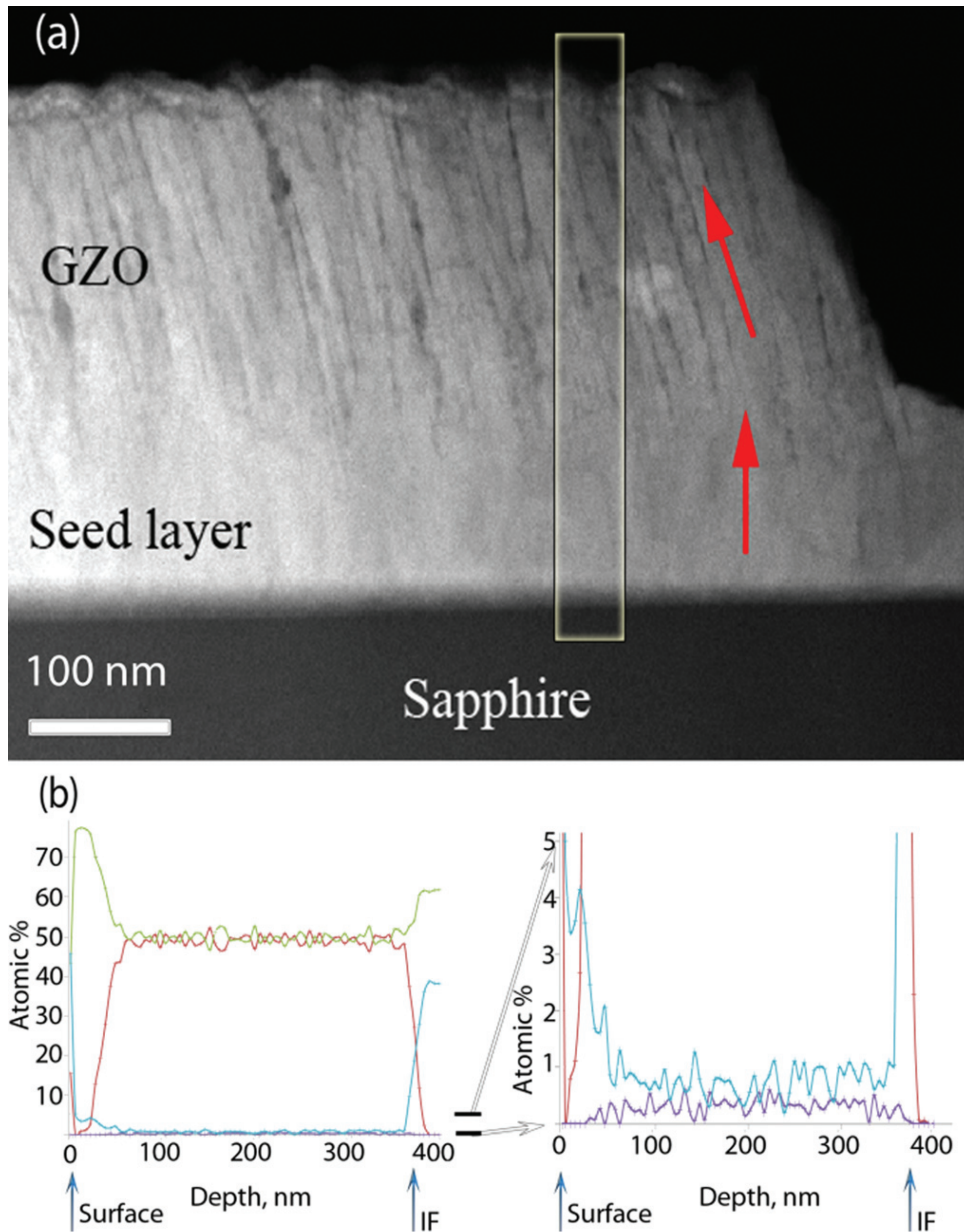

Figure 3.2: (a) HAADF STEM image of a GZO/ZnO/sapphire structure grown under oxygen-rich conditions close to the GZO $[1\bar{1}00]$ zone axis. (b) EDS spectrum profiles for host and impurity elements in GZO/sapphire acquired from in the box in (a). The blue line represents Al. The purple line represents Ga. The red line represents Zn. The green line represents O. Image by Alex Kvit.(*68*)

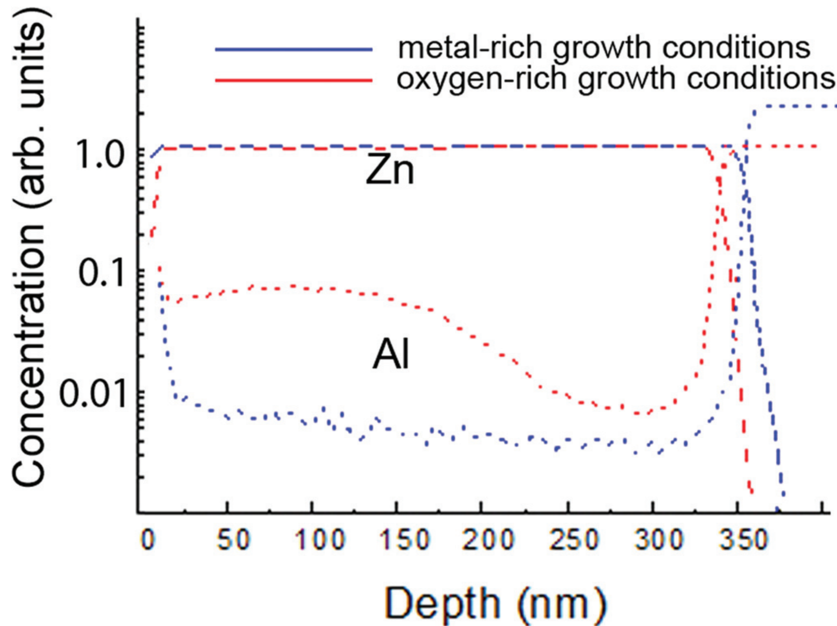

Figure 3.3: SIMS profiles (measured by Evans Analytical Group) for Zn (dashed lines) and Al (dotted lines) for GZO grown under metal-rich (blue) and oxygen-rich (red) growth conditions. Images by Alex Kvit.(*68*)

visible. Figure 3.2(b) shows the composition of the layers from EDS spectrum profiling from the box in Figure 3.2(a). The EDS data in Figures 3.2(b) shows the extra surface layer is aluminum oxide, while TEM and STEM nanodiffraction (not shown) show that this layer is amorphous. Gallium has an almost homogeneous depth distribution in the GZO layer. The Al depth distribution suggests diffusion from substrate through the entire GZO layer to the surface. The SIMS profiles shown in Figure 3.3 confirm the surface segregation of Al in oxygen-rich GZO films. Figure 3.3 also shows that Al has a higher concentration in GZO layer grown in oxygen-rich conditions compare to Al concentration in the layer grown in metal-rich condition. If we assume the sapphire substrate is the major source for Al incorporation into GZO films, the Al diffusion

coefficient should be higher in GZO grown in oxygen-rich conditions than metal-rich conditions. The Al concentration profile also reveals different Al concentrations coinciding with the zinc blende and wurtzite layers in the GZO film.

Ga-doped ZnO grown with metal-rich conditions on ZnO seed layer/sapphire

Growing Ga-doped ZnO films with metal-rich conditions creates a structure that is much closer to single crystal material than the textured structure of GZO grown under oxygen-rich conditions. SAD (not shown) taken along ZnO $[01\bar{1}0]$ (sapphire $[01\bar{1}1]$) shows very good epitaxial relationship between GZO and sapphire. However, the GZO films grown under metal-rich conditions are porous, as shown in the HAADF STEM images of Figure 3.4. The voids have a variety of shapes and occur at very high density (up to 2 x 10^{17} cm^{-3}). The most common defects observed are pyramid-shaped voids, basal plane stacking faults, and basal plane inversion domain boundaries (IDBs). The size of the pyramid-like voids ranges from 1 to 20nm, and they often overlap and form chains of voids due to their high concentration. Most of the voids have {0001} base facets perpendicular to the growth direction and are point-up or point-down pyramids with respect to the growth direction. As shown in Figure 3.4, point-up pyramids tend to group together and point-down pyramids tend to group together in nanoscale domains.

Figure 3.5 contains STEM images showing there are no voids in the nominally undoped ZnO seed layer and the pores become present at the interface between the GZO and ZnO seed layer. At the interface between the ZnO seed layer and GZO layers, there is a set of point-down pyramid voids. Then there is a 20 nm thick layer that does not

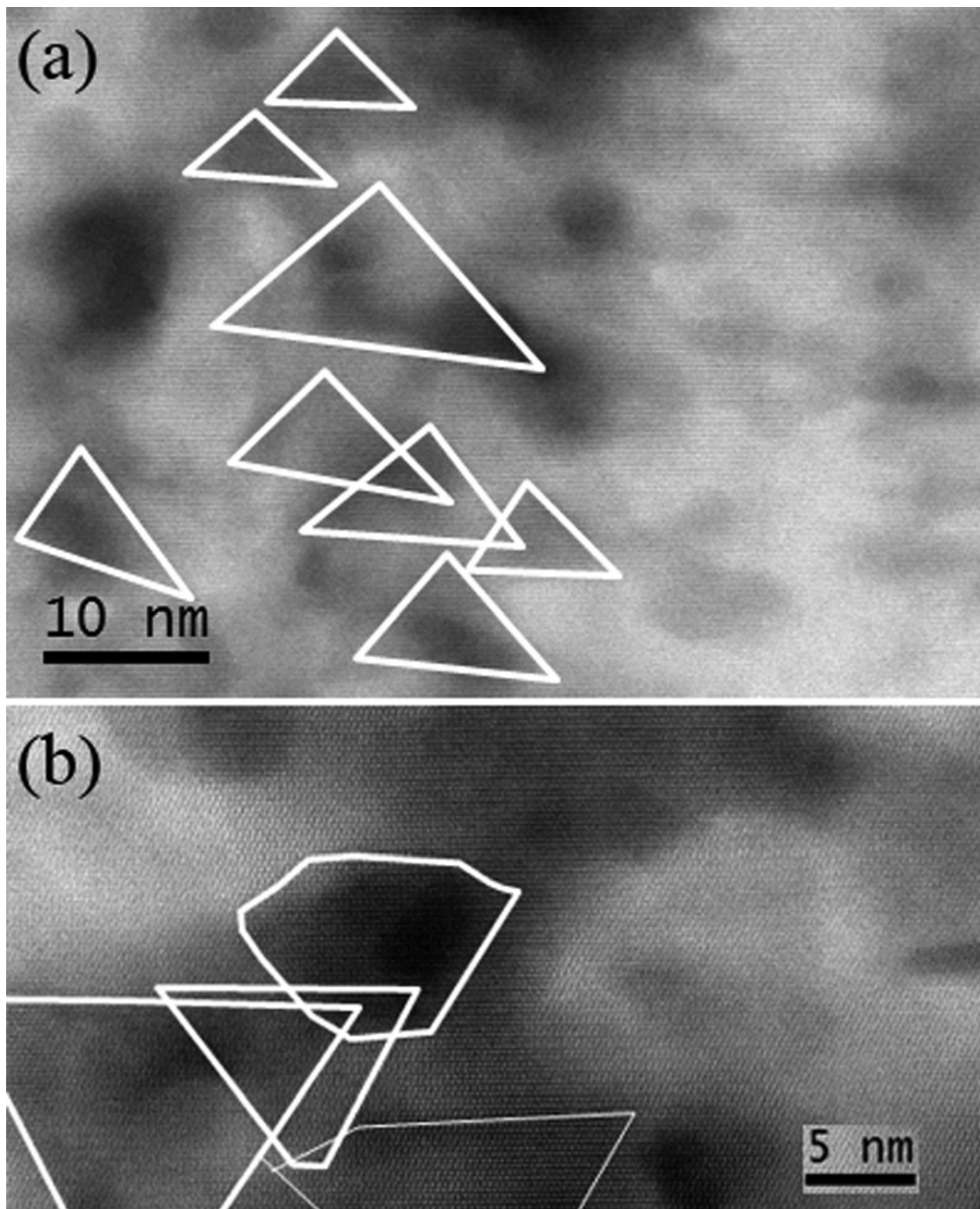

Figure 3.4: HAADF STEM images of GZO grown under metal-rich conditions showing porous nanostructures. In (a), pointed-up pyramid shaped voids prevail. In (b), pointed-down pyramid shaped voids prevail. Image by Alex Kvit.(*68*)

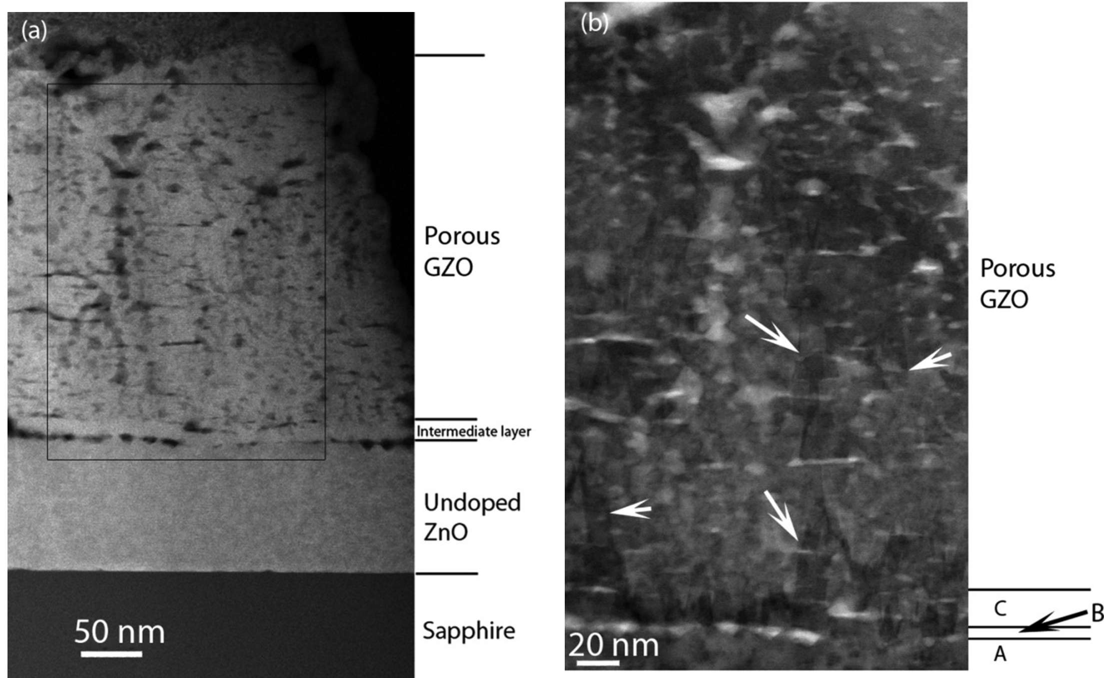

Figure 3.5: (a) HAADF STEM image of GZO grown under metal-rich conditions on top of an undoped ZnO seed layer and on a sapphire substrate. (b) ABF STEM image taken from the rectangle in (a). The area marked A is the undoped ZnO seed layer. The area marked B is the layer where Ga doping starts, coinciding with a line of pyramid voids (shown by brighter intensity in ABF images). The area marked by the letter C indicates the layer containing many IDBs and voids. The arrows indicate dark lines, which are vertical IDBs. Both images were taken in the ZnO $[2\bar{1}\bar{1}0]$ zone axis. Image by Alex Kvit.(*68*)

contain any voids, followed by the rest of the GZO film, which contains a very complex porous structure.

Figure 3.6 shows STEM images of the pyramid voids at the interface between the ZnO seed layer and GZO. These images indicate this interface is the origin of the IDBs running through the GZO film. The pores within the first 25 nm of the seed layer terminate most of the IDBs, but some of them propagate all the way through the GZO

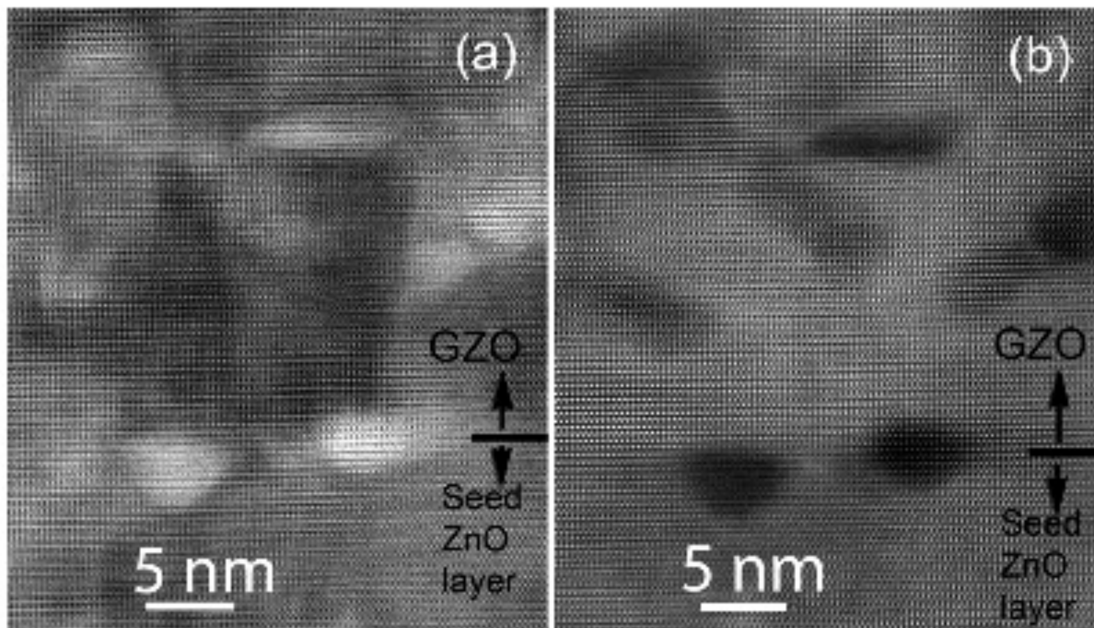

Figure 3.6: High-resolution STEM images of the interface between undoped ZnO seed layer and GZO grown under metal-rich conditions. (a) ABF STEM image, in which IDB contrast is strong. (b) Simultaneously acquired HAADF STEM image, in which IDB contrast is weak. Image by Alex Kvit.(*68*)

layer. In the ABF images of Figure 3.5(b) and Figure 3.6(a), the IDBs inclined to the beam direction are dark lines, as indicated by the white arrows in Figure 3.5(b). The polarity domains form columnar structures, with the basal-plane defects and the point-up pyramid voids occurring in columnar domains of one polarity, and point-down pyramid voids occurring in columnar domains of the opposite polarity.

PACBED(*49*) was used to confirmed the polarity change between columnar domains by comparing experimental patterns to simulated patterns with know polarity. Figure 3.7 shows regions of experimental PACBED patterns from two separate domains, along with the corresponding simulated patterns that have matching asymmetries,

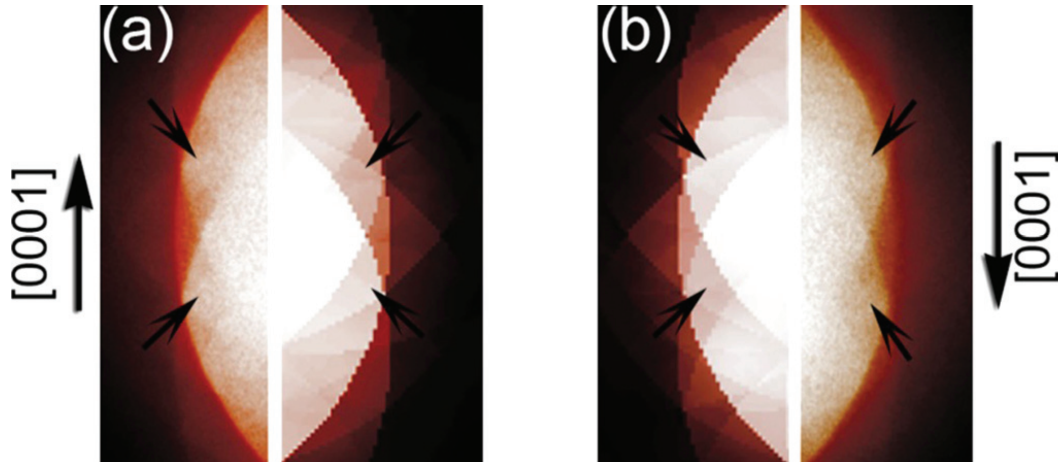

Figure 3.7: Cropped experimental and simulated PACBED patterns used to determine local sample polarity. The experimental PACBED patterns (left image of (a) and right image of (b)) were acquired in different domains of the metal-rich grown GZO. The frozen-phonon multislice simulated PACBED patterns (right image of (a) and left image of (b)) are from (a) O-polar ZnO and (b) Zn-polar ZnO. The simulated patterns show matching asymmetry (marked by the arrows) with the compared experimental patterns, revealing the different domains have different polarity.(*68*)

confirming the polarity change across domain boundaries. Figure 3.7(a) is from O-polar ZnO, and Figure 3.7(b) is from Zn-polar ZnO.

In addition to IDBs and voids, the metal-rich GZO films contain low angle grain boundaries that propagate through the GZO layer from the ZnO seed layer with grain sizes that vary from 30 to 90 nm. Electron nano-diffraction (not shown) from both sides of grain boundaries confirms these extended defects are low angle grain boundaries.

Figure 3.8 shows EELS spectrum image data of host and impurity elements around a void in GZO grown under metal-rich conditions. The EELS data was de-noised using principle component analysis, keeping 5 principle components. The concentrations

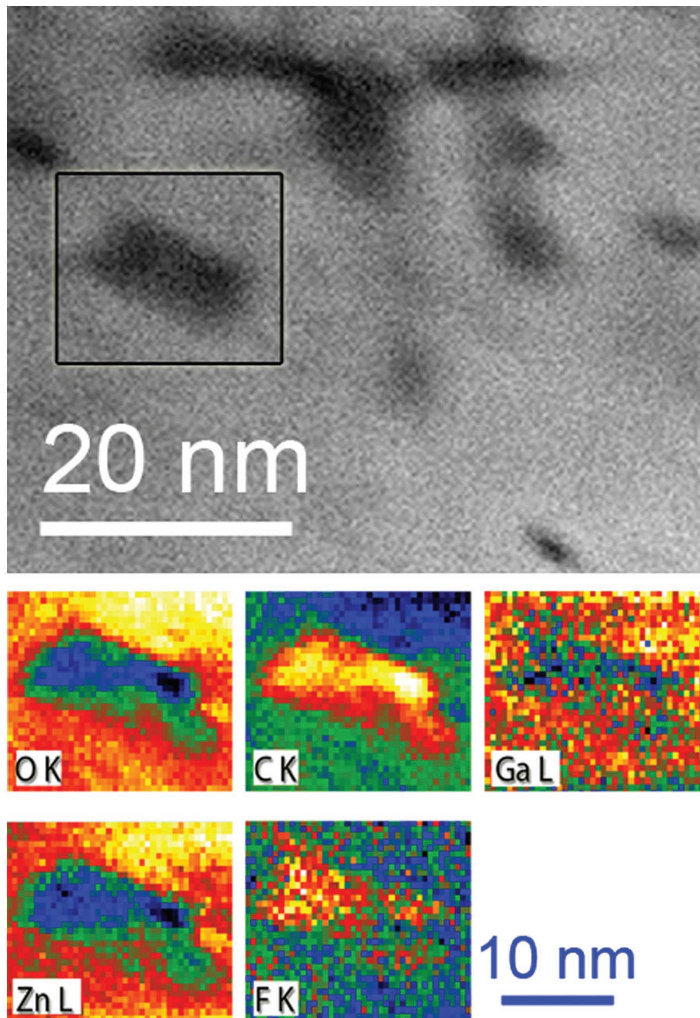

Figure 3.8: EELS spectrum images showing the distribution of host and impurity elements around a void in metal-rich grown GZO. The top image is a HAADF STEM image of the general sample region. The EELS color maps are from inside the black box in the HAADF STEM image. The color maps show the integrated intensity of each edge after background subtraction and normalization to the O K-edge. Image by Alex Kvit.(*68*)

of the Zn and O host elements inside the void are small, as expected. Within our detection limits, no segregation of Ga dopants around the voids or any other extended defects, interfaces, or surfaces is observed. Carbon and fluorine, two common residual

impurities, do accumulate inside the pores.

Ga-doped ZnO grown with metal-rich conditions on GaN

Due to the excellent lattice match between ZnO and GaN, GZO layers on GaN have a much smaller concentration of extended defects than those grown on sapphire. GaN substrates are also not a source of Al impurities, eliminating the problem of Al diffusion to the surface discussed previously. Figures 3.9(a) – (c) show HAADF STEM images of GZO grown on a GaN template under metal-rich conditions. It shows GZO grows epitaxially on a 4 nm thick undoped ZnO seed layer on a GaN substrate and GZO has atomically sharp interfaces and no voids. Figure 3.9 (b) shows there are two rows of defects near the ZnO/GaN interface, marked "A" and "B". "A" defects are exactly at the interface between GaN and the ZnO buffer layer, and their strain-induced contrast slightly extends into the GaN substrate. "A" defects are misfit dislocations with Burgers vectors 1/3$[\bar{1}2\bar{1}0]$, 1/3$[\bar{2}110]$, and 1/2$[1\bar{1}00]$, and a density that is high enough to compensate most of the interface strain. "B" defects are 3–4 nm away from the ZnO/GaN interface inside the ZnO seed layer. They are misfit dislocations at the ZnO seed layer/GZO interface and have relatively diffuse strain-induced contrast. The two rows of misfit dislocations located at the two interfaces probably indicate that the ZnO seed layer thickness is smaller than the critical thickness for strain relaxation, so when the combined GZO and ZnO seed layer reaches the critical thickness during growth, the misfit dislocations are likely generated at both interfaces simultaneously. The residual stress due to thermal expansion coefficient differences (GZO, ZnO, and GaN) is likely

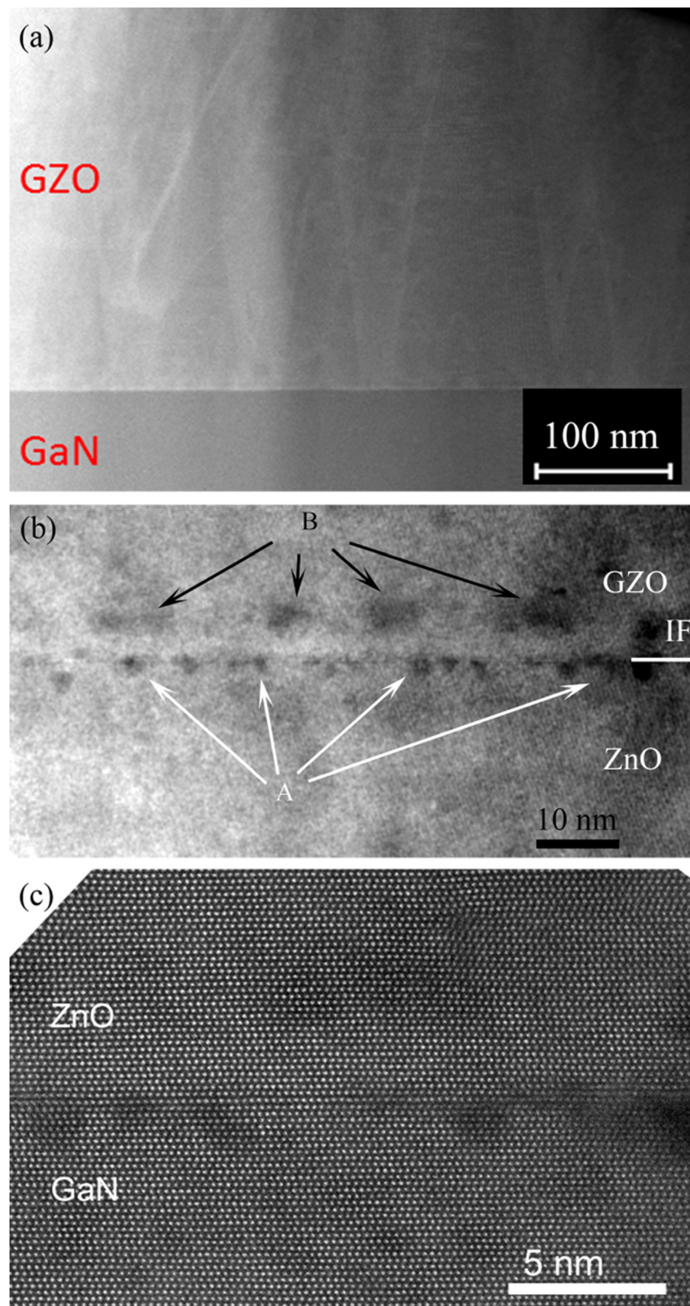

Figure 3.9: HAADF STEM images in the ZnO $[2\bar{1}\bar{1}0]$ projection. (a) shows the entire composite structure of GZO grown on a GaN template. (b) shows two rows of defects near the interface between GaN and ZnO. (c) shows a high-resolution image of both interfaces, revealing misfit dislocations between GaN and the ZnO seed layer, and between the ZnO seed layer and the GZO. Image by Alex Kvit.(*68*)

compensated by threading extended defects inside the GZO layer.

Figure 3.9(a) shows the dominant extended defects in the GZO layer are low-angle grain boundaries with a grain size between 50 and 80 nm. The low-angle grain boundaries are probably the major extended defects responsible for free carrier scattering because the misfit dislocations are localized to the small area at the interfaces.

EDS spectrum imaging (not shown) did not reveal any irregularities in the concentration vs. depth profiles for the major impurity and host elements. It showed flat distribution profiles for Ga in GZO, and no accumulation of Ga at the defects, surfaces, or interfaces.

Discussion

Gallium doping does not affect the polarity stability of GZO grown on Zn-polar undoped ZnO seed layers on GaN substrates. However, Ga doping does affect the polarity stability of GZO grown on O-polar undoped ZnO seed layers on sapphire substrates. These observations might suggest that Ga doping of O-polar ZnO leads to the accumulation of Ga species on the surface of the film during growth. The accumulated Ga on the surface may modify the dangling bond configurations on the surface, leading to a change in the surface adsorption and evaporation coefficients for Zn and O species, causing a polarity switch from O to Zn. This process could be laterally inhomogeneous due to surface fluctuations of the Ga concentration at the nanoscale, creating the observed columnar structures of both polarity materials. Further switching of the O-polar material to Zn-polar material may not occur because Ga diffuses easily from the O-polar surfaces

to the Zn-polar surfaces. However this might suggest that the Zn-polar domains should have more Ga than O-polar domains, which is not experimentally observed.

The different concentration distributions of Al and Ga in GZO/sapphire shown in Figures 3.2 and 3.3 suggest different diffusion mechanisms for Al and Ga, even though they are both group III elements widely used for n-type doping of ZnO. The increased concentration of Al is always observed in O-polar GZO, suggesting the mechanism of Al diffusion, and not Ga diffusion, is dominated by electromigration and depends on the electrical charge of the surface. A high electromigration coefficient for Al in ZnO could limit the applications of AZO in some devices that require a homogeneous dopant distribution and a large applied field. The Ga concentration profile is flat with no tendency to accumulate on surfaces, interfaces, or extended defects, highlighting another positive attribute of Ga as a donor dopant in ZnO compared to Al. Two common residual impurities, carbon and fluorine, accumulate inside these voids and Ga does not. The role of C in is controversial(*80*, *81*), but F is considered to be a shallow donor(*82*). These results also suggest that oxygen deficiency may enhance graphitic cluster formation during growth, similar to previous reports(*83*).

In the cases of GZO/sapphire grown with O-rich conditions and GZO/GaN grown with metal-rich conditions, low-angle grain boundaries are the major defect impacting electron scattering and electron mobility. The 24° grain boundary inclination in GZO/sapphire grown under O-rich conditions should strongly affect the carrier scattering. The strong associated polar field in highly ionic ZnO should give rise to a Coulombic interaction with free carriers and reduce electron mobility. Our previous

investigations(*75*, *76*) show strong correlation between grain size (from STEM and XRD data) and mobility, showing a significant contribution of grain-boundary scattering in these samples. The electrical data also revealed a significant effect on mobility from ionized impurity and polar optical phonon scattering, especially for samples with large grains and thus relatively high carrier mobility(*75*).

On the other hand, the formation of voids and IDBs in GZO/sapphire grown under metal-rich conditions suggest the electron mobility could be limited by scattering at these pores. The pores must also reduce the conductance of the film because they reduce the current-carrying cross-sectional area, but that effect may be more than compensated by the decrease in the density of the other defects. The small pores (with sizes much smaller than the wavelength of visible light) also increase the optical transparency.

3.5. Conclusions

The microstructure of GZO grown by MBE under metal-rich conditions on sapphire, O-rich conditions on sapphire, and metal-rich conditions on GaN has been investigated by various TEM techniques, with the motivation of better understanding GZO for its application as a transparent conducting oxide. All GZO layers grown on a-sapphire and GaN show relatively good epitaxial relationship with the substrate, but the prevalent extended defects strongly depend on the oxygen-rich and metal-rich growth conditions.

GZO films grown under O-rich conditions on a-sapphire substrates show the instability of the wurtzite crystal structure. We observe phase switching from the

wurtzite structure to the zinc blende structure part way through the GZO layer growth. The grain boundaries in the top zinc blende layer are along the [022] direction for the zinc blend phase and are tilted 24° from the [0001] growth direction of the wurtzite layer. This inclination could noticeably affect the carrier scattering because an inclined grain boundary likely has a strong polar field in highly ionic ZnO, resulting in Coulombic interactions between free carriers and grain boundaries. Al diffusion is observed from the sapphire substrate to the GZO surface, causing amorphous Al and O surface accumulation. Ga shows uniform distribution through all the GZO layers, possibly implying that GZO has more predictable optical and electrical properties than AZO.

GZO films grown under metal-rich conditions on a-sapphire substrates have relatively good epitaxial crystal quality with slightly textured grains as large as 90nm. Inside the grains, there are two types of domains, O-polar and Zn-polar. These films also show a porous structure of interlinking faceted voids grown on top of non-porous O-polar ZnO seed layers. One explanation of this microstructure is that Ga-doping of ZnO with O-polarity leads to the accumulation of Ga species at the nanoscale on the growth surface, eventually switching the surface polarity from O to Zn. The final structure is a porous GZO layer with slightly textured grains and smaller domains of different polarity material. Carbon and fluorine impurities segregate inside the voids, while Ga does not accumulate inside the voids or at any other extended defect. Further optimization of growth parameters is needed to avoid the polarity switching of GZO/sapphire grown under metal-rich conditions.

GZO grown on GaN under similar metal-rich growth conditions have Zn-polar

material with no voids. A network of misfit dislocations at the ZnO seed layer/GaN substrate interface and the GZO/ZnO seed layer interface relaxes most of the residual stress between the thin layers and the substrate. Low-angle grain boundaries that run through the GZO film are the major microstructural defect in these films.

Chapter 4: Sb-doped ZnO Nanowires

4.1. Introduction

Zinc Oxide (ZnO) is a promising semiconducting material for UV optoelectronics because of its large exciton binding energy of 60 meV and direct wide band gap of ~3.37 eV, making it a bright emitter at UV wavelengths(*84*). ZnO is also relatively cheap, abundant, and environmentally friendly, as well as having good availability of undoped large area substrates. To make ZnO most useful for optoelectronic device applications, high quality *p-n* homojunctions must be accessible. However, like most wide band gap semiconductors, ZnO suffers from the doping asymmetry problem(*85*, *86*). Due to native point defects, ZnO is intrinsically *n*-type, and more heavily *n*-type ZnO can be easily synthesized. After extensive efforts using multiple doping schemes and some reports of *p*-type ZnO (such as P, As, Ga, Al, In, Li, N, Ag, K, and P)(*87–98*), there remains a lack of reliable *p*-type dopant for ZnO, impeding its use in optoelectronic applications(*99–101*). The lack of *p*-type dopants is primarily due to native donor defects, low dopant solubility, and large accepter ionization energies(*99–101*). *p*-type ZnO thin films(*89*, *92*, *102–107*) and nanowires (NWs)(*95*, *108–110*) have been reported using a variety of doping schemes, but none of the results have been widely reproduced or resulted in stable optoelectronic devices, until recently. As and Sb doping has been reported to create *p*-type ZnO films(*111–116*) and NWs(*117*), and in particular, Sb-doped ZnO NWs grown on *n*-type ZnO thin films have been used to create photodiodes(*118*) and electrically pumped waveguide lasers that are stable over 7 months(*119*).

The most intuitive hypothesis for *p*-type ZnO behavior from Sb doping is that Sb substitutes for O. However, Wahl et al. reported experimental evidence using electron emission channeling that Sb primarily substitutes for Zn, contradicting the intuitive hypothesis(*120*, *121*). Because simple substitutional Sb dopants for Zn cannot produce *p*-type material, it has been proposed that Sb defect complexes are responsible for the *p*-type conduction,(*122, 123*). Limpijumnong *et al.* used DFT to predict a $Sb_{Zn} + 2V_{Zn}$(and $As_{Zn} + 2V_{Zn}$) defect complex could produce shallow acceptor states and *p*-type conductivity(*124*). Later, Puchala *et al.* used DFT to predict that it is energetically favorable for the Sb atoms in this point defect complex to pop off the Zn site into an interstitial site, producing a $Sb_I + 3V_{Zn}$ defect complex(*125*). However, this new complex is predicted to create deeper acceptor states(*125*). Despite significant interest in these proposed causes for *p*-type Sb-doped ZnO, no conclusive experimental evidence supporting them has been published.

Imaging single dopant atoms is possible using HAADF STEM imaging if the dopant species has a significantly higher atomic number (Z) than the surrounding matrix material and a small enough concentration(*3*). Figure 4.1 shows a frozen phonon multislice simulated HAADF STEM image of one of the Sb defect complexes in ZnO discussed above. The image predicts that the Sb dopant atoms are visible in HAADF STEM images if the STEM specimen is thin enough (<15 nm). The predicted visibility of Sb dopant atoms in STEM images highlights one method for experimentally supporting the defect complex theory behind *p*-type Sb-doped ZnO.

Recently, Fei Wang and Xudong Wang demonstrated *p*-type Sb-doped ZnO NWs

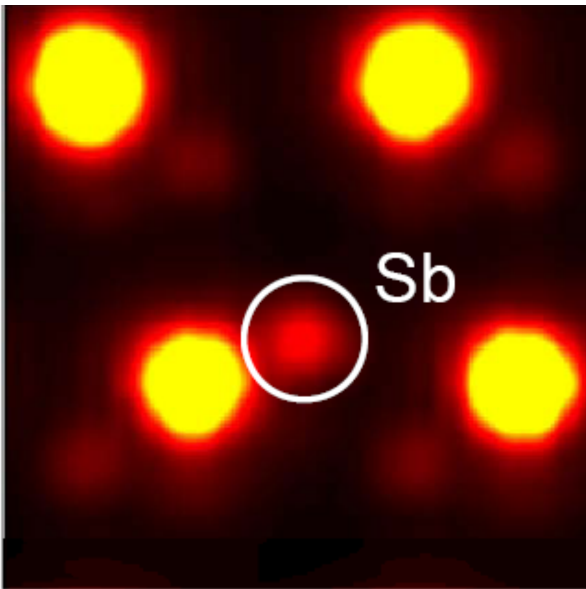

Figure 4.1: Frozen phonon multislice HAADF STEM image of a $Sb_I - 2V_{Zn}$ defect complex in ZnO, demonstrating the visibility of this class of defect complex in thin TEM specimens.

using an aqueous solution synthesis method that has the advantage of low cost and ease of processing(*117*). Figure 4.2 shows scanning electron microscopy (SEM), EDS, x-ray diffraction, and transmission electron microscopy results from the Sb-doped ZnO NWs. Figure 4.2(a) and (b) show SEM images of the as-grown Sb-doped ZnO NWs distributed on the silicon substrate. The NWs have a hexagonal cross-section and are on average ~100–200 nm in diameter and ~4 μm long. Figure 4.2(c) shows an EDS spectrum from a NW revealing the presence of Sb in the doped NWs. The XRD data in Figure 4.2(d) shows the NWs have the wurtzite crystal structure. The intense (0002) peak confirms the NWs have semi-aligned growth directions. The TEM images and selected area diffraction pattern in Figure 4.2(e)-(g) show the NWs have relatively clean growth surfaces and are single crystal with a (0001) growth direction.

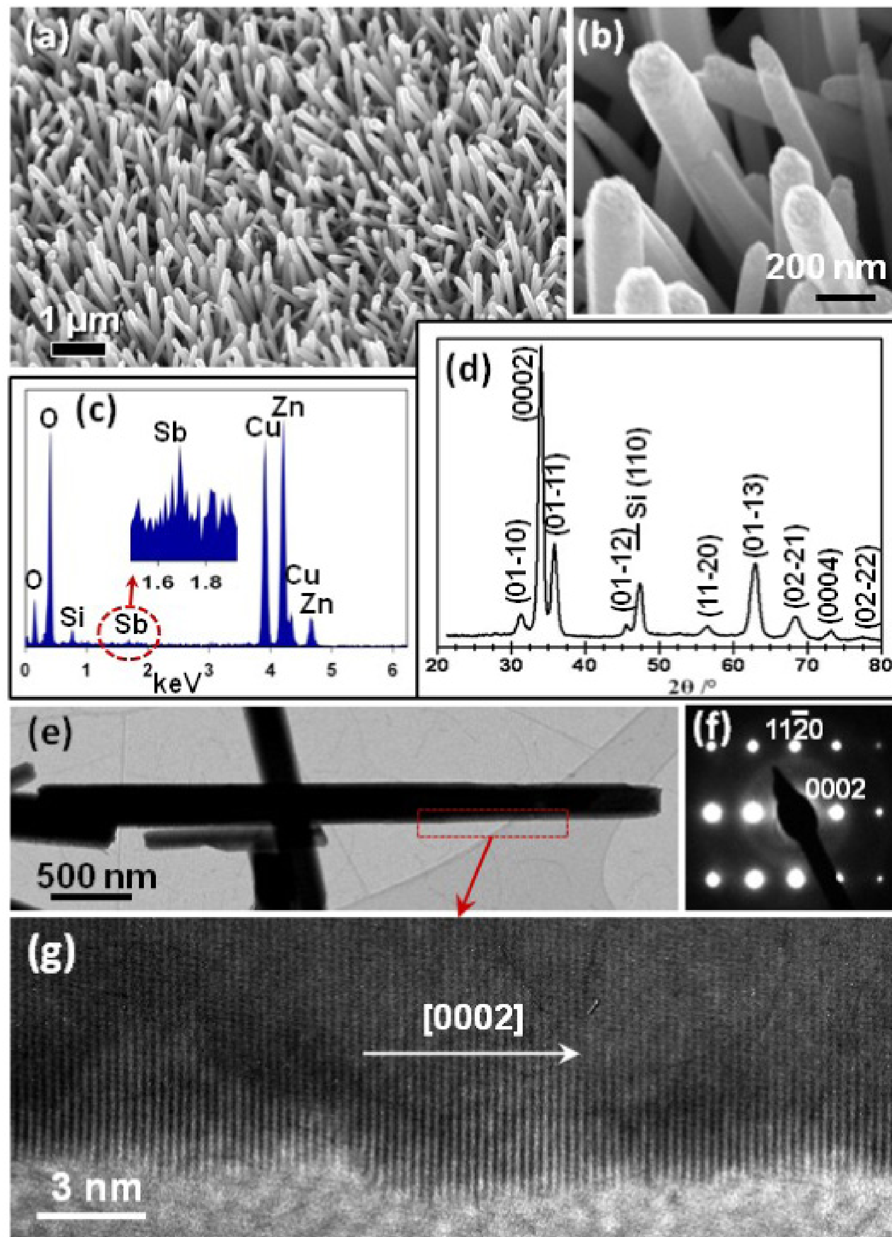

Figure 4.2: (a) and (b) show SEM images of the as-grown Sb-doped ZnO NWs distributed on the silicon substrate. (c) shows an EDS spectrum from a Sb-doped NW. (d) X-ray diffraction data confirming the wurtzite crystal structure and (0001) growth direction. (e) Low magnification TEM image. (f) Selected area diffraction pattern from single NW. (g) High magnification TEM image of area inside the red box in (e).(*117*)

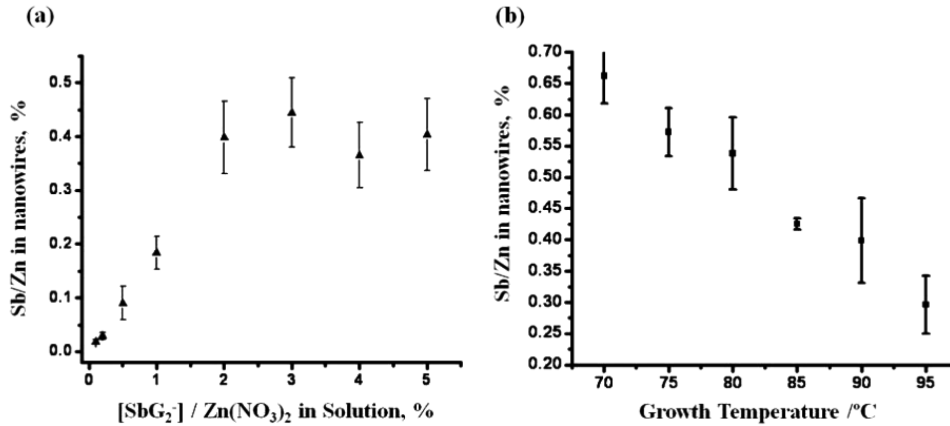

Figure 4.3: (a) Plot of the Sb/Zn percentage in the Sb-doped ZnO NWs vs. the amount of Sb glycolate in solution at a constant 90°C temperature. (b) Plot of the Sb/Zn percentage in the Sb-doped ZnO NWs vs. the growth temperature at a constant 2% Sb glycolate concentration.(*117*)

The Sb concentration in the NWs can be tuned by varying the growth temperature and the solution chemistry(*117*). Figure 4.3(a) shows that by holding the growth temperature at 90°C, keeping all the solution chemistry the same except for the Sb glycolate, and varying the Sb gycolate concentration between 0-2%, it is possible to linearly control the amount of Sb incorporated into the NWs. Above an antimony glycolate concentration of 2%, the Sb incorporated into the NWs saturates. Figure 4.3(b) shows that by holding all the solution chemistry the same with an antimony glycolate concentration of 2% and varying the growth temperature between 70-95°C, the Sb incorporation into the NWs can be controlled in a decreasing linear relationship.

NW field effect transistors (FETs) were constructed from single undoped and Sb-doped NWs to allow measurement of the electrical transport behavior of the NWs. The FET consists of a single NW on a 100 nm SiO_2 dielectric. The back gate consisted of a

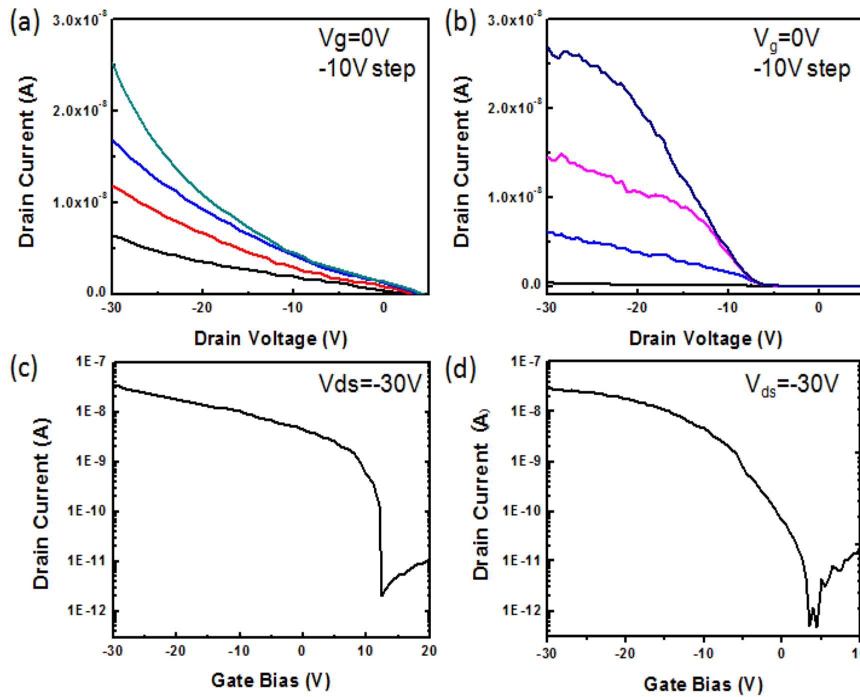

Figure 4.4: Single nanowire FET electrical measurements showing stable p-type character directly after synthesis and 18 months after fabrication. Drain current vs. drain voltage plots at various gate voltages, starting at 0 V and increased by -10 V steps to -30 V (a) as-synthesized and (b) 18 months later. Drain current vs. gate bias plots at a drain-source voltage of -30 V (c) as-synthesized and (d) 18 months later.(*1*, *117*)

heavily-doped Si substrate and the source and drain contacts were Ti / Au. To passivate and seal the FET, 100 nm of SiO_2 and 50 nm of Si_3N_4 were deposited. Jung-Hun Seo and Zhenqiang Ma conducted the electrical measurements with a HP4155B semiconductor parameter analyzer. Further details of the FET fabrication and electrical measurement technique may be found elsewhere.(*117*)

The undoped ZnO NWs show *n*-type conduction while the Sb-doped ZnO NWs show clear *p*-type conduction(*117*). In addition, electrostatic force microscopy shows the

shift of the metal-semiconducting barrier due to the Sb-doping, supporting the Sb-doping cause *p*-type conductivity(*117*). Figure 4.4 shows the electrical transport behavior of a single Sb-doped ZnO NW FET device (a) & (c) as-synthesized and (b) & (d) 18 months later. The FET shows increasing source-drain current at more negative gate voltage, indicating p-type conduction in both measurements. The mobility and carrier concentration was derived from NW FET geometry and electrical properties(*126*). Directly after fabrication, the NW had a field effect mobility of 1.2 $cm^2V^{-1}s^{-1}$ and carrier concentration of 6.6×10^{17} cm^{-3} (*117*). Eighteen months later, after sitting in air and at room temperature, the same FET had a moderately reduced field effect mobility of 0.7 $cm^2V^{-1}s^{-1}$ and carrier concentration of 1.2×10^{17} cm^{-3}. Imperfect packaging of the FET may have caused the slight decrease in mobility and carrier concentration, but the *p*-type character is stable over an 18-month period.

In this study, aberration-corrected STEM was used to experimentally test the hypothesis of the origin of *p*-type conductivity in Sb-doped ZnO NWs: point defect complexes predicted by first principle calculations mentioned above. Within the experimental detection limits, no point defect complexes were observed in the Sb-doped ZnO NWs despite their predicted visibility using state of the art STEM image simulations. Instead, all the Sb is contained in Sb-decorated head-to-head (H-H) (0001) basal plane inversion domain boundaries (b-IDBs) that are present under the growth surface and at the bottom facet of internal voids in the NWs. Density functional theory (DFT) calculations support the hypothesis that the Sb-containing b-IDB defects are responsible for the *p*-type conduction of NWs. The H-H b-IDBs incorporate an extra

basal plane of O compared to the ZnO host lattice, codoping the ZnO with Sb and O, which, according to DFT calculations, makes them electron acceptors(*1*).

4.2. Material Synthesis

Fei Wang synthesized the Sb-doped ZnO NWs on silicon substrates with a ZnO seed layer grown from a zinc acetate ethanol solution(*117*). The substrates were placed on the surface of a solution consisting of 25 mM sodium nitrate, 25 mM hexamethylenetetramine, and an Sb-dopant solution for one day at 90 °C to induce NW growth. The Sb-dopant solution contained sodium glycolate, created from equal molar sodium hydroxide and glycolic acid, and antimony acetate in a ratio of 12:1. After synthesis, NW samples were treated with oxygen plasma to remove surface organics. To help activate the *p*-type dopants, NW samples were annealed in argon at 850 °C for 30 minutes. More information about the growth of the NWs can be found elsewhere(*117*).

4.3. Procedures

Aberration-corrected HAADF STEM was used to image the Sb-doped ZnO NWs and the Z-contrast effect was used to distinguish the Zn and Sb atomic columns. STEM experiments were conducted using the typical STEM imaging conditions discussed in Chapter 2.4. STEM samples were prepared by scratching NWs off the Si substrates with a fine needle onto non-porous 5 nm thick Si membrane window grids. Prior to STEM experiments, samples were plasma cleaned in a Fischione plasma cleaner in 25% oxygen - 75% argon mixture for ~5 minutes to eliminate organic carbon surface contamination.

The STEM images presented here were smoothed with a Gaussian smaller than the probe size to reduce image noise.

Brian Puchala and Dane Morgan conducted the DFT calculations to obtain the relaxed structure and charge distribution of both head-to-head and tail-to-tail b-IDBs. DFT(*127*) was implemented in the Vienna Ab Initio Software Package (VASP)(*128–132*) using the Perdew, Burke, and Ernzerfhof (PBE)(*133*, *134*) generalized gradient approximation (GGA) exchange-correlation functional. The errors in the band gap of ZnO due to inadequate repulsion between Zn *3d* and conduction band levels were treated with the GGA+U correction(*135*) and U-J = 7.5 eV(*136*) so that the valence band and Zn *3d* energy levels match experiment and self-interaction corrected calculations. A plane-wave energy cutoff of 600 eV and a 7x5x3 Monkhorst-Pack *k*-point mesh was used.

PACBED patterns were simulated using the frozen phonon multislice technique(*55*) to compare to experimental PACBED patterns to determine the ZnO NW polarity. Zn-polar ZnO PACBED patterns were calculated using Debye−Waller factors for ZnO from Reid(*79*), averaged over one ZnO $[11\bar{2}0]$ unit cell and 16 phonon configurations.

4.4. Defects Responsible for *p*-type Conduction in ZnO NWs

Figure 4.5(a) is a $<11\bar{2}0>$ projection HAADF STEM image of a Sb-doped NW tip ([0001] growth direction points up), showing a terraced surface and Sb-decorated b-IBDs 2-3 planes under the (0001) growth surfaces, as marked by the yellow arrows. Figure 4.5(b) is a $<10\bar{1}0>$ projection HAADF STEM image of a different Sb-doped NW

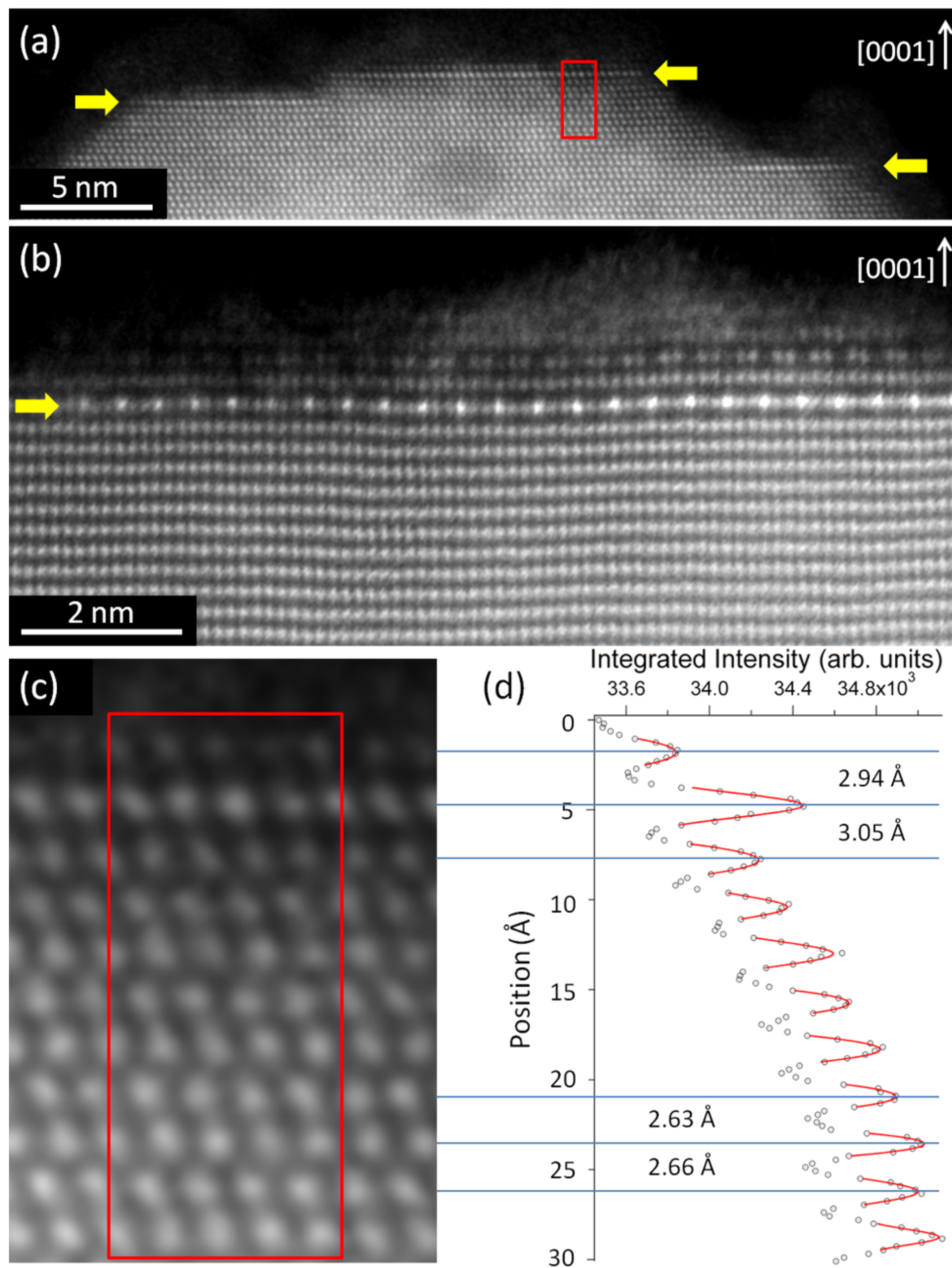

Figure 4.5: (a)-(c) HAADF STEM images with the growth direction up in every image. (a) and (b) are images of NW tips in the (a) <11$\bar{2}$0> and (b) <10$\bar{1}$0> projections, revealing Sb-decorated b-IDBs, marked by yellow arrows. (c) Higher magnification image of the region surrounding the red box in (a). (d) Integrated line profile of the region inside the red box in (c), revealing the lattice expansion around the IDB.(*1*)

tip, showing another Sb-decorated b-IBD, also marked with a yellow arrow. Because these are Z-contrast HAADF images, the difference in atomic number between O, Zn, and Sb means that the pure O columns are invisible and the Sb-containing atomic columns are brighter than the regular Zn lattice atomic columns. In both projections of

Figures 4.5(a) and (b), the (0001) stacking sequence and atomic column positions across the IBD match previous reports of Sb-decorated b-IBDs in ZnO(*137–140*). In the <$10\bar{1}0$> projection of Figure 4.5(b), the Sb-decorated (0001) plane has every third atomic column brighter, since in this projection pure Sb atomic columns are separated by two pure Zn atomic columns(*137–140*). In the <$11\bar{2}0$> projection image of Figure 4.5(a), the atomic columns of the Sb-decorated (0001) plane are mixed Zn and Sb in the ratio of 2 to 1, explaining their lower contrast compared to the contrast of Sb atomic columns in Figure 4.5(b).

Figure 4.6(a) and (c) are HAADF STEM images (with the [0001] growth direction pointing up) of Sb-doped NWs showing the size and location of voids and internal b-IDBs. Figure 4.6(a) shows that the NWs have voids 2 - 20 nm in diameter at least 15 - 20 nm away from the NW side surfaces. These features have been confirmed as voids by TEM over/under focus images displaying the characteristic Fresnel fringe contrast reversal(*141*), as shown in Figure 4.7(a)-(c). Figure 4.6(c) shows a <$10\bar{1}0$> projection image revealing an Sb-decorated b-IDB sitting just below the bottom (0001) facet of a void inside a NW, as marked by the yellow arrow. The contrast of the Sb-decorated b-IDB plane in Figure 4.6(c) is lower than in Figure 4.5 because Figure 4.6(c) is a thicker part of the NW compared to Figures 4.5 and the b-IDB does not penetrate

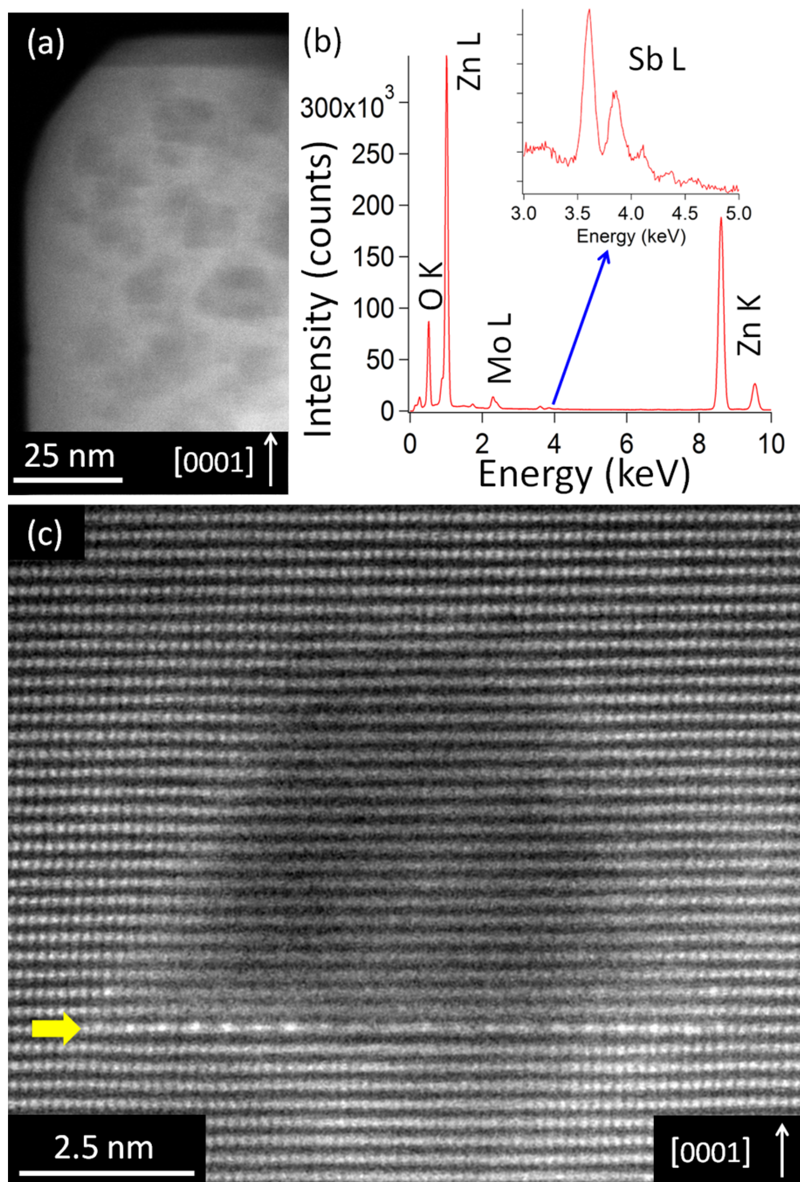

Figure 4.6: (a) HAADF STEM image of a NW showing the position and size of internal voids (the areas with darker contrast). The [0001] growth direction points up in the image. (b) Integrated STEM EDS spectrum image of one NW revealing the presence of Sb with an Sb/Zn ratio of ~0.58 at %. (c) <10$\bar{1}$0> projection HAADF STEM image of a void showing an Sb-decorated H-H b-IBD marked with a yellow arrow just below the bottom facet of the void.(*1*)

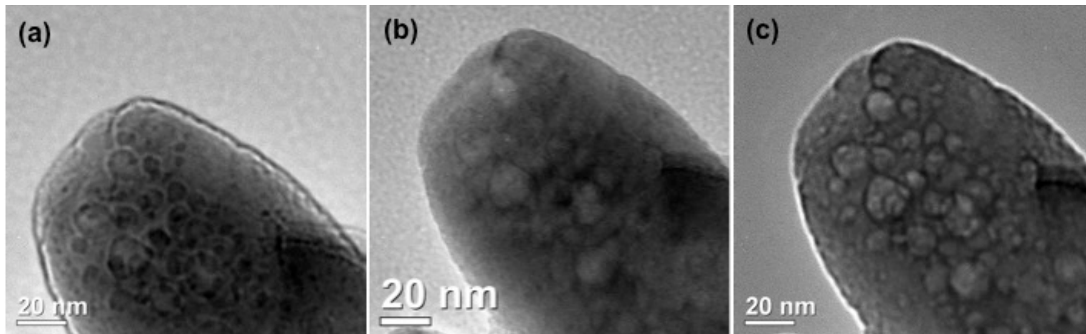

Figure 4.7: TEM images of a Sb-doped ZnO NW tip in (a) under focus, (b) in-focus, and (c) over-focus imaging conditions. The Fresnel fringe contrast reversal around the interior features indicate that they are voids.

through the entire thickness. Every NW we examined across different growth batches contained similar growth tips, voids, and b-IDBs.

To the best of our detection limits, our results indicate the b-IDBs incorporate all of the Sb present in the NWs. Figure 4.6(b) shows an integrated STEM EDS SI of one NW showing it contains an Sb/Zn ratio of ~0.58 at %, consistent with Wang *et al.*(*117*) STEM EDS in regions without b-IDBs near the edges of the NWs show no Sb peak, although the minimal detectable Sb concentration is limited by the poor counting statistics achievable without substantial beam damage. We have acquired HAADF STEM images of single substitutional and interstitial Sb atoms in Sb-doped thin films, confirming their detection with this technique is possible. However, we searched ~10^{-15} cm^3 of NW thin edges and found no single Sb atoms in HAADF STEM images like that shown in Figure 4.8. This implies the concentration of substitutional Sb and Sb-containing point defect complexes is less than 10^{15} cm^{-3}, and at least two orders of magnitude less than the measured carrier concentration. Therefore it is probable that the

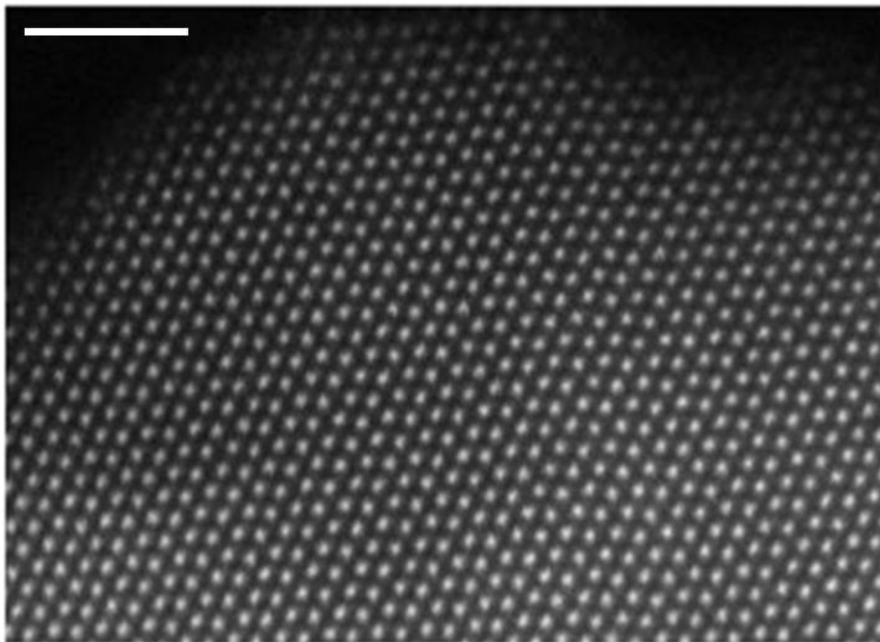

Figure 4.8: HAADF STEM image (not smoothed) of a very thin (2-5 nm) area of an Sb-doped ZnO NW. No signs of Sb-defect complexes are visible. Scale bar is 2 nm.

previously proposed mechanisms of Sb defect complexes for *p*-type conduction in Sb-doped ZnO(*122*) are not responsible for the *p*-type conduction in these NWs.

There are two types of b-IDBs in ZnO, with the structures shown in DFT relaxed supercell of Figure 4.9(*137*, *140*). Head-to-head (H-H) b-IDBs switch the polarity from Zn-polar to O-polar across the (0001) boundary, and tail-to-tail (T-T) b-IDBs switch the polarity from O-polar to Zn-polar. The H-H b-IDB incorporates an extra plane of O, creating octahedrally coordinated Zn and Sb in the defect plane. The T-T b-IDB is O deficient, so the Zn and Sb remain tetrahedrally coordinated. To satisfy periodic boundary conditions, the supercell in Figure 4.9 contains one H-H and one T-T b-IDB. The total stacking sequence is AB(H-H)$A^{-1}C^{-1}A^{-1}C^{-1}$(T-T)BAB, where $^{-1}$ indicates planes of opposite polarity. In the DFT relaxed structure, the H-H b-IDB causes a substantial

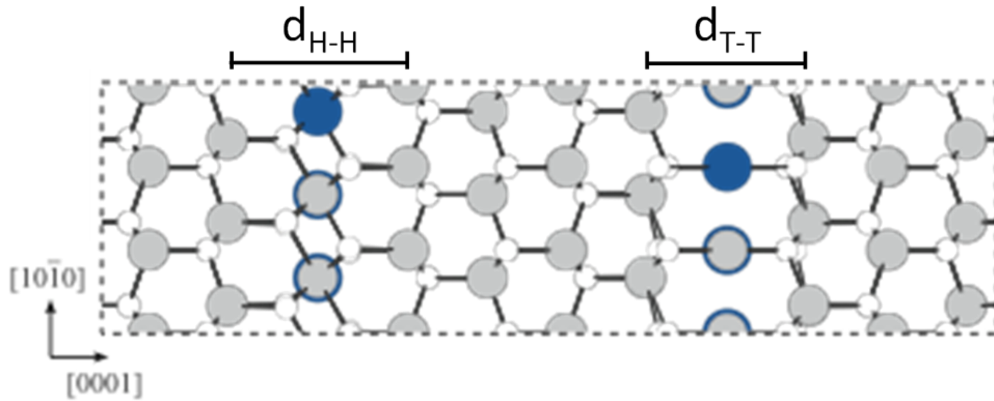

Figure 4.9: Supercell structure containing both a H-H and T-T b-IDBs with the stacking sequence AB(H-H)$A^{-1}C^{-1}A^{-1}C^{-1}$(T-T)BAB, where $^{-1}$ indicates planes of opposite polarity. Grey atoms are Zn. White atoms are O. Blue atoms are Sb in the b-IBD plane. Grey atoms with blue circles are Zn in the b-IDB plane.(*1*)

lattice expansion, with a distance of d_{H-H} = 5.95 Å between the two (0001) Zn planes on either side of the defect. This expansion is due to the larger size of the Sb ions and the extra O plane. The T-T b-IDB distance is d_{T-T} = 5.38 Å, and the un-defected crystal *c* lattice parameter is 5.14 Å. We also used DFT to relax a slab structure with the stacking sequence AB(H-H)$A^{-1}C^{-1}$ which contains a single H-H b-IDB and a free surface. The H-H basal plane spacing in the slab geometry is d_{H-H} = 6.04 Å. The good agreement between the slab and supercell d_{H-H} indicates that the lattice expansion is not a result of interacting H-H and T-T b-IDBs in the supercell.

The NW polarity, and therefore the b-IDB nature, cannot be directly determined from the HAADF STEM images because the O sub lattice is not visible, but comparison of the experimental and DFT calculated b-IDB expansion shows that the NWs contain H-H b-IDBs. Figure 4.5(c) is part of a higher magnification STEM image corresponding to the red box in Figure 4.5(a). Figure 4.5(d) is an integrated line profile of the raw (not

smoothed) STEM image from the red box. The NW gets thinner towards the tip producing a steady slope in the line profile. In order to locate each atomic column maximum with sub-pixel accuracy, the peaks were fit to a Gaussian, as shown by the red profiles in Figure 4.5(d). The Sb-decorated (0001) plane corresponds to the higher peak compared to its neighbors at 5 Å in the line profile. The b-IDB spacing is 5.99 ± 0.04 Å, as measured from the neighboring (0001) Zn planes. The average ZnO lattice parameter is c = 5.21 ± 0.02 Å, determined by doubling the average of the bottom 5 separations. The reported uncertainties are propagated from the uncertainties in the Gaussian center positions estimated from the fit.

The comparison of the experimental b-IDB spacing to the H-H and T-T b-IDBs separations from the DFT calculations confirm our NWs contain H-H b-IDBs. The experimental b-IDB spacing nearly perfectly agrees with the DFT calculated $d_{H\text{-}H}$ from the supercell and slab models. The experimental c lattice parameter agrees with previous experiments (c = 5.207 Å from Chen *et al.*(*84*)) and is slightly larger than the DFT calculated c, implying the outstanding agreement between STEM and DFT on the b-IDB H-H spacing is partially by chance. However, the difference in the simulated $d_{H\text{-}H}$ and $d_{T\text{-}T}$ of 0.57 Å is significantly larger than the experimental uncertainties and the discrepancy in the c axis lattice parameter, proving the experiments disagree with the smaller $d_{T\text{-}T}$. Other b-IDB images, such as Figure 4.6(c), show similar b-IDB lattice expansions, as does a similar expanded 6.20 ± 0.30 Å lattice across In-decorated H-H b-IDBs in ZnO NWs(*142*, *143*).

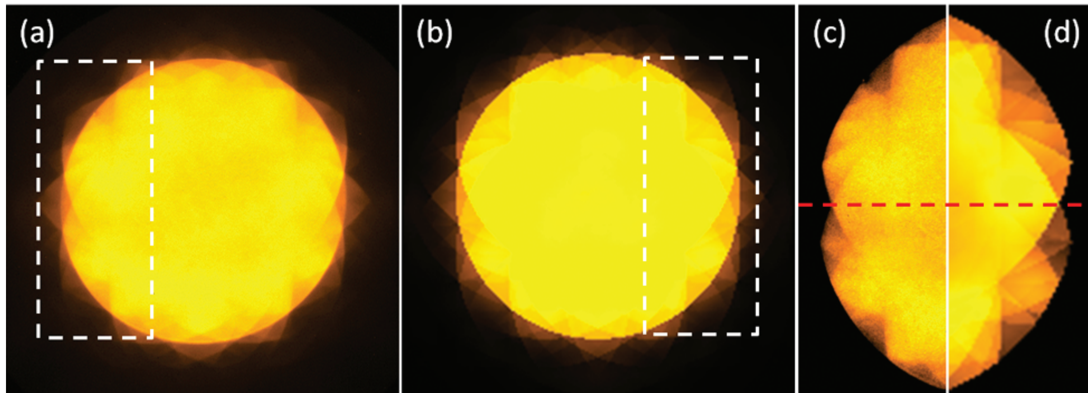

Figure 4.10: (a) Experimental PACBED pattern acquired near the edge of a NW away from voids and b-IDBs with the growth direction pointing up. (b) Simulated PACBED pattern of a 12.5nm $[11\bar{2}0]$ Zn-polar ZnO model using the frozen-phonon multislice algorithm. (c) and (d) Enlargements of the white dotted rectangles in (a) and (b), respectively. The match in asymmetry across the horizontal red dotted line in (c) and (d) show that the NWs are Zn- polar.(*1*)

Figure 4.10 shows experimental and simulated PACBED patterns confirming the NWs are Zn-polar. As discussed in chapter 2.4, PACBED allows for accurate measurement of sample thickness and polarity by comparing experiments to simulations(*49*, *53*). Figure 4.10(a) shows an experimental PACBED pattern acquired near the edge of a NW away from voids and b-IDBs with the growth direction pointing up. Figure 4.10(b) shows a simulated PACBED pattern of Zn-polar ZnO with a thickness of 12.5 nm. A simulated sample thickness of 12.5 nm gives the best agreement with the experiment. Figures 4.10(c) and (d) are enlargements of the white dotted rectangles in Figures 4.10(a) and (b) respectively, contrast stretched to emphasize the pattern asymmetry caused by the polarity. The matching asymmetry across the horizontal red dotted lines in Figures 4.10(c) and (d) indicate the NWs are Zn-polar. In addition to the enhanced lattice expansion around the b-IDBs, these PACBED patterns provide evidence

supporting the presence of H-H b-IDBs and not T-T b-IDBs.

It is not possible to directly explore the electronic levels of the b-IDB with DFT because a single b-IDB cannot be isolated in a periodic supercell and there are significant surface effects in the slab geometry. We indirectly investigated the electrical activity of the b-IDBs by integrating the charge density within the Voronoi polyhedra surrounding each atom and assigning that net charge to the atom. Including the nuclear charge, H-H b-IDBs have a net negative charge of -1.46e per $SbZn_2O_6$ unit in the slab geometry and -1.68e per $SbZn_2O_6$ unit in the supercell geometry. T-T b-IDBs have a net positive charge of +1.96e per $SbZn_2$ unit (or +1.62e per $SbZn_8O_6$ unit if the neighboring planes are included in the T-T b-IDB) in the supercell geometry. These results indicate that H-H b-IDBs would act as acceptors and that T-T b-IDBs would act as donors, implying a structure containing more H-H b-IDBs would be net *p*-type, although not every electron captured by the H-H b-IDBs is likely to generate a free hole. This method of forming *p*-type ZnO is essentially O-doping of the material that is stabilized by Sb co-doping through the creation of stable Sb-decorated H-H b-IDBs.

The NWs contain only H-H b-IDBs, which stands in contrast to thin film and bulk bulk Sb-doped ZnO. Thin film and bulk Sb-doped ZnO contains H-H b-IDBs, T-T b-IDBs, $\{10\bar{1}0\}$ IDBs, and $\{10\bar{1}1\}$ IDBs(*144*). The predominantly H-H character of the b-IDBs in our NWs are explained by their appearance below the bottom (0001) facets of voids, as shown by Figure 4.6(c). If the NWs did not contain voids and were solid material throughout, they would need T-T b-IDBs or some other plane IDB after a H-H b-IDBs to switch the polarity from O-polar back to Zn-polar before there could be

another H-H b-IDB. The H-H b-IDBs create O-polar material that is terminated almost immediately after a few monolayers by the voids bottom (0001) surface. The Zn-polar material surrounding the b-IDBs topped with O-polar ZnO overgrows the b-IDB region by forming a void over it because Zn-polar ZnO grows faster than O-polar ZnO(*145*). The NW maintains its Zn-polar nature past the void, requiring b-IDBs further up the wire to be again H-H. The lack of the $\{10\bar{1}0\}$ IDBs, and $\{10\bar{1}1\}$ IDBs that are found in bulk and thin film Sb-doped ZnO could be related to strain reduction at the high density of interior void and NW surfaces.

The internal voids' size and position could be beneficial to the electrical transport properties of the NWs. The voids and internal H-H b-IDBs have a lateral size of 2 - 20 nm, which is small compared to the 50 - 120 nm NW diameter. Therefore, holes created by the H-H b-IDBs do not have to travel far to escape the extended defects and contribute to conduction. This is in contrast to b-IDBs in In-doped ZnO NWs, which span the whole width of the NWs(*142*). In addition, neither the voids nor IDBs are located near the NW surface. Because conduction in ZnO NWs is dominated by surface conduction(*146*, *147*), the voids and b-IBDs should not significantly decrease the carrier mobility. A similar scheme could be used for creating *p*-type ZnO thin films by utilizing atomically abrupt delta doping with Sb to create holes through a single H-H b-IDB separated from, but close to, a high mobility conduction path. More recently, we studied Sb-doped ZnO thin films and found no IDB structures and n-type behavior(*148*). Sb was found to act as a donor and predominantly occupy Zn positions(*148*).

4.5. Conclusions

By using aberration-corrected HAADF STEM we discovered that all of the Sb (within our detection limits) in Sb-doped ZnO NWs is contained in Sb-decorated H-H b-IDBs just under the (0001) growth surfaces and the (0001) bottom facets of interior voids. We find no evidence for Sb-containing point defect clusters. According to DFT calculations, the extra basal plane of O per H-H b-IDB accepts electrons, explaining the *p*-type character of the ZnO NWs. Electrical measurements of a single NW FET shows stable *p*-type conduction over 18 months. This new mechanism for producing *p*-type character in ZnO is made possible by the NW void morphology. The confined lattice of ZnO NWs offers an environment that stabilizes the O and Sb-decorated b-IDBs and the NW voids allow for the presence of only the acceptor H-H b-IDBs. This discovery suggests new possibilities for realizing ZnO based *p-n* homojunction devices(*118*, *149–151*).

Chapter 5: Composition Variation in InGaN Quantum Well LEDs

5.1. Introduction

InGaN quantum wells (QWs) in GaN, utilized in blue to ultraviolet light emitting diodes (LEDs) and lasers, are attractive because they can be operated in high power and high temperature applications, and they have long lifetimes, extremely high internal quantum efficiencies (>90%), and tunable emission wavelengths(*152–155*). However, GaN exhibits a high density of threading dislocations (typically 10^{10} cm^{-2}) that originate at the heteroepitaxial GaN/substrate interface(*156*). Extensive efforts have been made to reduce the density of threading dislocations, such as incorporating SiN_x nanonetworks, but densities of 10^7-10^8 cm^{-2} remain in state of the art devices(*157*). In other III-V semiconductor LEDs, threading dislocation densities of this magnitude are more than enough to quench emission if they are effective non-radiative recombination sites.

InGaN based devices have also been reported to have lateral In composition fluctuations within the plane of the QWs(*158–161*), that are potentially created from a InN-GaN miscibility gap(*162*, *163*). Various characterization techniques, including high-resolution TEM(*164*, *165*), energy filtered TEM(*161*), and EDS(*158*), showed the presence of lateral In composition fluctuations. After these reports, Smeeton *et al* showed evidence for electron beam induced lateral In segregation that is not present in unirradiated InGaN QWs(*166*). These results call into question whether the previous conclusions were true in unirradiated samples or were caused by electron beam irradiation. In addition to lateral In composition variation, well width variations are

another proposed microstructural feature that could confine carriers away from threading dislocations(*167*).

In this study, we use aberration-corrected STEM to show that no lateral In composition fluctuations exist in $In_{0.20}Ga_{0.80}N$ layers at the length scales previously reported. The STEM experiments were done at a controlled electron dose well below the reported damaging dose for InGaN QWs. PACBED is used to confirm that the TEM specimen is sufficiently thin to ensure images could detect small scale In composition fluctuations if they existed. In addition to disproving small-scale lateral In composition variation, we also show evidence for InGaN QW well-width variations of 3-4 atomic planes. Combining aberration-corrected STEM and STEM EDS SI allowed us to measure the In segregation at prevalent defects in InGaN LEDs, including dislocations and V-defects. We also observe, but cannot yet explain, extra vertical In composition variations in nominally $In_{0.01}Ga_{0.99}N$ layers.

5.2. Material Synthesis

The InGaN based LED samples we examined were grown by Hadis Morkoc's group at Virginia Commonwealth University. They consisted of (0001) sapphire/GaN template (3.7 μm) / GaN buffer (1.5 μm) / $In_{0.01}Ga_{0.99}N$ (60 nm) / $In_{0.04}Ga_{0.96}N$ (5 nm) / $In_{0.08}Ga_{0.92}N$ (5 nm) / $In_{0.20}Ga_{0.80}N$ (9 nm) / $In_{0.01}Ga_{0.99}N$ (3 nm) / 30×($Al_{0.05}Ga_{0.95}N$/GaN) / GaN:Mg (9 nm) / Ga-doped ZnO transparent conducting oxide top contact. The InGaN active region of this device was deposited by vertical low-pressure metal organic vapor

phase deposition and a schematic of the structure is shown in Figure 5.1(b). Additional details of the device synthesis and performance may be found elsewhere(*168*).

5.3. Procedures

STEM samples were prepared in the $[11\bar{2}0]$ projection by mechanical wedge polishing(*169*), followed by ion milling for final thinning at 4 keV and 1.5 keV in a Fischione 1010, and 900 eV and 500 eV in a Fischione Nanomill. The FIB sample was prepared using a FEI Helios NanoLab 450S DualBeamTM and an in situ lift-out technique(*170*) by Brandon Van Leer at FEI Company. The sample was thinned to ~100 nm using a 30 keV, 230 pA Ga+ beam, then polished at 3 and 1 keV with a 50 pA beam in the FIB to the final thickness. The 1 keV final polish is essential to avoid Ga surface damage in InGaN regions of the sample. The typical STEM imaging conditions discussed in chapter 2.4 were used. STEM EDS SI experiments were performed on the FEI Titan STEM operated at 200 keV with a 24.5 mrad convergence angle and 800 pA probe current. These conditions give a STEM spatial resolution of 2.1 Å.

PACBED simulations, based on the Kirkland frozen-phonon multislice algorithm(*55*), were utilized to determine sample thickness and polarity. They were calculated using Debye-Waller factors for GaN from Xiong and Moss,(*171*) averaged over one GaN $[11\bar{2}0]$ unit cell with 25×25 probe positions and 16 phonon configurations.

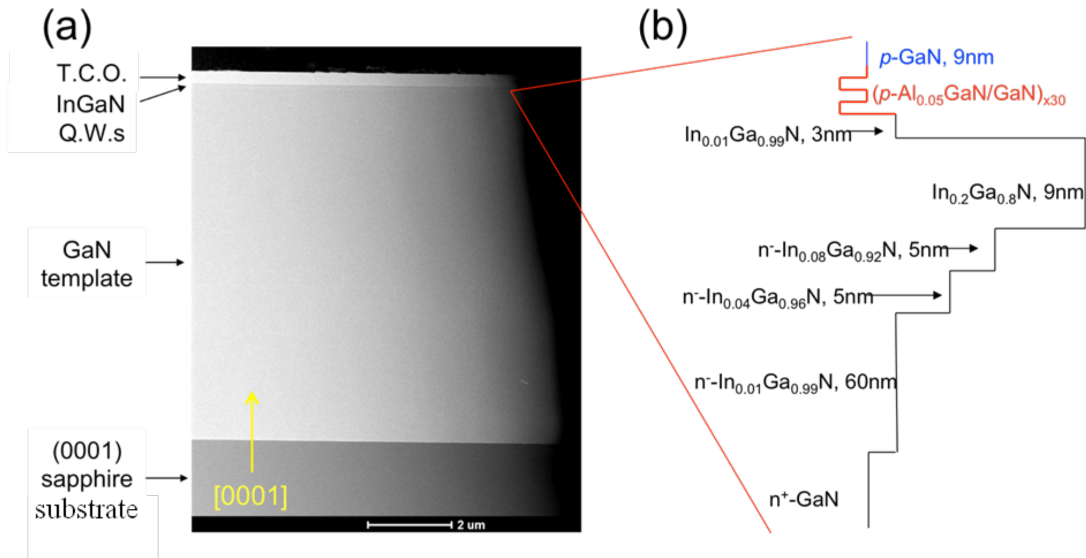

Figure 5.1: (a) A HAADF STEM image along $[11\bar{2}0]$ of the InGaN quantum well based LED with the various layers labeled on the left. (b) A schematic of the InGaN LED region as described in Chapter 5.2.

5.4. In Composition Variation in InGaN QW LED Structures

Figure 5.1(a) shows a low magnification HAADF STEM image of the whole InGaN / GaN based LED structure. As labeled in Figure 5.1(a), the bottom layer is the sapphire substrate, the next layer up is the GaN template, followed by the InGaN layers which are barely visible, and capped with Ga-doped ZnO. Figure 5.1(b) shows a schematic of the InGaN layers described in the materials synthesis section.

Figure 5.2 shows a typical high-resolution STEM image along $[11\bar{2}0]$ of the $In_{0.20}Ga_{0.80}N$ QW region of the LED. The regions above and below the quantum well are $In_{0.01}Ga_{0.99}N$ and $In_{0.08}Ga_{0.92}N$ respectively. It shows atomically smooth interfaces with some relatively weak contrast inside the quantum well. However, the regions above and below the quantum well also show the same contrast in terms of length scale and

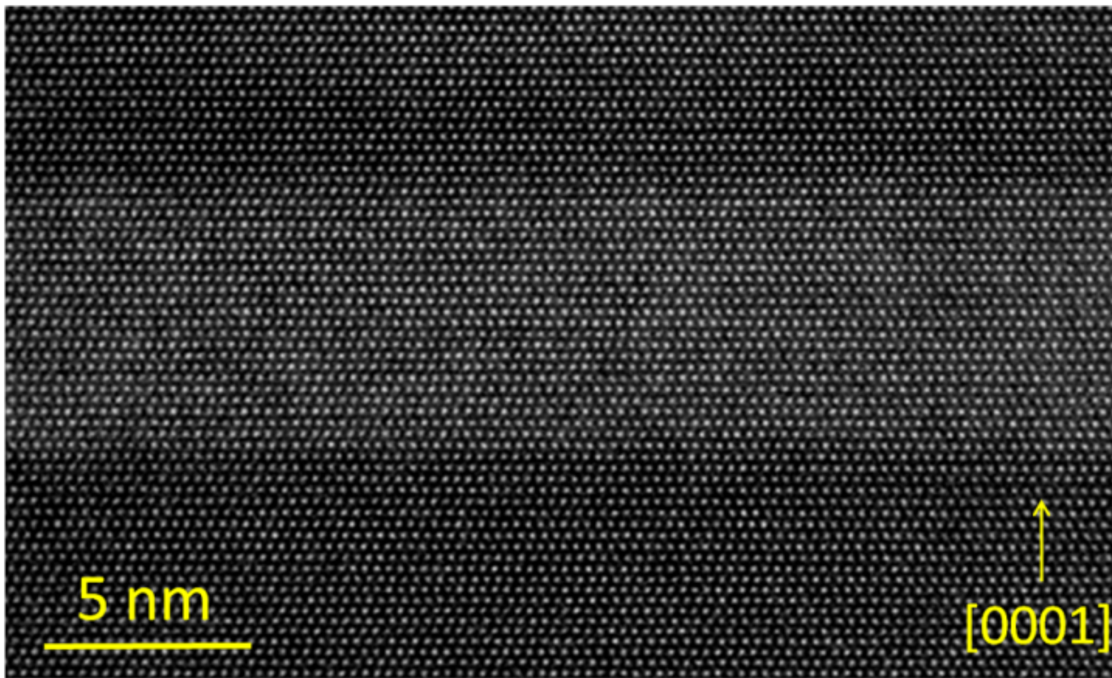

Figure 5.2: A HAADF STEM image along $[11\bar{2}0]$ of the $In_{0.20}Ga_{0.80}N$ quantum well region of the LED. This image was smoothed with a Gaussian smaller than the probe size to reduce noise.(*267*)

intensity. This contrast arises from surface damage left over from the sample preparation, such as oxidation or amorphization, not from In composition fluctuations. Similar images have been acquired from nearby areas of this LED, other TEM samples prepared from the same LED, and LEDs grown at different times in the same reactor.

Figure 5.2 was acquired at a low enough dose to supply an image that is representative of the intrinsic structure of the sample. Figure 5.2 represents the first time that area of the sample was irradiated by the electron beam. The dose incident on a sample (d) is calculated from the probe current (c), image acquisition time (t) and image area (A) by $d = ct/A$. For the image in Figure 5.2, $A = 4.2 \times 10^{-11}$ cm^2, $t = 16.77$ s, and $c =$ 24.5 pA, so $d = 10$ C/cm^2. We calculate that the dose Smeeton *et al.* used to observe

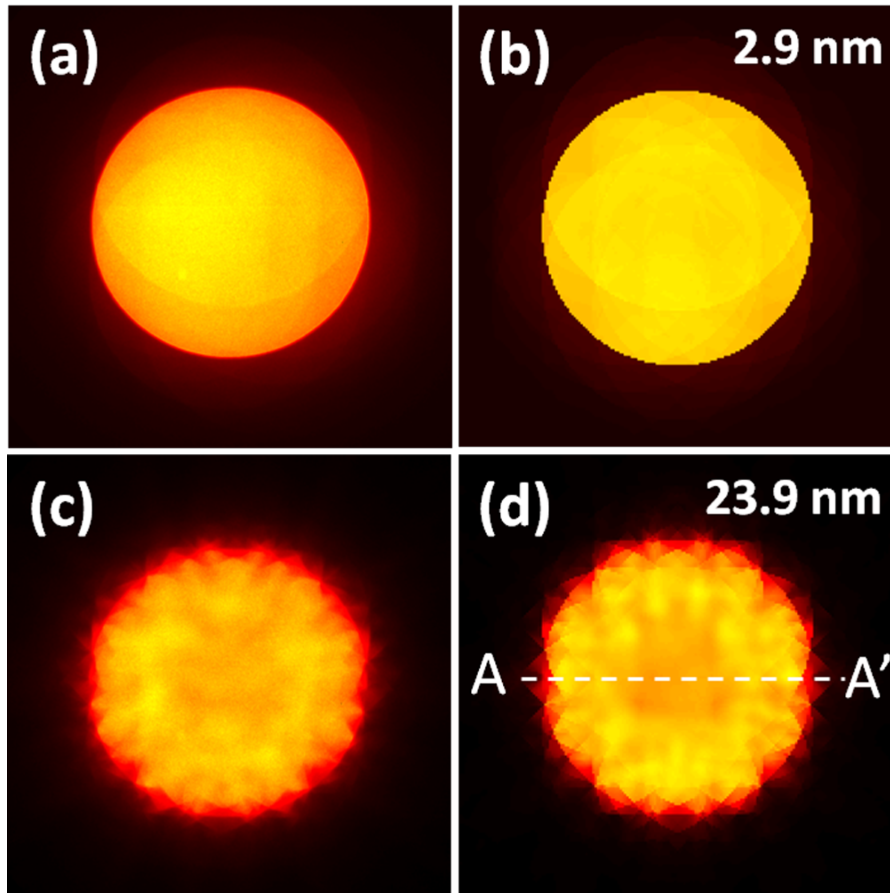

Figure 5.3: (a) Experimental and (b) simulated PACBED patterns of GaN $[11\bar{2}0]$, indicating that the experimental sample in Figure 3.2 is 2.9 nm thick. (c) Experimental and (d) simulated PACBED patterns, indicating the GaN is Ga-polar.(*267*)

composition fluctuations is 1,050 C/cm^2, also at 200 kV, so Figure 5.2 was acquired with 1% of the reported damaging dose in InGaN.

Figure 5.2 was acquired from a thin enough region of the sample to reveal the intrinsic structure of the $In_{0.20}Ga_{0.80}N$ quantum well in this device. According to the log-ratio EELS method the sample has a thickness of 8.8 nm (0.08 inelastic mean free paths of 110 nm(*172*)), but, as described in Chapter 2.5, this is an upper bound on the

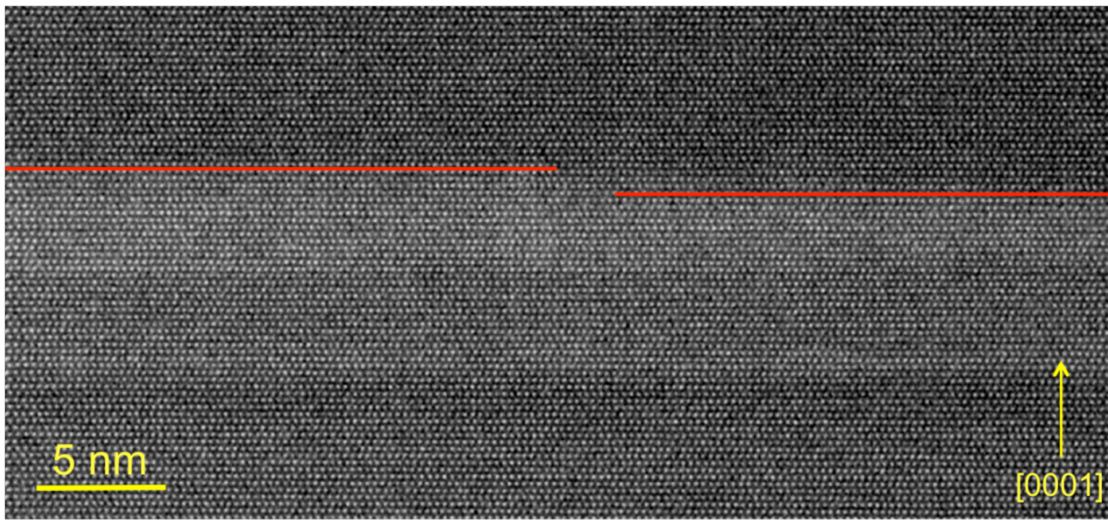

Figure 5.4: HAADF STEM image along $[11\bar{2}0]$ of a 5nm thick $In_{0.08}Ga_{0.92}N$ layer on top of a 5 nm thick $In_{0.04}Ga_{0.96}N$ layer showing a 3-4 monolayer step in the $In_{0.08}Ga_{0.92}N$ layer.(*267*)

thickness(*51*). Figure 5.3(a) is an experimental PACBED pattern from an area of the sample just below the quantum well near Figure 5.2. Figure 5.3(b) is a simulated GaN PACBED pattern of a sample 2.9 nm thick. A simulated sample thickness of 2.9 nm gives the best agreement with the experimental PACBED pattern in Figure 5.3(a). The sample in Figure 5.2 is only 2.9 nm thick, confirming it is thinner than the samples in other TEM reports of composition fluctuations(*165*). It is also thin enough to avoid the projection through several composition domains that could suppress contrast from composition fluctuations in thicker samples.

Figure 5.3(c) shows an experimental PACBED pattern from a thicker part of the same sample. Figure 5.3(d) is a multislice simulated PACBED pattern from a sample that is 23.9 nm thick and Ga-polar. The match between the experimental and simulated patterns reveals the experimental sample is 23.9 nm thick. More importantly, the match

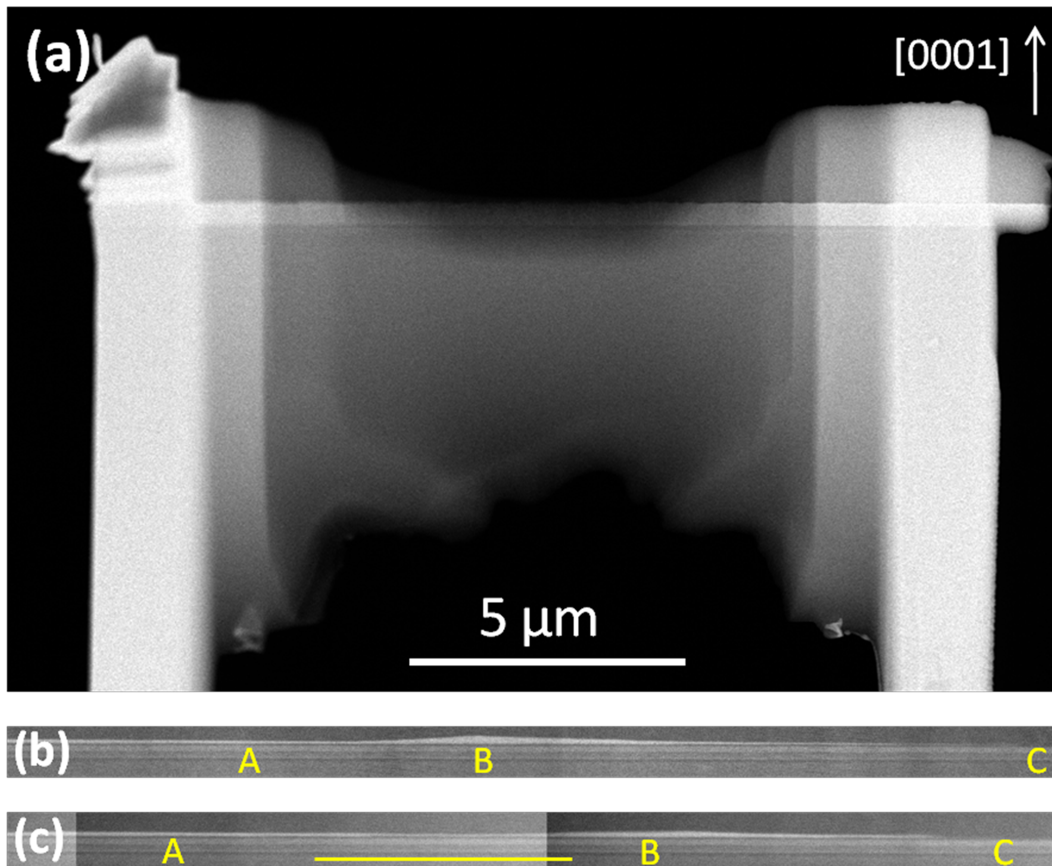

Figure 5.5: (a) A low magnification HAADF STEM image of a LEM sample prepared by the FIB lift-out technique. (b) and (c) Higher magnification HAADF STEM images of parts of the InGaN active region layers that are cropped from a larger stitched image. “A” marks regions of constant active layer thickness. “B” marks regions of thicker active layer. “C” marks regions of absent active layer. The yellow scale bar in (c) is 150 nm.(*267*)

between the asymmetry of the patterns along the line A-A’ in the figure reveals that the experimental sample is Ga-polar. This method provides an easy way to determine local material polarity.

Figure 5.4 shows a HAADF STEM image along $[11\bar{2}0]$ of a 5 nm thick $In_{0.08}Ga_{0.92}N$ layer on top of a 5 nm thick $In_{0.04}Ga_{0.96}N$ layer. This layer structure is part

of the InGaN LED layer structure discussed in Chapter 6. The image shows a 3-4 monolayer step in the $In_{0.08}Ga_{0.92}N$ layer, providing evidence for small-scale well thickness variations, which is another proposed mechanism for carrier confinement away from threading dislocations(*167*).

Figure 5.5(a) shows a low-magnification HAADF STEM image of a FIB lift-out prepared specimen. The thin area is over 3 μm wide, compared with a few hundred nanometers for normal wedge-polished specimens. Figures 5.5(b) and (c) are higher magnification HAADF STEM images that are cropped form a larger stitched image that shows significant variations in the thickness of a $In_{0.15}Ga_{0.85}N$ active layer. In regions such as the ones marked “A” in Figure 5.5(b) and (c), the active layer thickness is constant. In regions such as the ones marked “B”, the active layer thickness becomes substantially thicker. In regions such as the ones marked with “C”, it disappears entirely. The larger composite image contains four in-plane bounded active layer regions with lengths of 94, 280, 662, and 690 nm. The average length is 430 nm, consistent with the observations of Oliver et al (ref 2008).

Figure 5.6(a) shows a HAADF STEM image showing the whole InGaN layer structure. In the bottom 60 nm thick nominally $In_{0.01}Ga_{0.99}N$ layer there are 4 extra contrast bands that are marked with arrows. Figure 5.5(b) is an integrated line profile of Figure 5.6(a) along the [0001] growth direction that clearly shows the extra contrast bands. The extra bands have diffuse interfaces compared to the interfaces that were introduced deliberately. A STEM EDS SI of the same area is shown in Figure 5.6(c)-(f). Figure 5.6(c) is the simultaneous STEM image and (d)-(f) are background subtracted (d)

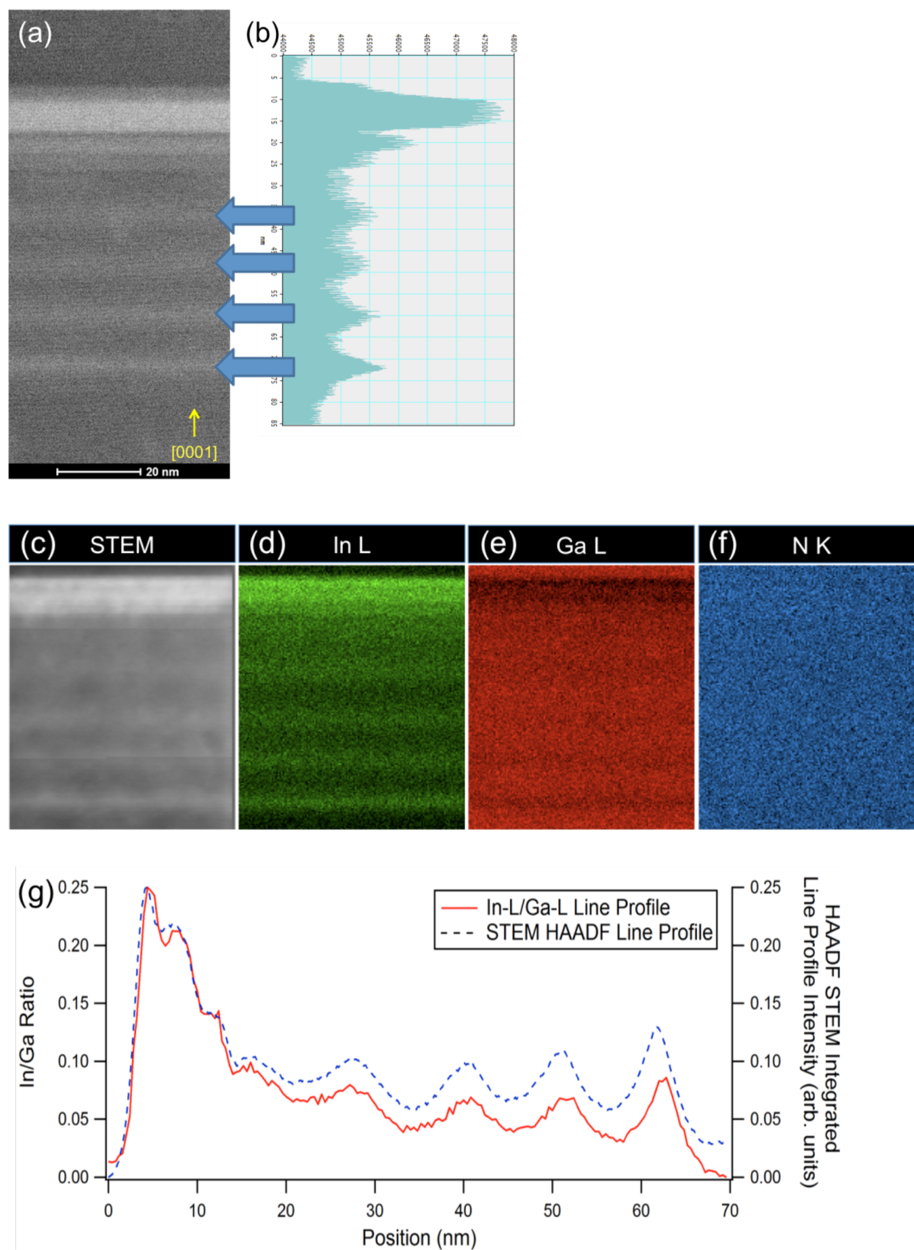

Figure 5.6: (a) HAADF STEM image of the InGaN LED region. (b) The integrated line profile along the [0001] growth direction of (a). There are 4 extra contrast bands in the $In_{0.01}Ga_{0.99}N$ layer, as marked by the arrows. (c) The simultaneous STEM image acquired during the STEM EDS SI. (d)-(f) Background subtracted (d) In L, (e) Ga L, and (f) N K edge intensity maps. (g) Integrated line profiles of the In/Ga ratio and HAADF STEM intensity along the growth direction.

In L, (e) Ga L, and (f) N K edge intensity maps. They reveal that the extra contrast bands are due to vertical In composition variation, which is consistent with the higher Z-contrast intensity. Figure 5.6(g) shows integrated line profiles of the HAADF STEM intensity and In/Ga ratio determined from EDS along the growth direction. There is a direct relationship between the In composition and extra contrast bands in the HAADF STEM image. It also reveals that the HAADF STEM image is way to image In composition. The dose required to acquire the STEM EDS SI was ~150,000 C/cm^2, four orders of magnitude higher than the dose required for the HAADF STEM image. The origin of these extra contrast bands is not understood, but the diffuse interfaces may suggest that they formed after deposition due to some diffusion process, such as spinodal decomposition.

Figure 5.7 shows data from an STEM EDS SI of the most prevalent defect in InGaN QWs, the V-defect(*173–178*). These defects form when threading dislocations intersect the InGaN QWs and open up into hexagonal inverted pyramid pits. When subsequent layers are deposited on top of the QWs, the pits are filled in. Figure 5.7(a) is a HAADF STEM image of a V-defect showing the threading dislocation above and below the V defect that caused its formation. Figure 5.7(b) is a background subtracted In L edge intensity map from a STEM EDS SI of the same V-defect. Figure 5.7(b) reveals that In segregates at the V-defect surfaces. An In depletion region is present under the V-defect surfaces, implying the In from this region has surface segregated and contributed to the large In intensity on the V-defect surfaces. Within the detection limits of EDS, there are no signs of In segregation at the threading dislocations. The threading

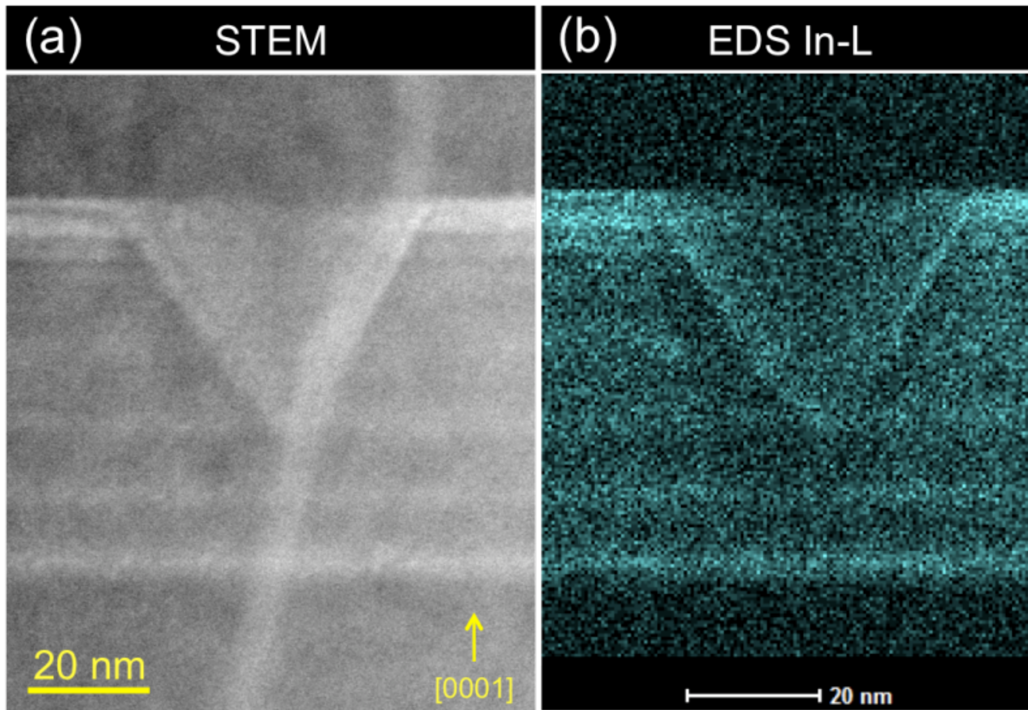

Figure 5.7: (a) HAADF STEM image of a V-defect in the InGaN QW region. (b) Background subtracted In L edge intensity map from a STEM EDS SI of the V-defect in (a).

dislocations have bright contrast in the STEM image because of sample strain producing diffraction contrast, not due to compositional Z-contrast from In.

5.5. Conclusions

We have shown that no lateral In composition fluctuations exist in $In_{0.20}Ga_{0.80}N$ layers at the length scales previously reported. The imaged area of the STEM sample was 2.9 nm thick, determined from PACBED. This is sufficiently thin to avoid the projection through several composition domains that could suppress contrast from composition fluctuations in thicker samples. The electron dose used to create the

reported images is 10 C/cm^2, which is 1% of the previously reported damaging dose in InGaN QWs. We also have shown evidence for 3-4 monolayer well thickness fluctuations, which has been proposed as a microstructural feature that could confine carriers.

STEM EDS SI reveal 4 vertical In composition fluctuations inside the 60 nm nominally $In_{0.01}Ga_{0.99}N$ layer. The origin of these composition fluctuations is not understood, but their diffuse interfaces suggest that diffusion may have occurred post deposition and spinodal decomposition could be a formation mechanism. STEM EDS SI also reveals no In segregation at threading dislocations, but does reveal In segregation at the surfaces of V-defects with an In depletion region below these surfaces.

Chapter 6: Extended Defects in InGaN Quantum Well LEDs

6.1. Introduction

As discussed in Chapter 5.1, III – nitride wide band gap semiconductors have large potential in optoelectronic device applications. A major component in the optimization of these devices efficiency and reliability is identifying and controlling extended defects. GaN extended defects include threading dislocations(*156*, *179*, *180*), stacking faults(*180*), open-core dislocations(*180–183*), inversion domain boundaries(*182*, *184*), V-defects in InGaN QWs(*173–178*), and pyramid shaped inversion domains and voids in Mg-doped GaN(*185–190*). Sapphire, GaN's most common substrate, and GaN are poorly matched in lattice parameter and thermal expansion coefficient, causing the interfacial region in as-grown films to have a high density of defects. The defect with the highest density is threading dislocations with densities as low as ~10^8 cm^{-2} for metal organic chemical vapor deposition (MOCVD) films grown on SiN_x nanonetworks(*157*). The threading dislocations are pure edge dislocations with a Burgers vector of 1/3<$11\bar{2}0$>(*156*, *179*, *180*). Open core dislocations, also called nanopipes, run in the [0001] growth direction and have hexagonal cross sections, $\{10\bar{1}0\}$ facets, and screw character with a [0001] Burgers vector(*180–183*). GaN inversion domains are similar to the nanopipes, but instead of having a voided core they contain GaN of the opposite polarity(*182*, *184*). Stacking faults are only present near the sapphire/GaN interface(*180*). V-defects were introduced and discussed in Chapter 5.4. Inverted hexagonal pyramid-shaped voids have been observed in Ga-polar Mg-doped GaN. These voids form from Mg-rich clusters below the pyramid tip and cause the void to open up

along the $\{11\bar{2}2\}$ or $\{11\bar{2}3\}$ planes(*185–190*). The void forms due to a polarity change across these planes to the slower growing N-polar GaN. When there is a lack of Mg on the defect walls, there is fast lateral overgrowth along the (0001) planes, terminating the defect.

Here, we report a pyramid-shaped void extended defect in InGaN and GaN not previously reported. The InGaN based LED devices examined here exhibited reduced performance and were grown side by side with high performance devices. In this study, we use various TEM techniques to elucidate the pyramid-shaped void defects responsible for the decreased device performance and propose a defect growth mechanism based on C contamination.

6.2. Material Synthesis

The InGaN based LED samples we examined were deposited using vertical low-pressure metal organic vapor phase deposition by Professor Morkoc's group at Viginia Commonwealth University. They consisted of (0001) sapphire / GaN template / GaN buffer (Si doped, $n \approx 2\text{-}3 \times 10^{18}$ cm^{-3}) (1.5 μm) / 10 x 6 nm $In_{0.08}Ga_{0.92}N$ layers separated by 10 nm $In_{0.01}Ga_{0.99}N$ barriers / $In_{0.04}Ga_{0.96}N$ (10 nm) / $In_{0.08}Ga_{0.92}N$ (10 nm) / p-type $Al_{0.15}Ga_{0.85}N$ (10 nm)/ p-type Mg-doped GaN (150 nm). The p-type Mg-doped GaN layer was deposited at 950°C and 150 Torr. More growth details and electrical, optical, and surface morphology properties can be found elsewhere(*74*, *168*).

6.3. Procedures

TEM and STEM samples were prepared for the $[11\bar{2}0]$ cross-section and [0001] plan-view projections by mechanical wedge polishing,(*169*) followed by ion milling for final thinning in a Fischione 1010 and Fischione Nanomill ion mills. The Fischione 1010 ion mill parameters for both top and bottom ion guns in order were, (1) 4 kV and 5 mA at a 9° angle from the surface for one hour, and (2) 1.5 kV and 5 mA at a 9° angle from the surface for 15 minutes. The Fischione Nanomill parameters in order were, (1) 900 V and 115 pA at a 10° angle from the surface for 25 minutes, (2) 500 V and 115 pA at a 10° angle from the surface for 25 minutes, (3) 900 V and 115 pA at a -10° angle from the other surface for 25 minutes, and (4) 500 V and 115 pA at a -10° angle from the other surface for 25 minutes. Samples were plasma cleaned in a Fischione plasma cleaner in 75% argon - 25% oxygen mixture for 5 minutes to eliminate organic carbon surface contamination immediately before STEM experiments.

TEM bright field experiments were performed on a Phillips CM200 microscope operated at 200 keV. STEM experiments were performed using the typical imaging conditions discussed in Chapter 2.4. MAADF STEM images were collected with a detector range of 28.8 - 143.8 mrad, allowing the detection of more diffracted electrons and causing enhanced strain contrast in the images. ABF STEM images were collected simultaneously with HAADF STEM images with an annular detector range of 11 to 24.1 mrad. STEM electron energy loss spectroscopy (EELS) spectrum images were acquired on the Titan using a 24.5 mrad probe semi-angle, 400 pA probe current, and STEM

resolution of 2.1 Å. The EELS data were de-noised using HREM Research's MSA Digital Micrograph plug-in, retaining nine principle components.

6.4. Void Defect in InGaN and GaN

Figure 6.1 shows atomic-resolution HAADF STEM images of a $[11\bar{2}0]$ cross-section sample. Figure 6.1(a) shows part of the n-type GaN, the whole InGaN QW structure, and the p-GaN top layers (the [0001] growth direction pointing upwards in the image). Small triangular shaped voids are present in the n-type GaN and InGaN QW structure, but not in the Mg-doped p-GaN top layer. Similar voids were observed below the imaged area of Figure 6.1(a) in the GaN all the way down to the sapphire/GaN interface, but not in the sapphire. The voids tend to form in similar (0001) planes perpendicular to the vertical growth direction in the images. Figure 6.1(b) is a higher magnification image of the QW structure showing the high In concentration layers as brighter bands due to the Z contrast and revealing the same voids. Figure 6.1(c) is an atomic-resolution STEM image showing a typical triangle void in GaN with a sidewall angle of ~58° to the (0001) base. Typical side wall angles range from 58° to 62° and void base lengths range from 5 to 75 nm, with a majority falling within the 5 to 25 nm range. The density of the voids varies within each sample, with some areas tens of square microns large have ~10^{15} cm^{-3} while other areas have none. Figure 6.1(a) and (b) show that some triangular shaped voids have vertical nanopipe caps that extend hundreds of nanometers upward. Figure 6.1(d) shows an atomic-resolution image of a typical void

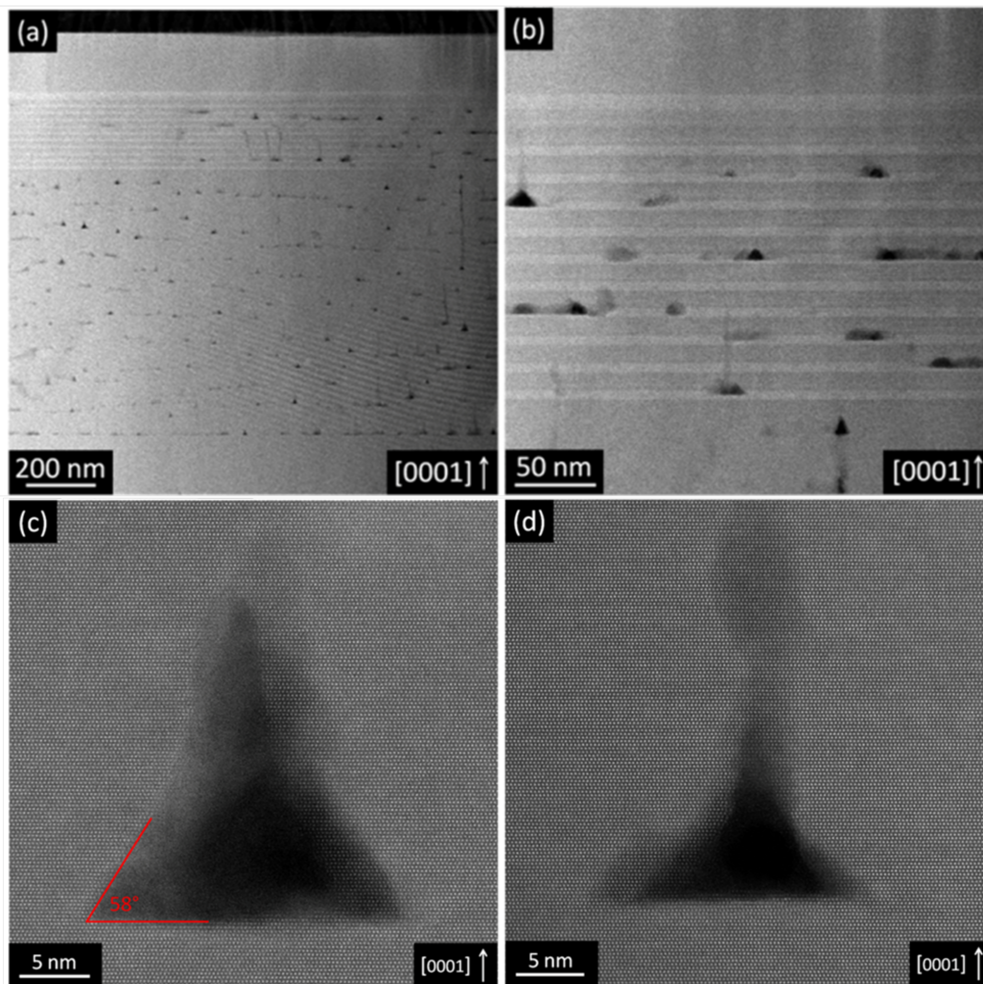

Figure 6.1. $[11\bar{2}0]$ cross-section HAADF STEM images with the growth direction pointing up. (a) shows voids in the GaN template and InGaN quantum well structure, but not the p-GaN top layers. (b) shows voids in the InGaN quantum wells. (c) and (d) are atomic-resolution images of pyramid voids. The apparent fringes in the bottom right of (a) are Moiré fringes between the square STEM scan and the underlying crystal lattice.(*77*)

with a vertical nanopipe cap. The lateral size of the nanopipe varies, but does not seem to grow larger than 10 nm.

Figure 6.2 shows simultaneously acquired HAADF and ABF $[11\bar{2}0]$ cross-section STEM images of GaN ([0001] growth direction pointing up in the image). Due to

the Z-contrast nature of the image, the atomic column positions in the HAADF image of Figure 6.2(a) represent the pure Ga columns, while the pure N columns are not visible. In the ABF STEM image in Figure 6.2(b), the pure Ga and pure N atomic columns are resolved and distinguishable. The Ga columns have higher contrast than the N columns due to its larger Z number, and are therefore the upper atomic columns in the dumbbells. The Ga positions in the HAADF STEM image in Figure 6.2(a) correlate to the larger atomic columns in the ABF image in Figure 6.2(b), also confirming the Ga and N column positions in the ABF image. ABF STEM imaging supplies an easily interpretable method to determine that our samples are Ga-polar, as shown in the model superimposed on Figure 6.2(b). This also confirms our polarity conclusions made from similar samples shown in Figure 5.3(c) and (d).

Figure 6.3 shows a (a) TEM image and (b)-(d) STEM images of a [0001] projection plan-view sample. The TEM image in Figure 6.3(a) reveals hexagonal Fresnel fringe contrast shapes, which arise due to diffraction from a sharp edge and are characteristic of embedded voids(*141*), and central contrast spots, which are characteristic of end-on dislocations. The extra background contrast in Figure 6.3(a) is a result of thickness fringes and bend contours that are typical in TEM images(*21*). Figure 6.3(b)-(d) are high-resolution MAADF STEM images emphasizing strain/diffraction contrast, which enhances the visibility of the voids. They show the hexagon Fresnel fringe contrast surrounding a central dislocation contrast spot. At larger HAADF detector angle ranges, like those used in Figure 6.1, the embedded voids in the plan-view samples are barely visible. Figure 6.3(a) and (b) shows that all the voids have hexagon bases and they

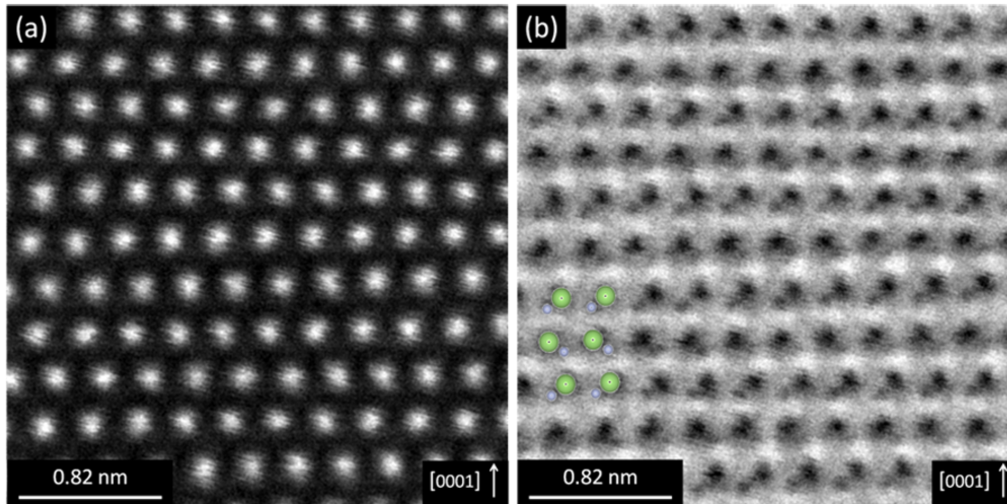

Figure 6.2. Simultaneously acquired (a) HAADF and (b) ABF $[11\bar{2}0]$ cross-section STEM images of GaN with the growth direction pointing up in the image, showing Ga polarity. A model of the Ga polarity atomic structure is superimposed on (b), with the larger green atoms being Ga and the smaller blue atoms being N.(*77*)

are oriented with respect to one another, implying some crystallographic facet preference of the formation mechanism. Figure 6.3(c) shows a higher magnification [0001] projection image with $\{10\bar{1}0\}$ facets labeled in red and the strain contrast and Fresnel fringes extending out from the void in a hexagonal shape, as well as the central strain contrast from the dislocation.

Figure 6.3(d) shows a void with hexagonal contrast from the Fresnel fringes and an open core dislocation that has formed out of the top peak of the void. The vertical tube voids visible in Figure 6.1(a), (b), and (d) are like the open core dislocation visible in Figure 6.3(d). Figure 6.3(e) is a high magnification Z-contrast STEM image that shows the same open core dislocation as in Figure 6.3(d). The open core dislocations have $\{10\bar{1}0\}$ hexagonal factes and are consistent with previous reports(*173–178*).

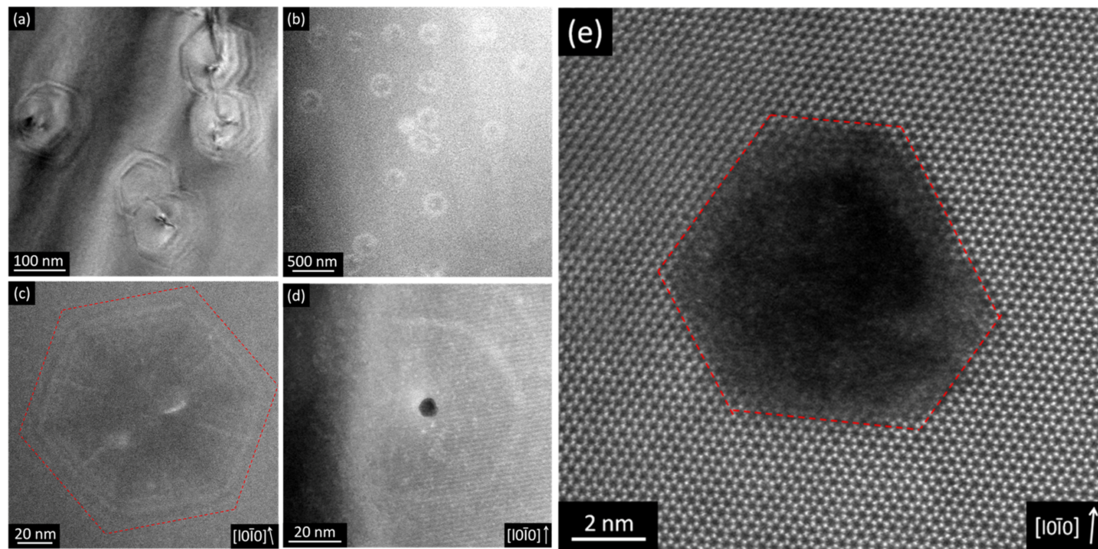

Figure 6.3. [0001] plan-view images. (a) TEM image showing Fresnel contrast from the embedded voids and central dislocation contrast. (b) STEM image showing Fresnel contrast from the embedded voids and central dislocation contrast. (c) and (d) are typical higher magnification STEM images of the embedded voids with the $\{10\bar{1}0\}$ facets shown in red in (c). (e) is a high magnification STEM image of an open core dislocation cap.(*77*)

Because the $\{10\bar{1}0\}$ facets of the open core dislocations are parallel to the facets of the voids hexagonal Fresnel contrast and the side facets of the void are 58° to 62° from the (0001) bottom facet, the voids must have $\{10\bar{1}1\}$ side facets. The Fresnel fringe contrast is always a nearly symmetric equal sided hexagon, while the open core dislocations are not always symmetric, as seen in Figure 6.3(e).

A Burgers vector circuit analysis was conducted on both of the two [0001] projection atomic-resolution images. Figure 6.4 shows the Burgers circuit on a closed dislocation, displaying a $1/3\langle 11\bar{2}0\rangle$ edge dislocation Burgers vector. Similar analysis on an open core dislocation resulted in no edge dislocation Burgers vector. This implies the

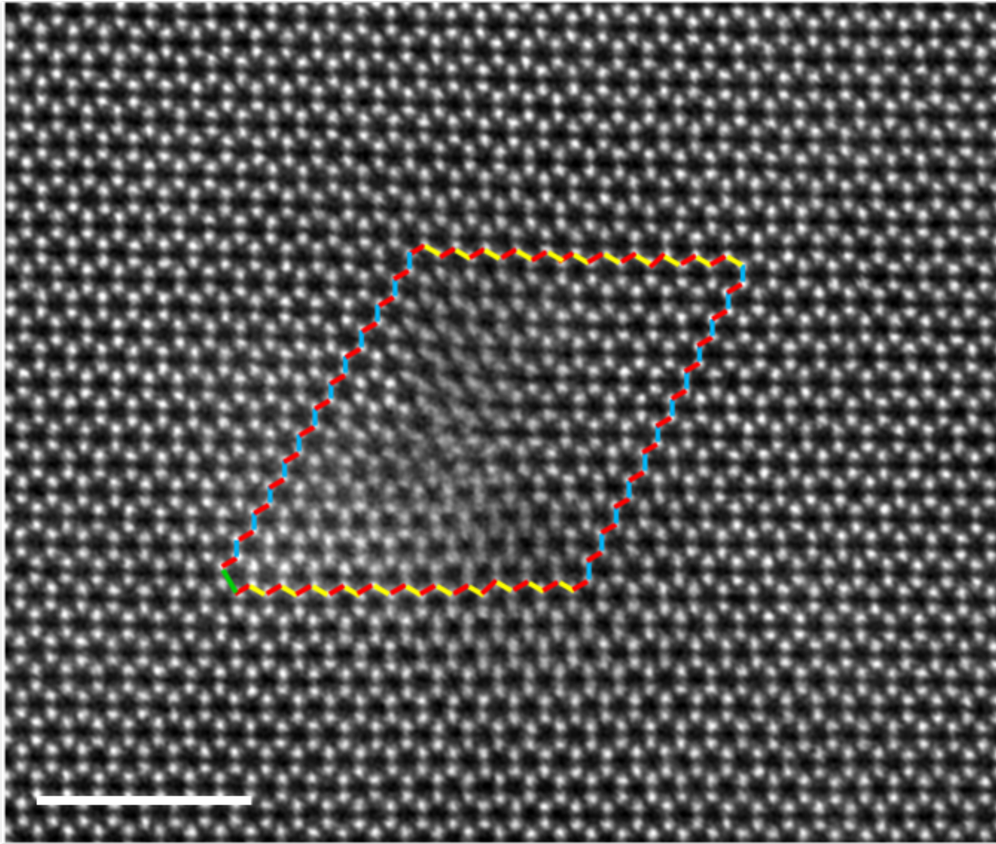

Figure 6.4. STEM image of a closed dislocation at the center of a void defect in a plan-view sample. The displayed Burgers vector circuit shows the dislocation has a 1/3<$11\bar{2}0$> Burgers vector and at least some edge character. Scale bar is 2 nm.

closed dislocations are of either pure edge character or a mix of edge and screw character, and the open core dislocations are purely screw dislocations. Pure edge character of the closed dislocation is consistent with known GaN threading dislocations, and pure screw character of the open core dislocations is consistent with past reports.

Figure 6.5 summarizes the 2 observed structures of the hexagonal-based pyramid voids. They have symmetric hexagonal-shaped (0001) base facets and $\{10\bar{1}1\}$ side facets. Each pyramid void has a dislocation at the peak of the pyramid, which extends up along the [0001] growth direction. The closed dislocations shown in Figure 6.5(a) have a

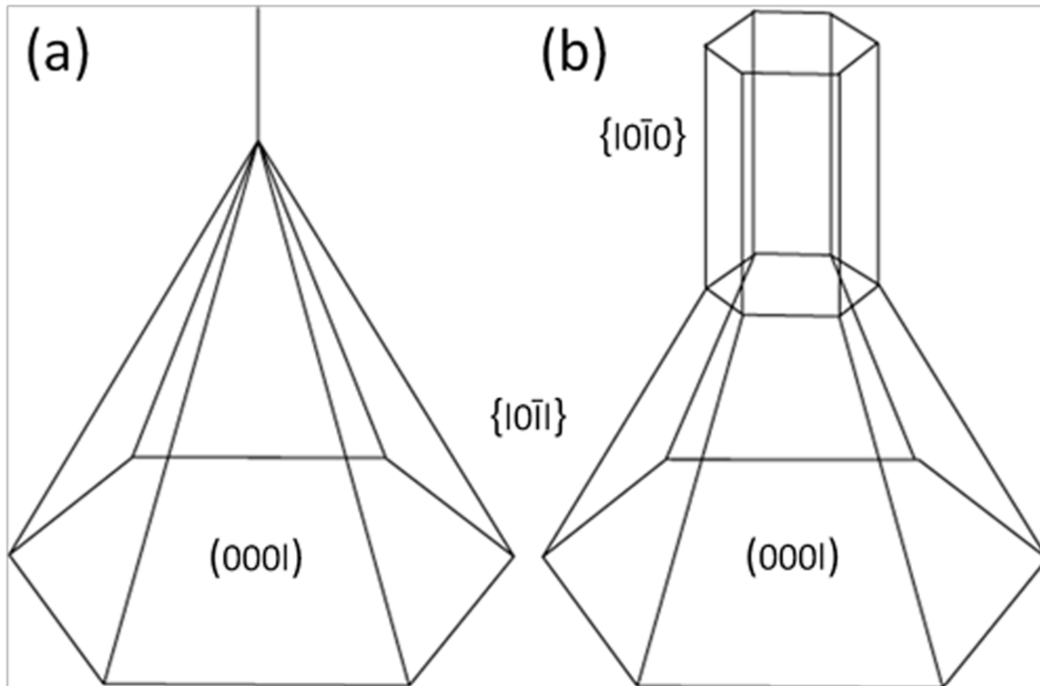

Figure 6.5. Schematic diagrams showing the structure and facets of the hexagonal-based pyramid voids with (a) a dislocation cap and (b) an open core dislocation cap. The dislocation in (a) has some edge character, and the dislocation in (b) has none.(*77*)

1/3<$11\bar{2}0$> Burgers vector component perpendicular to [0001], giving them at least some edge character. As shown in Figure 6.5(b), some of the dislocations are hexagonal open core pure screw dislocations with $\{10\bar{1}0\}$ side facets, varying lateral widths, and varying degrees of hexagonal symmetry.

Figure 6.6 shows data from a STEM EELS SI of a void viewed in cross-section. Figure 6.6(a) is a STEM image of a hexagonal-based pyramid void in the InGaN layers where the SI was taken. Figure 6.6(b) is the STEM image collected simultaneously with the EELS SI. The SI pixel size was 0.664 nm/pixel (which is much larger than the STEM resolution), causing the pixilated look of the simultaneous STEM image. Figures 6.6(c)-

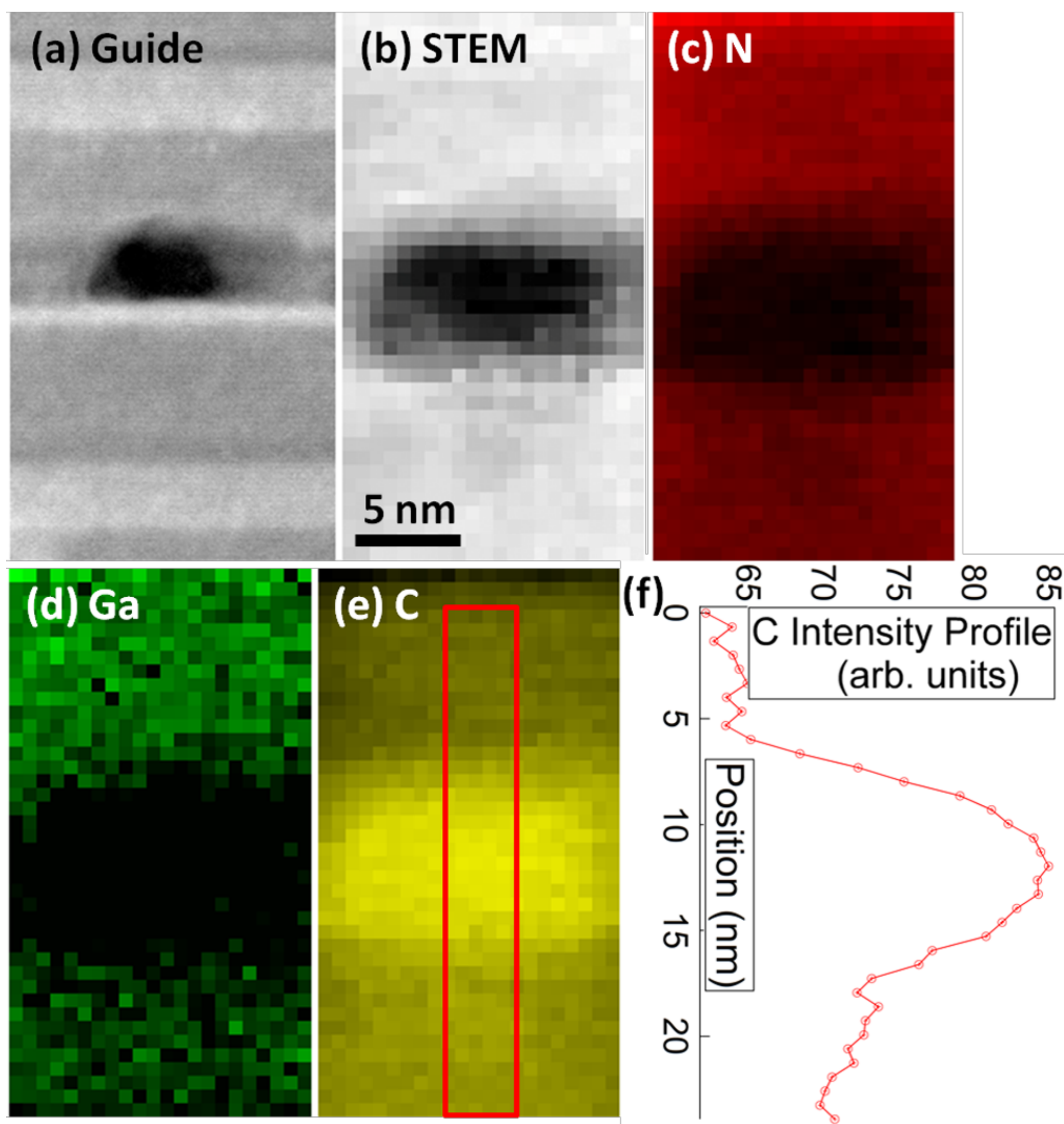

Figure 6.6. STEM EELS spectrum image data of a pyramid void. (a) HAADF STEM image of the sample area where the spectrum image was collected. (b) The simultaneous STEM image taken during the spectrum image. (c) Nitrogen K, (d) gallium L, and (e) carbon K edge EELS intensity maps after background subtraction. (f) Horizontally integrated line profile of the red box in (e) showing the vertical carbon distribution across the void.(*77*)

(e) are background-subtracted nitrogen K, gallium L, and carbon K edge EELS intensity maps, respectively. Figure 6.6(f) is a horizontally integrated line profile of the red box in Figure 6.6(e), showing the vertical carbon distribution across the void. Figure 6.6(e) and (f) indicate that there is a large C concentration inside or on the facets of the pyramid void, and that there is a larger C concentration below the void than above the void. This incorporated C may cause stress that contributes to the formation of the void and the capping dislocation. There is no indication that the sample is thicker under the void than above the void. Because carbon deposition is known to cause growth irregularities during deposition(*191*), we believe carbon contamination during the MOCVD deposition process could act as a growth mask, stopping the GaN deposition locally. When subsequent layers of GaN are deposited around the C contaminated regions, the GaN could then begin to overhang the voided areas along the $\{10\bar{1}1\}$ facets. The dislocation at the pyramids peak could be formed by the imperfect meeting of the six $\{10\bar{1}1\}$ facets.

This void is distinct from the V-defect found in InGaN QWs. The V-defect is not a void enclosed by a top plane, while the void defect reported here is a fully enclosed void with a (0001) bottom facet. The V-defect initiates when a [0001] pointing threading dislocation (created at the sapphire/GaN interface) intersects the InGaN active region layers, while the void reported here does not initiate from a dislocation, but likely from C enriched regions. This void defect creates a [0001] pointing dislocation that is not connected to the sapphire/GaN interface. V-defects are only found in InGaN layers, while the void reported here is found in InGaN and GaN layers. Lastly, V-defects are

point-down pyramids with respect to the Ga-polar growth direction, while the voids reported here are point-up pyramids.

This void is also distinct from the previously reported pyramidal defects found in Mg-doped GaN. Both voids are found in Ga polar GaN, but the Mg-doped GaN defect initiates at the tip of the pyramid and therefore makes a point-down pyramid with respect to the growth direction. The defect reported here initiates with the (0001) facet as a base and therefore produces a point-up pyramid with respect to the growth direction. The Mg-doped GaN defect has only been found in Mg and Be-doped GaN, while the defect reported here is found in GaN and InGaN. The sidewall facets of the Mg-doped GaN defect are $\{11\bar{2}3\}$, while the sidewall facets of the defect reported here are $\{10\bar{1}1\}$. The pyramidal defects found in Mg-doped GaN are not associated with dislocations, while the defect reported here produces a dislocation out the tip of the pyramid along [0001]. Finally, the Mg-doped GaN defect originates because of Mg-rich clusters, while the defect presented here likely originates due to C deposition on the growth surface.

No void defects like those reported here or previously reported in Mg-doped GaN were observed in the top Mg-doped GaN layer of the LED structures investigated here (with Mg concentrations in the range of 5 x 10^{18} to 1 x 10^{19} cm^{-3}). The higher Mg concentrations (6 x 10^{19} to 2 x 10^{20} cm^{-3})(*187*) of the layers in which defects were previously observed could be the reason why no such defects exist in our Mg-doped layers. Because Mg-doping increases the lateral growth rate in GaN(*192*, *193*), the C-disturbed areas in the Mg-doped layer could be more easily covered than undoped GaN.

This could explain why no defect voids of the type reported here were found in the Mg-doped layer.

To enhance light extraction in LED structures, voids with similar shapes but much larger sizes have been created in GaN by utilizing a patterned under layer(*194*). If engineered correctly, the voids reported here could serve a similar purpose. It might be possible to use a block-copolymer or a self-assembled monolayer to create a structured carbon mask without the use of lithography.

6.5. Conclusions

By using conventional TEM and aberration-corrected STEM we discovered a pyramid-shaped void defect in Ga-polar GaN and InGaN that has a hexagonal (0001) base facet and $\{10\bar{1}1\}$ side facets. Each pyramid void creates a dislocation from the top peak of the pyramid, which continues up along the [0001] growth direction to the surface. Some of the dislocation caps form hexagonal open core screw dislocations with $\{10\bar{1}0\}$ side facets. STEM EELS SI reveals a larger C concentration inside the pyramid void and inside GaN below the void compared to above the void. This suggests that the voids could be created during the MOCVD process by inadvertent carbon deposition that acts as a growth mask, stopping the GaN formation locally.

Chapter 7: Non-Rigid Registration and Image Analysis Tools

7.1. Introduction

Image registration techniques are useful in almost all scientific imaging fields, with the intention of increasing some measure of image quality to help detect and measure signals of interest. For TEM and STEM, image registration is routinely used to align tilt-series tomography data of nanostructures, to compute the size and direction of sample drift during EDS and EELS spectrum imaging for inline drift correction, and to align TEM and STEM image series to enable higher signal to noise ratio (SNR) after averaging. The most common image registration technique is rigid registration, which utilizes maximizing the normalized cross-correlation between 2 frames. By giving each image in a series a deformation vector, multiple frames can be aligned using rigid registration to correct for the shift in image area between frames. This works well for TEM images because TEM utilizes a parallel pixel acquisition, meaning all the pixels in a single image are recorded at the same time. In this case, when the sample or electron beam moves during an image series acquisition, there will be a single deformation that can be used on each image pair to register the two consecutive images. Rigid registration is a good way account for sample drift because all the pixels within a single image experience the exact same distortions.

For STEM image series, rigid registration is not optimal because STEM utilizes serial pixel acquisition, meaning each image pixel is recorded at a different time as the STEM probe is raster-scanned across the sample. This causes each pixel in an image to have different spatial distortions created by time varying instabilities. Rigid registration

would correct for the drift between image frames, but not the distortions present within the frames. As discussed further in the next 4 chapters, these distortions within STEM images affect one's ability to locate atom columns, measure atomic structures, quantitatively use the STEM image intensity, and determine the sample chemistry with atomic resolution.

The origins of the distortions present in STEM images are primarily due to instabilities in the electron probe and the sample. The major constituents of the instabilities are constant linear drift from sample holder thermal expansion, low frequency (1 Hz) random walk from floor vibrations, mid-frequency (30-60 Hz) motion from acoustic noise and electromagnetic fields, and high-frequency (400-3000 Hz) noise from electronic instabilities. The presence and magnitude of these instabilities vary from microscope to microscope depending on the lab environment.

Here, a new registration technique, non-rigid registration (NRR), developed for STEM by Benjamin Berkels is introduced and validated for STEM imaging. NRR allows for the correction of all types of distortions present in STEM images by allowing each image pixel a deformation vector. NRR of a simulated STEM image series of a silicon [110] dislocation model validates this technique by showing that NRR preserves non-homogeneous strain fields. Algorithms were written to extract quantitative information, such as atomic column positions and intensities, from STEM images in order to compare the quality of images processed with different techniques and to make measurements on experimental data. Chapter 7.4 summarizes these algorithms.

7.2. Non-Rigid Registration Technique

In order to register two images, *f* and *g*, a deformation ϕ of the image domain much be found such that the composition $f \circ \phi$ agrees with *g*. The conventional approach is using a rigid translation for ϕ(*195–197*), which works well for an unchanging pixel grid image that has no distortions within the image (like in Figure 7.1(a)), but it can lead to a loss of resolution and precision if there are distortions (like in Figure 7.1(b)). The NRR scheme uses a pixel-wise deformation ϕ_{NR}, which accounts for all sources of image distortion from the small probe instabilities to large sample drift.

Because each pixel in each image is allowed a deformation using NRR, estimating ϕ_{NR} is a highly under-constrained problem. Our collaborators (Benjamin Berkels, W. Dahmen, and P. Binev) found a solution to this problem which is summarized here and discussed in greater detail elsewhere(*198*). NRR minimizes E[ϕ_{NR}], which is the sum of the negative normalized cross correlation, E_{NCC}, of $f \circ \phi_{NR}$ and *g*, and the Dirichlet energy of the displacement, which is a regularizer on ϕ_{NR}(*199*):

$$E[\phi_{NR}] = E_{NCC}[\phi_{NR}] + \frac{\lambda}{2}\int_{\Omega} \left\| D\phi_{NR}(x) - \mathbf{1} \right\|^{2} dx \,, \tag{1}$$

where Ω is the image domain. The first term represents the similarity measure defined as

$$E_{NCC}[\phi] = -NCC[f \circ \phi, g]\,, \tag{2}$$

for two functions *f*, and *g* that are considered to be a function from the image domain **Ω.** NCC is the normalized cross correlation function defined by:

$$NCC[f,g] = \frac{1}{|\Omega|}\int_{\Omega} \frac{\left(f - \bar{f}\right)}{\sigma_f}\frac{\left(g - \bar{g}\right)}{\sigma_g} dx \,, \tag{3}$$

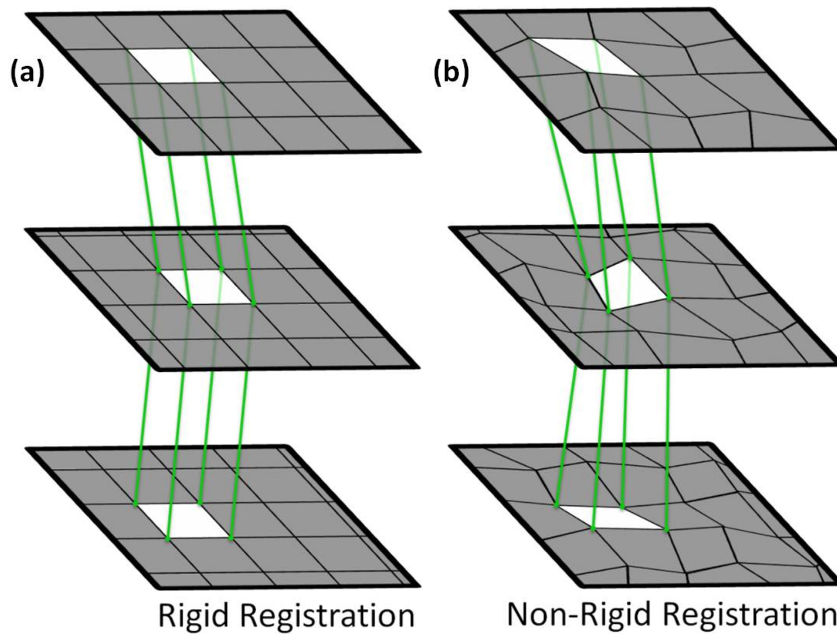

Figure 7.1: Diagrams showing (a) rigid and (b) non-rigid registration of an image series without and with image pixel distortions, respectively.(*241*)

The NRR deformation model uses a separate displacement vector for each pixel, which may move independently from the other pixels. To help solve this, a smoothness constraint is introduced on the deformation by penalizing irregular deformations using an additional regularization term, the second term in equation 1. Here, $D\phi(x)$ denotes the Jacobian of ϕ, **1** is the identity matrix, and $||A||$ denotes the Frobenius norm of A. λ is a nonnegative, constant parameter that controls the smoothness of the minimizing deformation. The use of this regularization term in the context of image registration is commonly called diffusion registration(*200*), and it acts to penalize pixel deformations that are dissimilar from the deformations of neighboring pixels.

Due to the periodic structure of the images, there will be several local minima of E despite the regularization term. To avoid the unwanted minima in the minimization,

they employ a coarse-to-fine multilevel scheme simultaneously with the other approaches, following the ideas of multi-grid algorithms(*201*, *202*). In this particular implementation, they use 2^d x 2^d grids for increasing integer values of d, starting with a scale coarse enough to capture the translational component of the distortion due to sample drift while maintaining atomic resolution. NRR initially registers down-sampled variants of the images, then uses the resulting ϕ_{NR} as an initial guess at the next finer sampling levels, iterating up to the original sampling. At each level the minimization problem is solved. The aim of this process is to aid the registration to the proper local minimum by avoiding small periodic structures at the beginning.

To register the entire sequence of images $f_0, \ldots, f_N$, first NR deformations $f_{j+1,j}$ between all pairs f_j and f_{j+1} are found. Then the entire series is registered to the first frame (f_0) using $\phi_{j+1,j} \circ \phi_{j,0}$ as the initial guess for $f_{j+1,0}$. Once all frames have been registered to the first frame, the series is averaged. Then the registration is repeated using the average of the registered frames $\bar{f}$ as the reference frame, and then iterated to find the final ϕ_{NR}. Bilinear interpolation is used to accommodate sub-pixel displacements, producing a small smoothing effect on the final image. Since the reference frame $\bar{f}$ computed by the first pass of the algorithm is significantly less noisy than the input frames, the regularization parameter λ can be reduced after the first pass. Specifically, 0.1λ is taken as the regularization parameter after the first pass.

The NRR technique makes some assumptions about the STEM imaging process. It implicitly assumes that: 1) sample drift is relatively small, less than any of the crystal repeat distances in the images, from frame to frame, 2) instabilities that are fast compared

to the frame time have zero mean over many frames, and 3) there is an inverse relationship between the amplitude of a distortion and its smoothness, so large displacements must affect many pixels, while small displacements affect only a few pixels. Unlike some previous efforts(*203–206*), we do not make any assumptions about the sample or its structure, such as periodicity or repetition of image features, nor do we make any assumptions about the nature of the image Fourier transform. In principle, any technique subject to pixel distortions can benefit from NRR, including cryo-TEM(*207*) and atomic force, scanning tunneling, or scanning electron microscopy.

7.3. Validation of Non-Rigid Registration on Simulated STEM Data

The NRR approach was validated using simulated STEM data of a Si dislocation core by showing it preserves inhomogeneous strain fields with pm-precision. Ao Li and Izabela Szlufarska calculated the atomic-structure of a Si [110] edge dislocation using molecular dynamics (MD) simulations implemented in the Large Scale Molecular Dynamics Simulator (LAMMPS) software using the Tersoff potential(*208*). The cohesive energy of a Si single crystal was calculated to be 4.61 eV, in a good agreement with published experimental values (4.55–4.90 eV)(*209*). Dislocations were modeled in a 66,420-atom cell with dimensions 16.1 nm x 21.7 nm x 3.8 nm along the x = [110], y = $[00\bar{1}]$ and z = $[\bar{1}10]$ directions, respectively. Two perfect edge dislocations of the opposite sign and with dislocation lines parallel to the z-axis were introduced in the model. Periodic boundary conditions were applied in all three spatial directions. The cell was large enough so that the overlap of strain fields from periodic images of dislocations

was negligible. The system was relaxed at zero pressure and 5 K in a constant pressure-constant temperature ensemble using a Nose Hoover thermostat and barostat. The resulting structure of the dislocation is in good agreement with previously published structures generated using MD(*210*).

The frozen-phonon multislice method was used to calculate a distortion-free STEM image of the Si [110] dislocation core, shown in Figure 7.2(a). A synthetic series of 512 distorted STEM images of the Si [110] dislocation core was calculated by resampling the distortion-free simulated image. The simulated distorted image series includes instabilities that match the frequencies of measured instabilities of the UW-Madison FEI Titan STEM, consisting of constant linear drift from thermal expansion, low-frequency (~1 Hz) random walk from floor vibrations, mid-frequency (30-60 Hz) motion from acoustic noise and electromagnetic fields, and high-frequency (400-3000 Hz) noise from electronic instabilities. The simulated series intensity was also scaled to match the incident intensity typical in STEM image series (like that shown in Figure 8.1), and appropriate Poisson noise was added in each pixel of each frame. Figure 7.2(b) shows one frame from the simulated noisy and distorted STEM image series of the Si dislocation core.

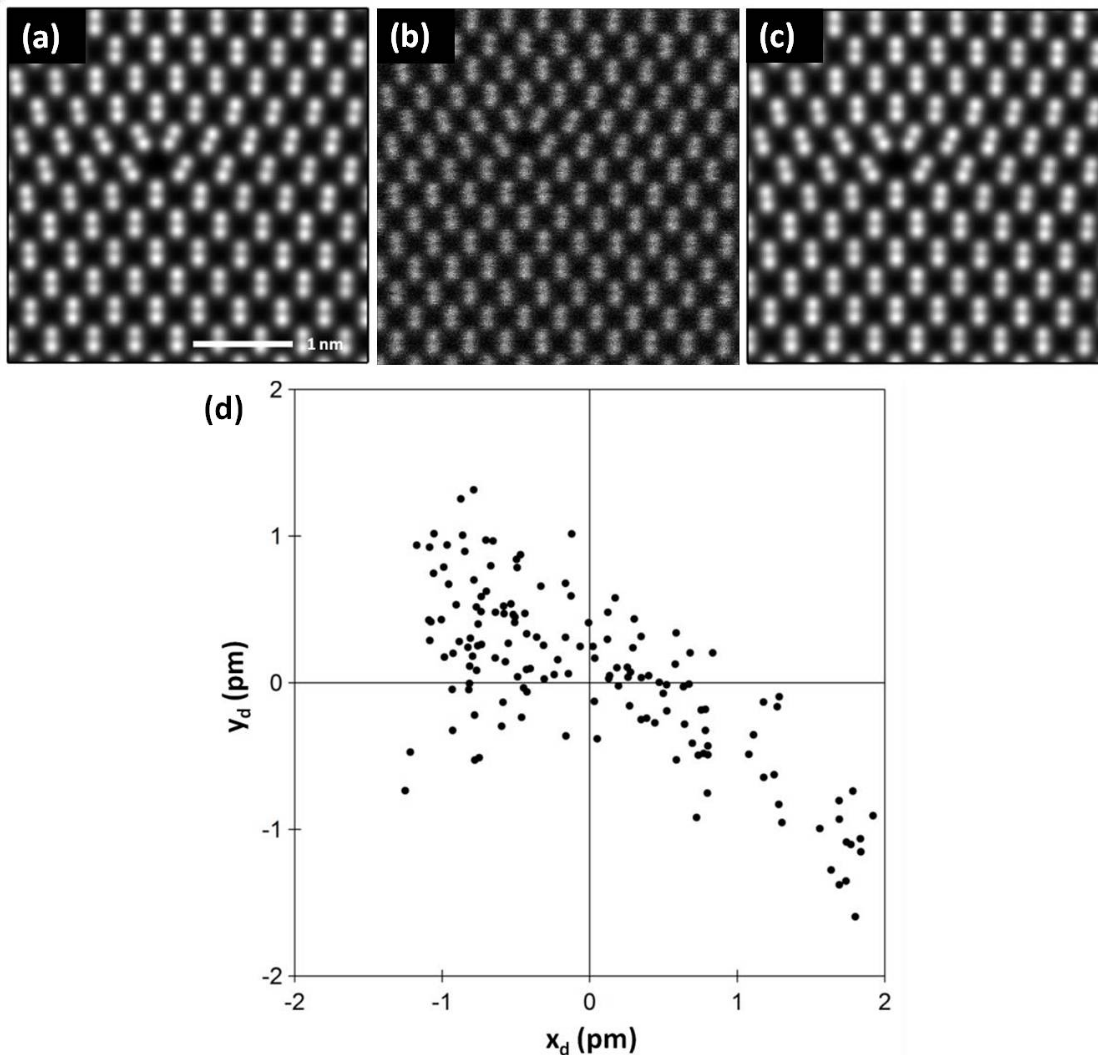

Figure 7.2: (a) Multislice simulated HAADF STEM image of a Si [110] dislocation core model. The model was determined using MD calculations. (b) One frame from the simulated noisy and distorted STEM image series created from (a). (c) The NRR and averaged HAADF STEM image of the distorted image series. (d) Displacement of every atom column between (a) and (b).(*241*)

NRR and averaging was employed on the simulated distorted STEM image series of the Si dislocation. Because of sample drift during the series acquisition, only part of the NRR and averaged image uses all the frames for the average and has the best SNR

ratio. Figure 7.2(c) shows the average image after NRR of only the area that used all 512 images in the average. Because of sample drift during the series acquisition, only part of the NRR and averaged image uses all the frames for the average and has the best SNR ratio. The atomic column positions in both the undistorted original simulated STEM image and the NRR and averaged STEM image were found using Gaussian fitting, using the methods discussed in the Chapter 7.4. Figure 7.2(d) shows the vector displacements (x_d, y_d) of every atomic column between the NR registered and averaged image and the undistorted image. Most of the displacements are smaller than 1 pm, including the atomic columns under the strongest influence of the inhomogeneous strain field surrounding the dislocation core. The root mean square of all the displacements is 0.85 pm in the x direction and 0.58 pm in the y direction. NRR preserves the positions of atomic columns in inhomogeneously strained structures and does not introduce any image artifacts that affect the locations of the atomic columns on a scale larger than one pm.

7.4. Image Analysis Tools Development

Atomic-resolution STEM images are information-rich and hold much more data than what is qualitatively interpreted by simply looking at the images. This information includes, but is not limited to, precise atomic positions of the imaged structure and sample thickness of each atomic column. To extract this information, methods of analyzing the image pixel intensities need to be used. Algorithms were developed in the IGOR Pro software package to process images in an unbiased, reproducible, and fast

approach to gain this information.

To achieve sub-pixel accuracy in locating the atomic column positions, we fit a small region of pixels around each atomic column to a 2D Gaussian function plus a constant,

$$I(x,y) = I_0 + A\exp\left[\left(\frac{-1}{2(1-c^2)}\right)\left(\left(\frac{x-x_0}{x_w}\right)^2 + \left(\frac{y-y_0}{y_w}\right)^2 - \left(\frac{2c(x-x_0)(y-y_0)}{x_w y_w}\right)\right)\right] \quad \text{(Eq. 1)}$$

using the standard Levenberg-Marquart L^2 norm minimization method. The fit parameters are I_0, A, x_w y_w, x_0, y_0, and c, while x and y are the position for the intensity I. If the image is put on the number of detected electrons intensity scale, the Gaussian fits can be weighted by the Poisson noise (square root of the total number of electrons, $\sqrt{n}$) in order to estimate the uncertainties in the fit parameters. Algorithms were written to automatically find atom columns (using particle analysis tools), fit the identified atom columns to find their location, and then analyze their positions in various ways depending on what information is desired. Once atom columns are automatically located, their intensities can also be analyzed in a number of ways to extract 3D information. Multiple algorithms were written to compare experimental and simulated data (both STEM images and PACBED patterns) in order to extract thickness measurements.

These algorithms are left with the Voyles group and hosted on github (https://github.com/paul-voyles/Igor/tree/ayankovich). Appendix 2 has basic instructions on how to use the IGOR functions. More detailed instructions can be found in the header of the IGOR procedures.

Chapter 8: High Precision Imaging of Single Crystal Materials

8.1. Introduction

For TEM and STEM, once the resolution is good enough to achieve atomic resolution, the question becomes how precisely can we measure atom positions(*211*)? Precision smaller than the resolution is routinely achievable(*142*, *195–197*, *212–215*). When we started this project, the best reported precision for STEM was 4-5 pm(*196*, *197*), but contemporaneous developments can now achieve 2 pm(*216*). The best reported precision for TEM is 1-3 pm(*212*, *214*). Spatial precision is fundamentally limited by the signal-to-noise ratio (SNR) of the image, so TEM and STEM usually combine multiple exposures to increase the SNR and achieve the optimal precision(*195*, *196*, *212–215*). However, STEM encounters practical limits that are introduced by the serial acquisition of image pixels before reaching the fundamental SNR limit. As discussed in Chapter 7.1, serial acquisition translates instabilities in the position of the probe and the sample into displacements of the imaged atoms, instead of reduced contrast as in the parallel acquisition of conventional TEM. In STEM, instabilities that are fast compared to the frame time and have zero mean can be removed by averaging over many frames, but the frames must first be registered to one another. Rigid registration is the conventional approach to account for drift of the sample between frames(*196*, *197*). Rigid registration works well for the perfect, unchanging pixel grid inherent in TEM images, but it can lead to the loss of both resolution and precision if there are distortions in the pixel positions that vary from image to image, which are inherent in STEM images. Because these small-scale instabilities are essentially impossible to completely eliminate during

experiments, developing a new registration technique to account for these instabilities is a more realistic approach to better STEM precision.

Here, we report that NRR allows sub-pm precision in atomic resolution STEM images of single crystal materials, the best reported in electron microscopy. The experimental protocol to achieve these results is described in detail in Appendix 2. We also conducted a simulation study looking into the question: what are the ultimate precision limits in STEM images? This question becomes relevant because of the high precision enabled by NRR and averaging. We find that the precision limits from dynamical scattering and electron channeling in HAADF images are similar to the experimentally observed HAADF STEM precision (~1 pm). However, the precision limits for ABF STEM are larger (10-20 pm) and should be experimentally noticeable. The precision limits are dependent on the material, zone axis, and imaging conditions, highlighting the necessity of combining STEM image simulations with experiments to interpret high precision STEM images.

8.2. Material Synthesis

STEM experiments were performed on the GaN template layers from the samples studied in Chapter 5. The GaN material synthesis and TEM sample preparation techniques are discussed in depth in Chapter 5. The Si TEM sample was made from a commercially purchased bulk Si wafer using the wedge polishing technique so that the [110] zone axis was normal to the TEM sample surface. Final thinning was conducted in a Fischione 1010 ion mill, and before STEM experiments, samples were plasma-cleaned

in a Fischione plasma cleaner in a 75% argon–25% oxygen mixture for 5 min to eliminate organic carbon surface contamination.

8.3. Sub-pm Precision Imaging of Single Crystal GaN and Si

Figure 8.1 and 8.3 show that NRR of aberration-corrected STEM images can achieve sub-pm precision. A series of 512 HAADF STEM images of Si [110] was acquired with 256 by 256 pixels, a 13 μs/pixel dwell time, and 15.25 pm/pixel sampling. Figure 8.1(a) shows the first image of the series. The series was aligned using the NRR technique, averaged, and put on an absolute intensity scale creating the final HAADF image shown in Figure 8.1(b) with a total dose of 82,850 C/cm^2 and a total dwell time of 6.656 msec/pixel. To achieve sub-pixel accuracy of the Si column positions, each Si dumbbell was fit to the sum of two, two-dimensional Gaussian functions marked by the red dots in Figure 8.1(b) using the algorithms discussed in Chapter 7.4. One Si dumbbell has an integrated intensity of $n = 1.9 \times 10^7$ e^-. Figure 8.1(c) shows a typical fit residual from the dumbbell in the red box in Figure 8.1(b), displaying no features indicative of a poor fit. Figure 8.1(d) and (e) show histograms of the 98 and 58 measured *x* and *y* Si column separations respectively, defined in Figure 8.1(b). Following Bals *et al.*, the precision σ of the image, the standard deviation of these measured values(*195*), is σ_x = 0.86 pm and σ_y = 0.72 pm. σ is a good measure of the precision because the histograms are normally distributed with $\chi^2 = 7.30$ for x and $\chi^2 = 11.46$ for y, both smaller than the 0.05 significance critical value. By another measure of image precision, the uncertainty in the atom column's fit position(*217*), σ_x = 0.36 pm and σ_y = 0.60 pm, again sub-pm.

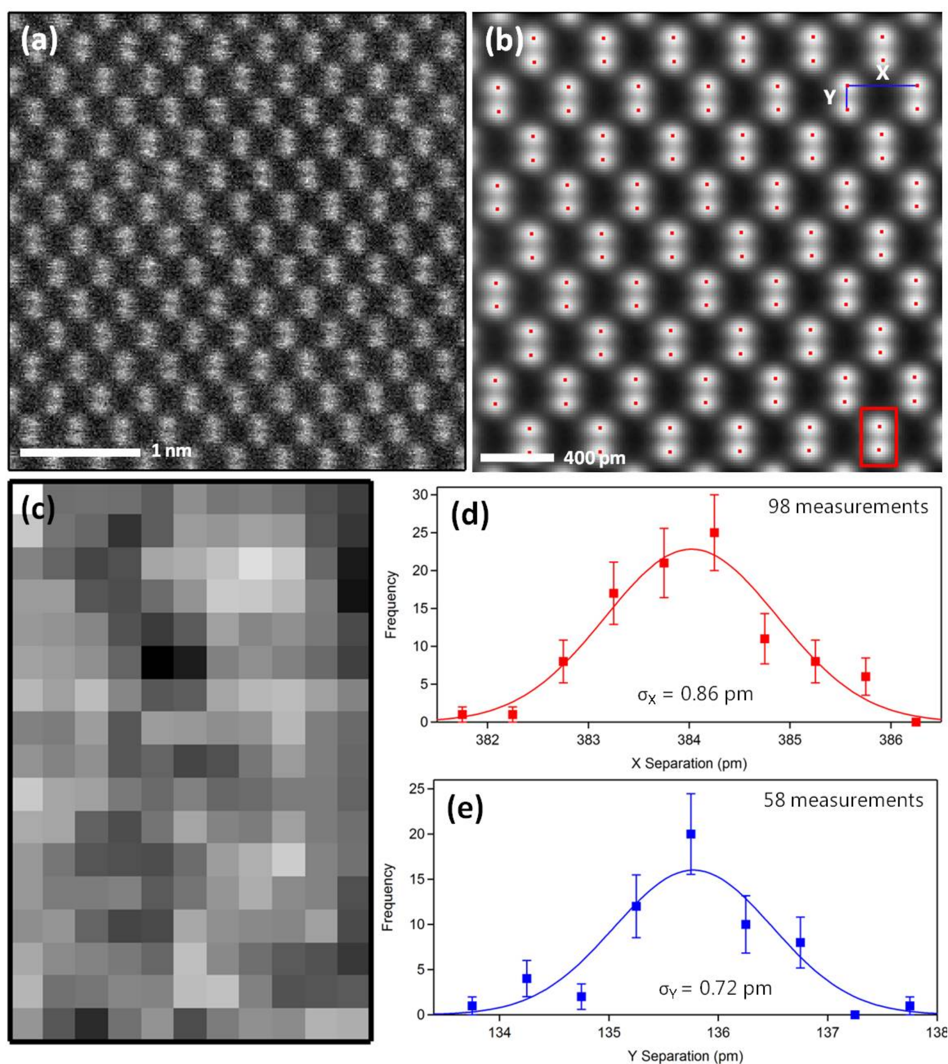

Figure 8.1: shows the use of NRR to achieve sub-pm precision on single crystal Si. (a) The first raw HAADF STEM image of the Si [110] series. (b) The average image after the NRR. The red markers indicate the atomic column positions determined from fitting. (c) The residual of a two 2D Gaussian fit to the Si dumbbell in the red box in (b). The maximum intensity in the residual is 0.5 % of the column peak intensity. (d) and (e) Histograms of the measured separations between the atomic column positions in the *x* and *y* directions defined by the blue axes in (b). The error bars in (d) and (e) are the square root of the frequency and the curves are the best-fit normal distributions.(*241*)

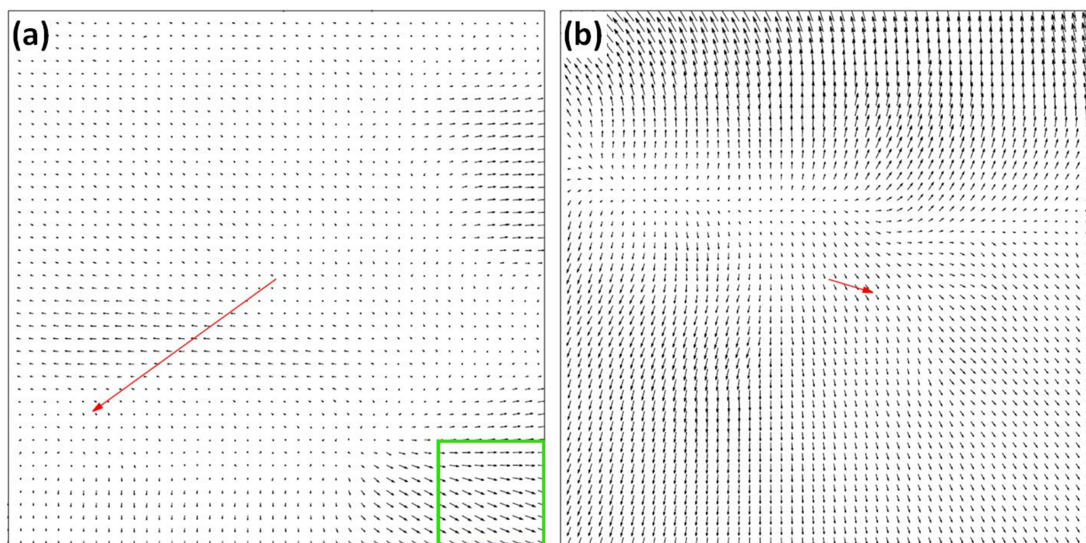

Figure 8.2: Vector plots of the NR pixel deformations of the 200th image in the 512 experimental Si image series shown in Figure 8.1. (**a**) the full image field at reduced pixel density and (**b**), full pixel density for the smaller field shown by the green box in (**a**). The red arrows are the average deformation over the field, which has been subtracted to give the black arrows. The length of all the vectors has been increased to improve visibility.(*241*)

Figure 8.2 shows vector plots of the pixel deformations present in the 200th image of the 512 experimental image series of Si presented in Figure 8.1 measured by the NRR algorithm. Figure 8.2(a) is the full image field at reduced pixel density after the average distortion (the red vector) has been subtracted. Figure 8.2(b) is a magnified image field of the lower right corner of Figure 8.2(a) outlined in green at full pixel density, again after the average distortion (the red vector) has been subtracted. The length of the vectors has been magnified to increase their visibility. The physical magnitude of the average deformation vector shown in red in Figure 8.2(a) is 325.75 pm or 21.50 pixels and in Figure 8.2(b) is 13.11 pm or 0.88 pixels. Figure 8.2 shows the multi-scale nature of the

NRR where at both length scales, there are domains of similar vector size and direction, but as the length scale decreases, so does the magnitude of the variability in the deformations.

Figure 8.3 shows that NRR of HAADF images of GaN along $[11\bar{2}0]$ also results in sub-pm precision. A series of 512 HAADF STEM images were acquired with 256 by 256 pixels, a 13 µs/pixel dwell time, and 10.64 pm/pixel sampling. Figure 8.3(a) shows the first image of the series. The series was aligned using the NRR technique, averaged, and put on an absolute intensity scale, creating a final HAADF image shown in Figure 8.3(b) with a total dose of 162,300 C/cm^2 and a total dwell time of 6.656 msec/pixel. Because of sample drift, the average image was cropped to consist of 56 Ga columns. Each Ga column was fit to a 2D Gaussian to achieve sub-pixel accuracy in the Ga column positions, indicated by the red markers in Figure 8.3(b). One Ga column has an integrated intensity of 1.7 x 10^7 e$^-$. Figure 8.3(c) shows a representative fit residual from the Ga column in the red box in Figure 8.3(b) and displays no features that are indicative of a poor fit. Figure 8.3(d) and (e) show normally distributed histograms of the measured x and y Ga column separations respectively, defined by the blue axes in Figure 8.3(b). The image precision defined as the standard deviation of measured separations is σ_x = 0.74 pm and σ_y = 0.85 pm, while the image precision defined as the average fit position uncertainty is σ_x = 0.16 pm and σ_y = 0.13 pm. Both measures result in sub-pm precision. Other HAADF image series of GaN and Si with different pixel sizes and pixel dwell times achieve similar sub-pm precision.

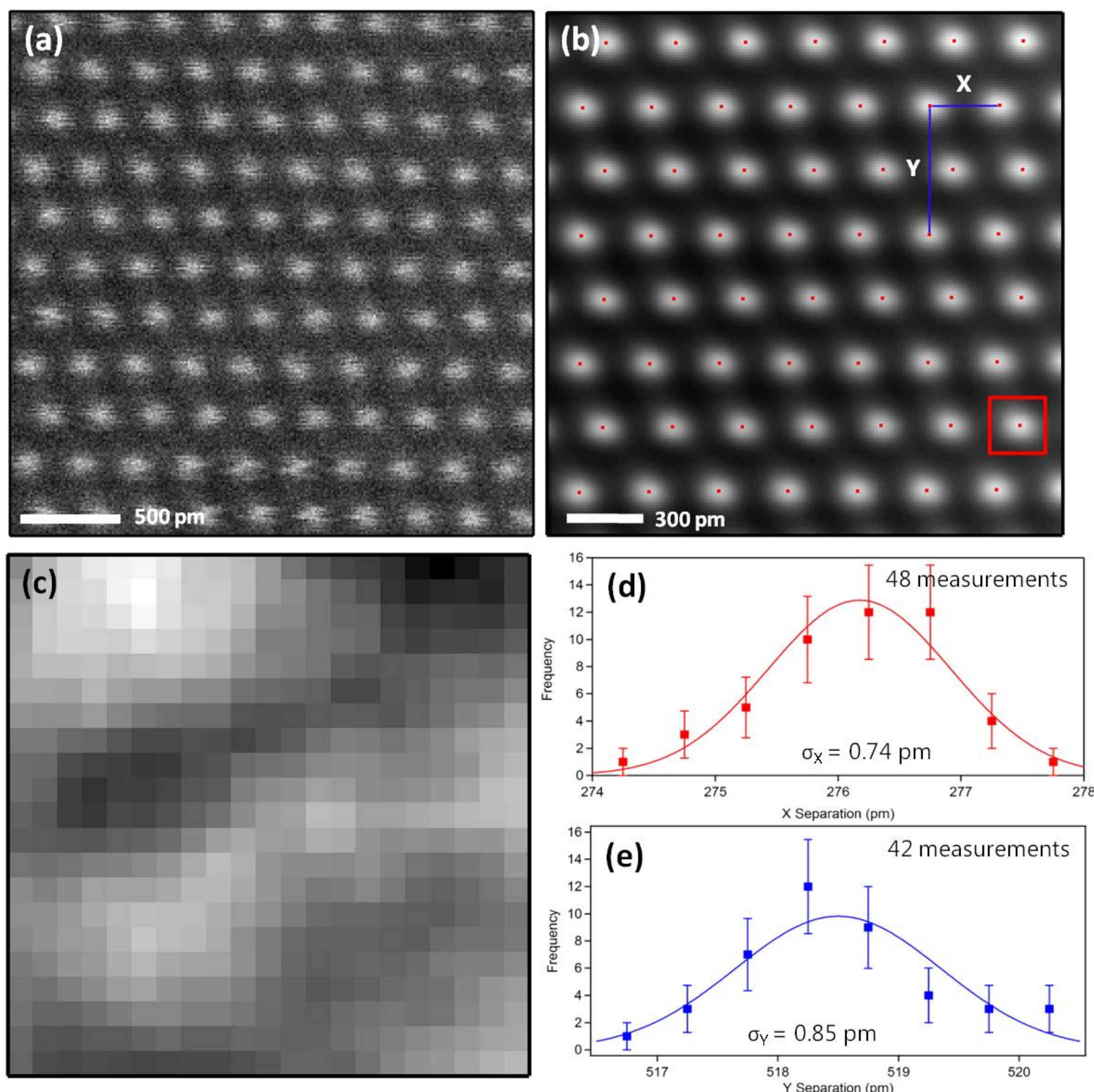

Figure 8.3: shows the use of NRR to achieve sub-pm precision on single crystal GaN. (a) the first raw HAADF STEM image of the GaN [11$\bar{2}$0] series. (b) the average image after the NRR of the 512 HAADF STEM GaN [11$\bar{2}$0] image series. The red markers indicate the atomic column positions determined from fitting. (c) the fit residual of a 2D Gaussian fit function in the red box in (b). (d) and (e) histograms of the measured separations between the atomic column positions indicated by the red markers in (b) in the *x* and *y* directions respectively, defined by the blue axis in (b). The error bars in (d) and (e) are the square root of the frequency and the curves are the best-fit normal distributions.(*241*)

The standard deviation of the series of intensities after NRR for a pixel inside a Si [110] column is 3.6 e-, while $\sqrt{n}$ = 10.6 e^- for the same pixel. Therefore, using $\sqrt{n}$ to weight the fits is a conservative estimate of the noise and yields a conservative estimate of the fit parameter uncertainties. The reduced noise from Poisson noise is most likely a result of the bilinear interpolation step of the NRR. Once atom column locations were found and the separations between the columns in the x and y directions were calculated, the average x and y separations were independently used to calibrate each image's spatial pixel size to the known atomic structure, which corrects for the ~1% pixel non-squareness typical in the STEM scan.

Figure 8.4 shows that NRR achieves better precision than rigid registration of the same Si data set shown in Figure 8.1. Rigid registration was performed with translations determined by fitting the cross-correlation to a Gaussian peak and implemented with sub-pixel shifts using bilinear interpolation. Figure 8.4(a) shows the average image after the rigid registration. The red markers indicate the atom column locations determined from Gaussian fitting. The square markers in Figure 8.4(b) and (c) show the separation histograms of the rigidly registered series in the x and y directions respectively. The lines in Figure 8.4(b) and (c) are the histograms of the NRR series in the x and y directions respectively from Figure 8.1(d) and (e). The rigid registration histograms are significantly wider, reflected in the image precision of σ_x = 5.3 pm and σ_y = 4.0 pm, 5-7 times worse than that achieved with NRR. The rigidly registered histograms are not normally distributed and have a large skew towards larger separations, indicating that some columns are substantially displaced from their correct positions and that σ is

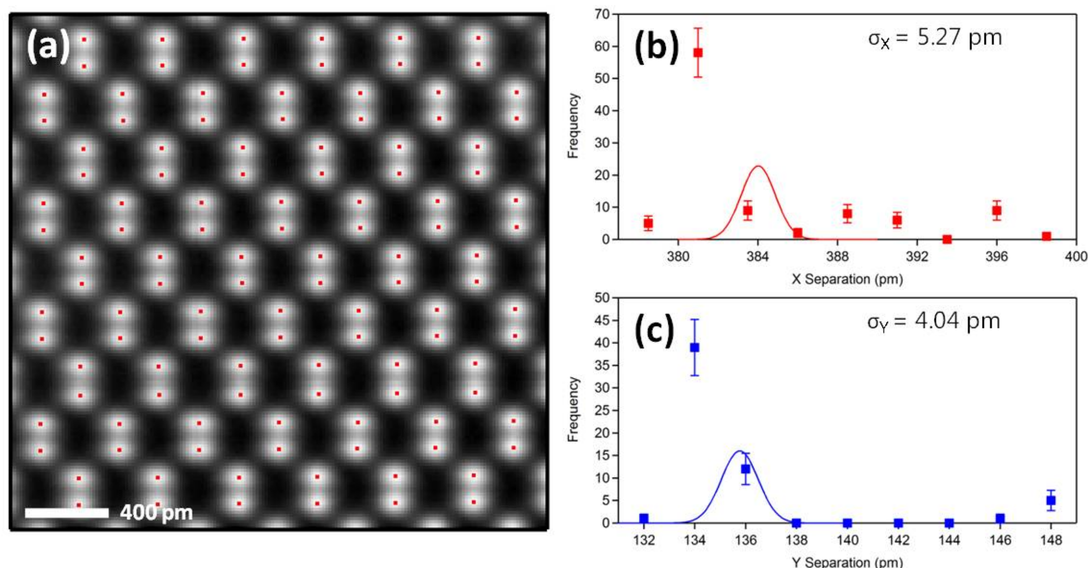

Figure 8.4: (a) the average image after the rigid registration of the HAADF STEM Si [110] image series. The red markers indicate the atomic column positions determined from fitting. The square markers in (b) and (c) show histograms of the measured separations between the atomic column positions indicated by the red markers in (b) in the *x* and *y* directions respectively. The error bars in (b) and (c) are the square root of the frequency. The curves in (b) and (c) show the histograms from the NR registration in the *x* and *y* directions respectively, displaying a much narrower distribution and smaller precision.(*241*)

probably not a good measure of the precision. We suspect that these distortions in the rigid registered image arise because rigid registration does not account for all types of image distortions caused by microscope instabilities.

Figure 8.5 shows the progression of precision, atom column width, and image contrast through the Si and GaN image series as a function of dose. Figure 8.5(a) and (b) show the precision calculated from the cumulative average up to the indicated frame # for Si and GaN. There is an initial steep decrease in precision, but there is no further improvement from including more than ~200 images in the average. This data is useful

for managing the trade-off between precision and damage in beam sensitive materials by limiting the number of frames included in the average. Figure 8.5(c) and (d) show the average *x* and *y* Gaussian fit widths calculated from the cumulative average up to the indicated frame # for Si and GaN. The widths increase by only a few pm by adding more frames to the average, increasing the atom column widths by only 2-4%. Because the Gaussian width is proportional to the image resolution, NRR causes no significant loss in resolution. Figure 8.5(e) and (f) show the image contrast, defined by the ratio of the Gaussian maximum to the constant background (A/I_0 in Equation 1), as a function of frame number through the series (not a cumulative average) using a 10 neighboring frame average in a floating window. Figure 8.5(f) shows a steady decrease of contrast as a function of frame past frame # 140. Because contrast is a good measure of how much focus drift is occurring through the image series, we believe this drop in contrast is probably due to focus drift from motion of the sample along the microscope optical axis. However, this could also be caused by sample damage, contamination accumulation, or aberration drift, although these seem less probable.

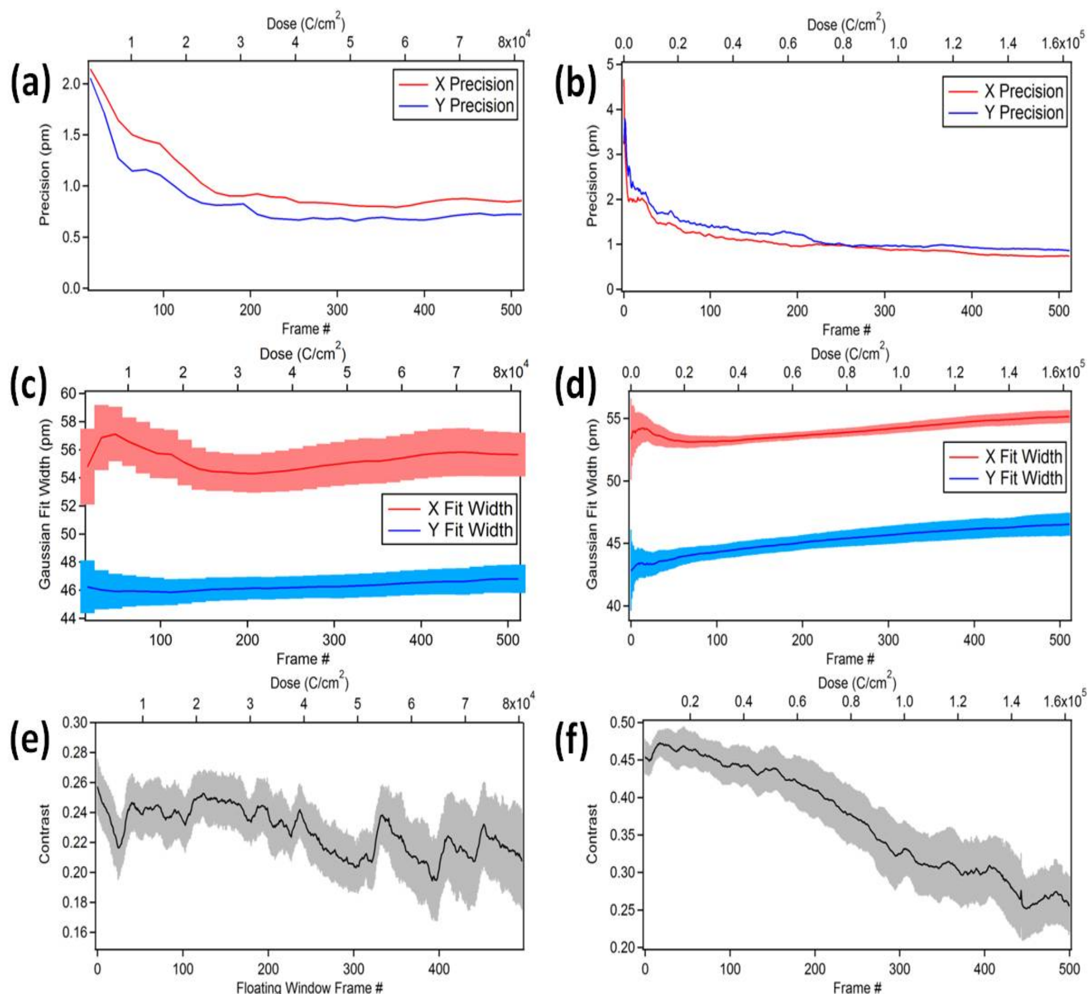

Figure 8.5: (a), (c), and (e) data from the NRR Si [110] image series. (b), (d), and (f) data from the NRR GaN [$11\bar{2}0$] image series. (a) and (b) plots of image precision vs. number of images in the average and total dose to the sample. (c) and (d) plots of the average Gaussian fit width in the *x* and *y* direction vs. number of images in the average and total dose to the sample. (e) and (f) plots of the average atom contrast in a floating window average of 10 images vs. image number and total dose to the sample. The error bands in (c) and (d), and (e) and (f) signify the standard deviation in the atom column widths and atom contrast respectively.(*241*)

8.4. Dynamic Scattering Limits to Precision in HAADF and ABF STEM Images

Surpassing the SNR precision limit using the non-rigid registration technique on STEM images and pushing the precision down to the sub-pm scale leads to a new question: what are the ultimate precision limits? If the SNR and the object (sample) are perfect, what scattering physics is limiting the image precision? Past studies(*218*, *219*) suggest that the supposed structure in some zone axis STEM images do not completely reflect the structure present in the sample, calling into question the robustness and interpretability of STEM images over various sample thicknesses. We have used frozen phonon multislice simulations to explore the precision limits in ABF and HAADF STEM images introduced by the electron beam channeling and dynamical scattering within Si and GaN single crystals.

The characteristics of the aberration corrected Titan at the University of Wisconsin – Madison were used for the frozen phonon multislice simulations in this study. Image simulations assumed a 200 keV electron beam, 24.5 mrad convergence angle, 24.5 pA probe current, and STEM spatial resolution of ~0.8 Å. The HAADF and ABF STEM detector collection angles were 54 to 270 mrad and 11 to 24.1 mrad, respectively. In real experiments, the defocus is usually determined by maximizing the contrast in both ABF and HAADF images. In order to ensure the simulation defocus parameter reflected the same criterion as in real experiments, thickness vs. defocus maps were calculated for Si (110) for both HAADF and ABF images, as shown in Figure 8.6(a) and (b), respectively. A defocus of 0 nm produced the highest contrast in both the

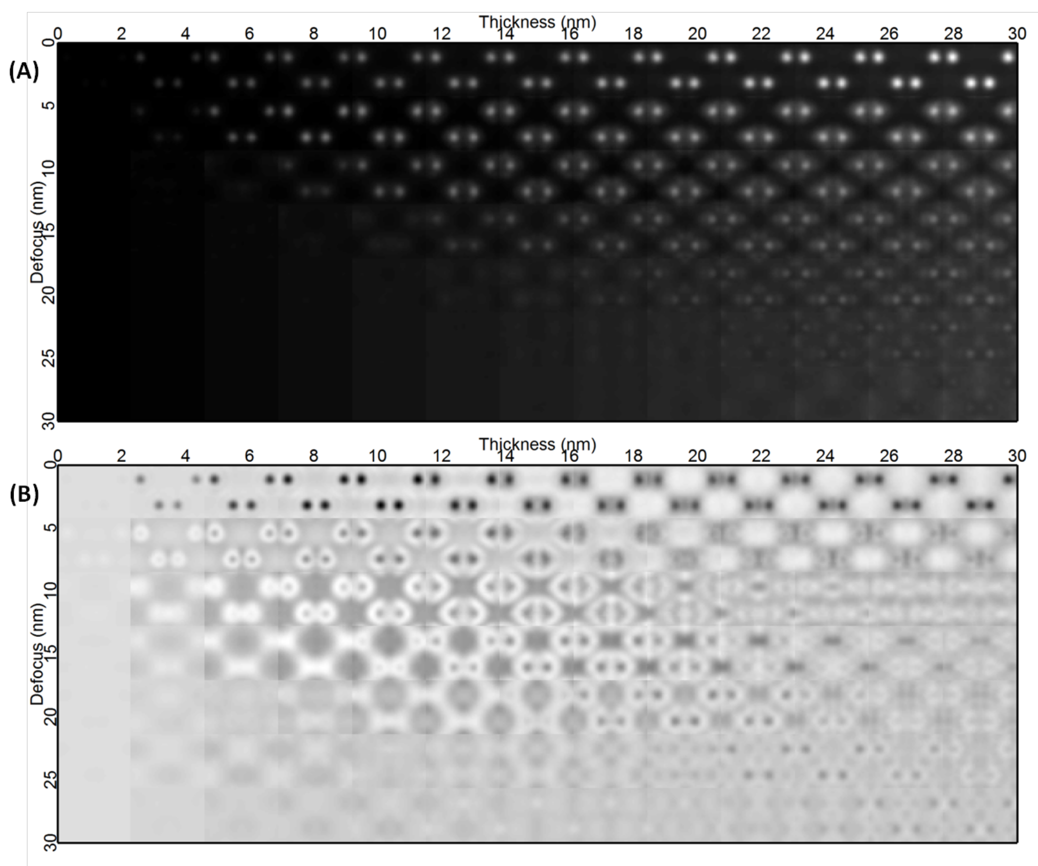

Figure 8.6: Simulated (a) HAADF and (b) ABF STEM thickness defocus map of Si [110] for a thickness and defocus range of 30 nm.

HAADF and ABF images at all thicknesses explored, and therefore 0 nm defocus was used for all further simulations.

Images of a Si [110] dumbbell with thicknesses between 0 and 100 nm were calculated using 16 phonon configurations and a Debeye Waller factor for Si of 0.456 Å^2 (*220*, *221*). The Si [110] crystal was 33.6 Å x 30.7 Å, and was sampled with a 2048 x 2048 pixel wave function. Images of GaN along $[11\bar{2}0]$ with thicknesses between 0 and 100 nm were calculated using 16 phonon configurations and a Debeye Waller factor for Ga of 0.28 Å^2 and N of 0.38 Å^2, taken from Xiong and Moss(*171*). The GaN crystal was

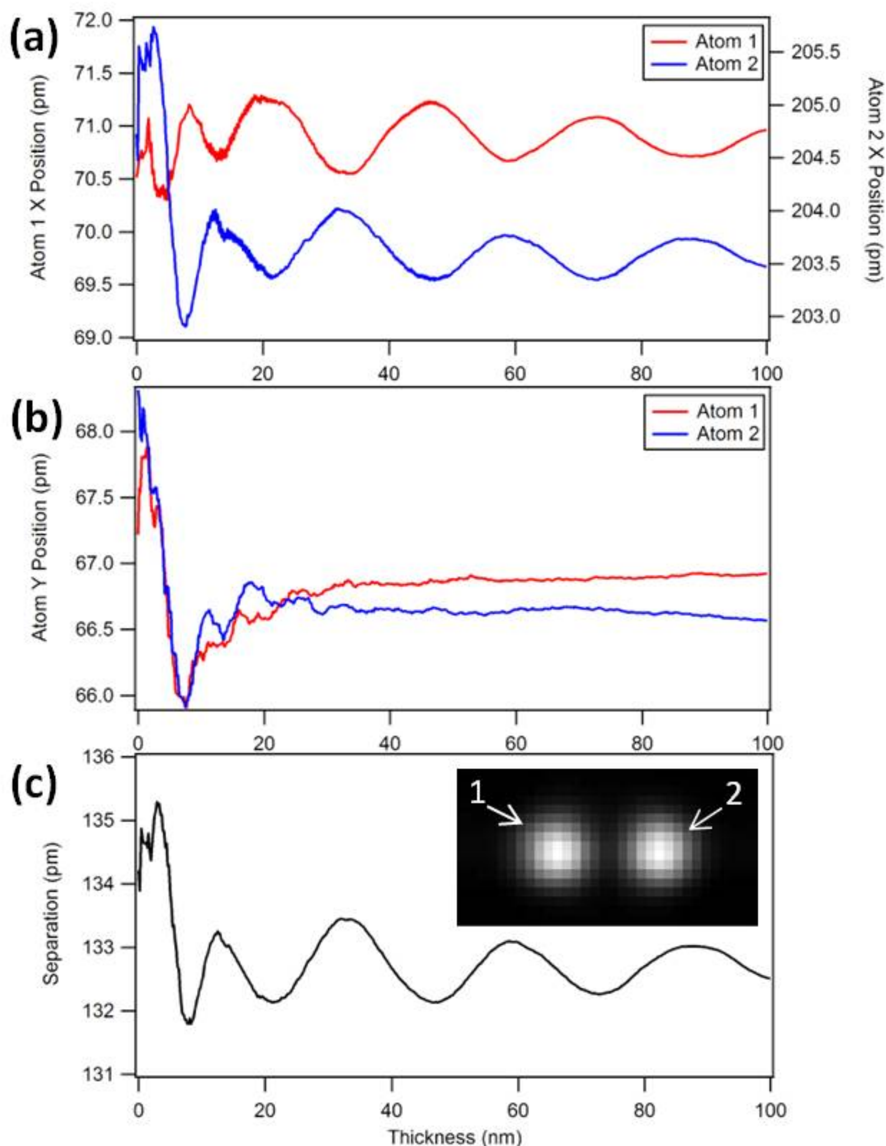

Figure 8.7: Position data from the simulated HAADF Si [110] thickness experiment. (a) Plot showing the x positions of Si column 1 and 2 as a function of model thickness. (b) Plot showing the y positions of Si column 1 and 2 as a function of thickness. (c) Plot showing the separation distance between Si column 1 and 2 vs. model thickness. The inset in (c) is the simulated HAADF STEM image of Si [110] of a model ~50 nm thick. The Si atom column on the left is Si column 1 and the Si atom column on the right is Si column 2.

33.1 Å x 31.1 Å, and was sampled with a 2048 x 2048 pixel wave function. The simulated images were not convolved with a Gaussian to account for incoherent source broadening(*40*, *48*) because this only makes atom columns wider with lower peak intensities and does not move the column's center position.

In order to test the dynamical scattering limits to precision, the atomic columns positions in the GaN and Si multislice simulations were tracked as a function of sample thickness by using the fitting algorithms introduced in Chapter 7.4. For the Si ABF and HAADF images, and the GaN ABF images, each dumbbell was fit to a sum of two two-dimensional Gaussian functions. For the HAADF GaN images, due to the Z-contrast nature of HAADF STEM images and the atomic weight difference of Ga and N, the N atomic columns are invisible. Therefore, only the Ga atomic columns were fitted to a single two-dimensional Gaussian function and those positions were studied.

Figure 8.7 shows the atomic column position results from the HAADF STEM simulations of Si [110]. The inset of Figure 8.6(c) is a simulated HAADF STEM image of Si [110] with a model thickness of ~50 nm. The x and y position of Si column 1 and 2 (marked in the inset of Figure 8.7(c)) in the HAADF image at various model thicknesses are shown in Figure 8.7(a) and (b), respectively. In the x direction, the imaged Si column positions vary by 0.5 pm at thicknesses lager than 10 nm, while at model thicknesses smaller than 10 nm, the Si column positions in the image vary by 2.5 pm. At thicknesses greater than 10 nm, the x direction motion of Si column 1 and 2 is equal and opposite in direction of one another, creating a breathing motion of the dumbbell. In the y direction, the Si column positions vary by 2 pm at thicknesses less than 10 nm, vary by 1 pm

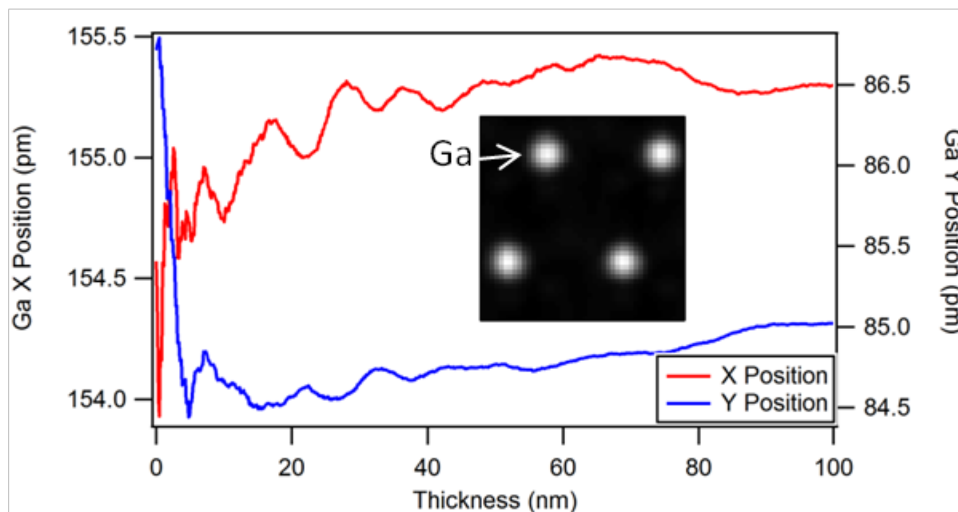

Figure 8.8: Position data from the simulated HAADF GaN $[11\bar{2}0]$ thickness experiment. Plot showing the x and y position of a Ga column as a function of model thickness. The inset is a simulated HAADF STEM image of Ga $[11\bar{2}0]$ of a model ~50 nm thick with the Ga column used for the position analysis labeled.

between thicknesses of 10 and 20 nm, and stop shifting at thicknesses greater than 20 nm. At thicknesses less than 10 nm, the position shifts in the x and y directions have similar magnitudes. At thicknesses greater than 10 nm, the position shifts in the x direction are much larger than the y direction, which correlates to an x direction breathing mode of the dumbbell that dominates the motion. The breathing motion of the dumbbell is quantified in Figure 8.7(c), which shows the separation distance between Si columns 1 and 2. The breathing motion has a model thickness period of about 25 nm and a maximum to minimum separation distance of about 2 pm.

Figure 8.8 shows the atomic column position results from the HAADF STEM simulations of GaN $[11\bar{2}0]$. The inset of Figure 8.8 is a simulated HAADF STEM image of GaN with a model thickness of ~50 nm. The x and y position of the Ga column

(marked in the inset image) at various model thicknesses are shown in Figure 8.8. In the x direction, at thicknesses less than 20 nm the Ga position varies by around 1 pm, while at thicknesses greater than 20 nm the Ga position variation drops to less than 0.5 pm and steadily flattens at larger thicknesses. In the y direction, the Ga position quickly varies by about 2 pm at thicknesses smaller than 10 nm, while at thicknesses larger than 10 nm the Ga position variation drops to less than 0.5 pm with an increasing y position.

Figure 8.9 shows the atomic column position results from the ABF STEM simulations of Si [110]. The inset of Figure 8.9(d) is a simulated ABF STEM image of Si [110] with a model thickness of ~50 nm. The x and y position of Si columns 1 and 2 (marked in the inset of Figure 8.9(d)) in the ABF image at various model thicknesses are shown in Figure 8.9(a) and (b) respectively. In the x direction, at thicknesses larger than 30 nm, the imaged Si column positions vary by up to 5 pm, while at smaller thicknesses less than 30 nm, the Si column positions vary by up to 9 pm. In addition, at thicknesses greater than 30 nm, the Si columns exhibit a x direction breathing motion. In the y direction, the Si column positions vary by 1.5 pm at thicknesses less than 30 nm, and decrease to 0.5 pm at thicknesses greater than 30 nm. At all thicknesses, the position shifts in the x direction are larger than the y direction, causing the x direction breathing mode to dominate the motion. The separation distance between Si columns 1 and 2 is shown in Figure 8.9(c). The breathing motion has a model thickness period of about 20-25 nm and a maximum to minimum separation distance of about 14 pm.

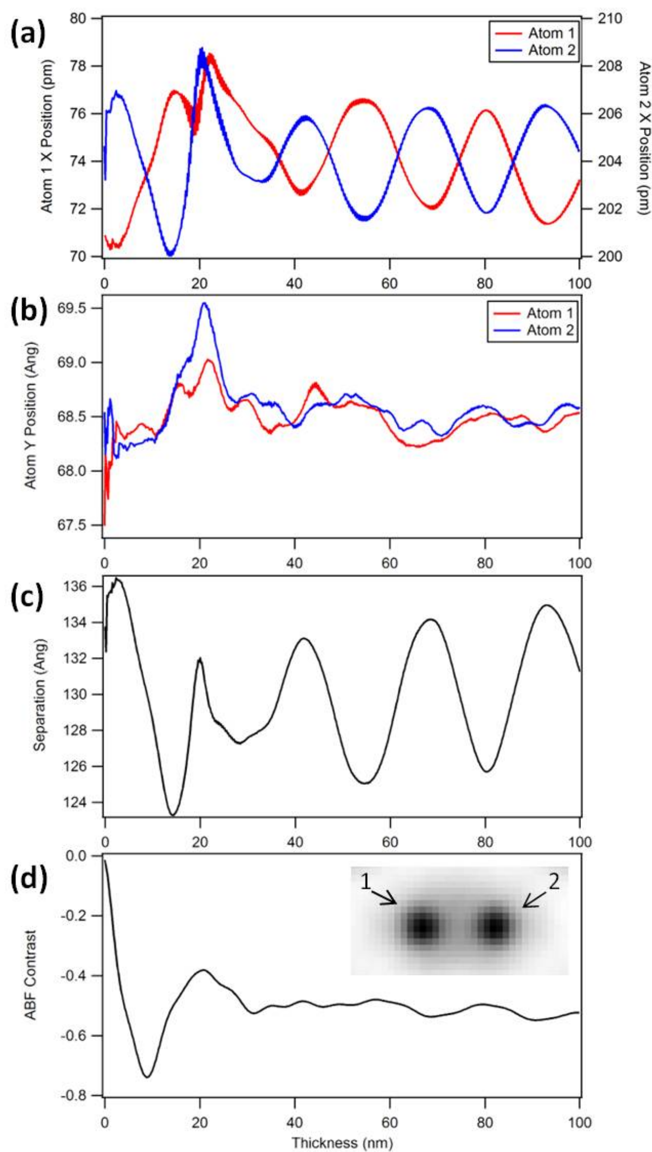

Figure 8.9: Position data from the simulated ABF Si [110] thickness experiment. (a) Plot showing the x position of Si column 1 and 2 as a function of model thickness. (b) Plot showing the y position of Si column 1 and 2 as a function of thickness. (c) Plot showing the separation distance between Si column 1 and 2 vs. model thickness. (d) Plot showing the contrast below the background intensity for each atom column in the ABF image as a function of model thickness. The inset in (d) is a simulated ABF STEM image of Si [110] of a model ~50 nm thick. The Si atom column on the left is Si column 1 and the Si atom column on the right is Si column 2.

Figure 8.10 shows the atomic column position results from the ABF STEM simulations of GaN $[11\bar{2}0]$. The inset of Figure 8.10(c) is a simulated ABF STEM image of GaN with a model thickness of ~50 nm. The x and y position of the N column (marked in the inset of Figure 8.10(c)) in the ABF image at various model thicknesses is shown in Figure 8.10(a). The x and y position of the Ga column (marked in the inset of Figure 8.10(c)) in the ABF image at various model thicknesses is shown in Figure 8.10(c). In the x direction, the N atom column position varies by about 14 pm, while the Ga position only varies by about 5 pm. In the y direction, the N atom column position varies by about 10 pm, while the Ga position varies by about 7 pm. The motion of the Ga and N columns is primarily along a direction pointing between the two atom columns, and associated with a breathing motion. This motion is displayed in Figure 8.10(c), which shows the separation distance between the Ga and N position at various model thicknesses. The separation distance between the Ga and N columns varies by up to 18 pm, with larger variations observed at model thicknesses smaller than 30 nm.

Figure 8.9(d) and 8.10(d) show the contrast below the background intensity for each atom column in the ABF STEM image as a function of model thickness from the Si and GaN simulation experiments respectively. Some of the local maximum, minimum and cross over points in the contrast plots occur at the same model thicknesses as the local maximum, minimum and cross over points in the atom position plots. We do not have an explanation for this yet, but this suggests a similar cause for contrast variation and atom position movement in the ABF STEM images.

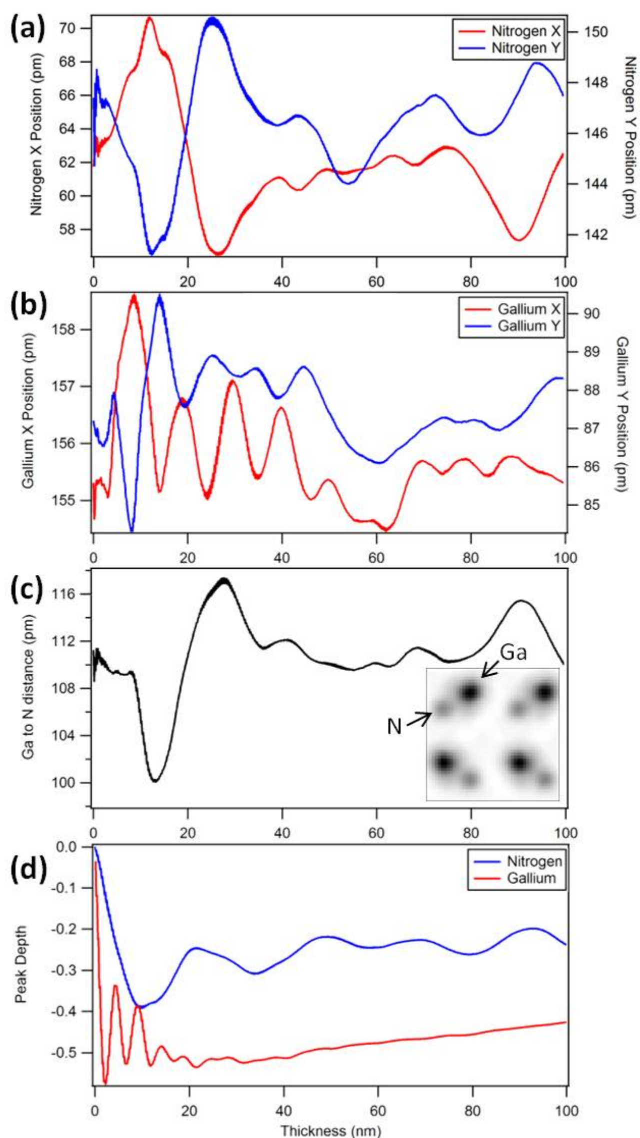

Figure 8.10: Position data from the simulated ABF GaN $[11\bar{2}0]$ thickness experiment. (a) Plot showing the x and y position of the N column labeled in the inset of (c) vs. thickness. (b) Plot showing the x and y position of the Ga column labeled in the inset of (c) vs. thickness. (c) Plot showing the separation distance between the Ga and N columns vs. model thickness. The inset in (c) is a simulated ABF STEM image of Ga $[11\bar{2}0]$ of a model ~50 nm thick with the Ga and N columns used in the position analysis labeled. (d) Plot showing the Ga and N contrast below the background intensity for each atom column in the ABF image as a function of model thickness.

The position results indicate the atomic column position shifts in HAADF images are similar to the STEM precision limits and might just barely be detectable, while the atomic column position shifts in ABF images are large and should be experimentally noticeable. From HAADF STEM images, without knowledge of sample thickness, the actual position of Si and Ga atoms could be a few pm away from the apparent positions in the image. From ABF STEM images, without knowledge of sample thickness, the actual position of Si atoms in a Si [110] structure could be around 14 pm away from the apparent positions in the image, and the actual position of Ga and N atoms in a GaN $[11\bar{2}0]$ structure could be around 18 pm away from the apparent positions in the image. With new STEM techniques pushing the precision limits to the sub-pm scale, this dynamic scattering precision limit cannot be overlooked.

Dynamical scattering and electron channeling of the high energy electron beam is responsible for the varying atom column positions with sample thickness in HAADF STEM images along high symmetry zone axes (*219*). In STEM, the scattering responsible for image creation is caused by the electron probe quantum mechanically interacting with the available Bloch states of the crystal. The general solution of dynamical diffraction requires using hundreds of Bloch states to quantitatively capture the correct interactions and scattering. To make this problem easier to solve and to give qualitative and not quantitative results, approximations can be made that only include specific Bloch states into the analysis. In the 1s model, the most important Bloch states that represents the localized interactions to the atomic nucleus are considered and the rest are ignored. In this model, each atomic column has an independent localized state that

the probe couples to(*222*). The bonding/antibonding model includes the situation when two atomic columns are close enough to interact and create 2 shared states, similar to the bonding and antibonding states created by hybridization in molecular orbital theory. As Hovden *et al.* (*219*) explains, the excitation of a particular antibonding or bonding Bloch state by an electron probe varies with probe position because the states have different probability density distribution shapes and locations of maximums and minimums. The interference between the two states also varies as a function of sample depth, causing variations in state excitation with sample thickness. In HAADF STEM images, Hovden *et al.* reports the antibonding state associated with a Si [211] crystal cause the Si dumbbells to appear wider in the STEM image than the actual spacing and the magnitude of the broadening depends on sample thickness(*219*). This observation and explanation is consistent with our results.

ABF and HAADF utilize the same sub-Angstrom electron beam to interact with the same Bloch states of the sample. The only difference between the two imaging modes is where in the diffraction pattern the electrons are detected. Since it is known that interference and splitting of the electronic states affect the scattering of electrons to the HAADF detector region and lead to changes in atom column positions in HAADF images, it is not farfetched to assume the same occurs in the ABF detector region. In fact, our results indicate this effect is enhanced in the ABF region, leading to more atom column movement compared to HAADF images. The increased Bragg scattering present in the ABF region of the diffraction pattern is the likely cause of the enhanced atomic column position variability in the ABF images.

By combining a set of experiments and multislice image simulations, the precision uncertainty imposed by dynamical scattering can be overcome. An iterative optimization scheme, similar to that used by Thust *et al*.(*223*), could be utilized to find the true atom column positions from their apparent positions in experimental STEM images and PACBED patterns from the same area.

8.5. Conclusions

NRR of atomic resolution HAADF STEM image series allows for sub-pm precision of locating atomic columns in single crystal GaN and Si, which is the best reported in electron microscopy. NRR achieves 5-7 times better precision than rigid registration, the most widely used registration scheme for STEM imaging. Studies of precision as a function of number of images NRR and averaged showed that the available precision saturates after about 200 images for these experiments. Studies of atom column width as a function of number of images NRR and averaged showed that no substantial loss of resolution is introduced by the NRR of experimental HAADF STEM image series.

A simulation study on Si [110] and GaN $[11\bar{2}0]$ found that dynamical scattering and electron channeling limits the HAADF and ABF STEM image precision to ~1 pm and 10-20 pm respectively. The precision limits to HAADF STEM images are close to what is experimentally observed. However, the precision limits introduced by dynamical scattering for ABF STEM are larger and should be experimentally observable. These effects are dependent of the material, zone axis, and imaging conditions, highlighting the need to combine simulations and experiments to interpret high precision STEM images.

Chapter 9: Surface Atom Bond Length Variation and 3D Structure Determination of Pt and Au Nanoparticles

9.1. Introduction

Nanoscience and nanotechnology require determination of the structure of heterogeneous, nanometer-scale materials that often depend on their surfaces for important properties. Determining the atomic structure of these objects with sufficient resolution and precision has earned the name "the nanostructure problem" due to its difficulty(*224*, *225*). Metallic heterogeneous nanocatalysts, such as crystalline Pt and Au nanoparticles (NPs), are one prototypical example of "the nanostructure problem". Pt NPs are used for various catalytic reactions(*226*–*228*), and controlling their morphology is crucial to determining their chemical activity. For example, crystalline Pt NPs exhibit much higher catalytic activity than disordered NPs(*229*), and faceted rather than spherical Pt nanocrystals show even higher activity(*230*, *231*), which varies depending on what facets and edges are exposed(*232*, *233*). Density functional theory (DFT) calculations show that surface steps and edges have different local electronic structure that influence the overall catalytic activity(*234*, *235*), showing the importance of measuring these local atomic structures to the complete understanding of the catalytic function of Pt NPs. Wide-angle scattering and computational techniques are making rapid progress in addressing the nanostructure problem(*236*, *237*), but microscopy remains an essential tool because of its ability to directly interrogate individual structures and their surfaces.

The ability to gain structural information along the electron beam direction is inherently difficult using TEM and STEM imaging because of their projection nature. To

overcome this hurdle, three-dimensional structural data can be extracted from two-dimensional images at nearly atomic resolution using several approaches(*238–240*). The standardless atom counting approach uses quantitative comparison between simulations and experiments to count the number of atoms in images of atomic columns. The uncertainty in these measurements is a few atoms and has been limited by the image Poisson noise. If the SNR can be increased enough, the Poisson noise contribution to the uncertainty could be decreased and made unimportant, and an uncertainty of less than 1 atom could be achieved.

In this study, the high precision NRR STEM technique discussed in Chapters 7 and 8 was used to measure pm-scale bond length variations of surface atoms on a Pt nanocatalyst, providing the surface structure of important active sites with higher precision than ever before achieved. The Pt nanocatalyst results show large bond length contraction at a $(1\bar{1}1)/(\bar{1}\bar{1}1)$ corner and significant expansion along a $(1\bar{1}1)$ surface facet. In addition, NRR has allowed for standardless atom counting(*19*) using the same Pt nanocatalyst data set with less than 1 atom uncertainty for a majority of the Pt atom columns, pushing the uncertainty limit of the technique past the previously encountered Poisson noise limit.(*241*)

The primary drawback to the NRR high-precision STEM technique is the large dose resulting from the multiple image series required to get the increased SNR. This makes high precision imaging either difficult or impossible for beam sensitive materials. The dose can be limited by decreasing the number of images in the NRR and averaged image series, as done in the Pt nanocatalyst results. However this also limits the resulting

image precision by reducing the collected electrons. Four other common methods in STEM to decrease the dose also have adverse effects on the image precision. First, decreasing the pixel dwell time will decrease the dose to the sample, but it will also decrease the signal collected at each pixel and decrease the SNR, compromising the image precision. Second, decreasing the probe current will decrease the dose to the sample, but it will also have a similar effect as the first method. Third, increasing the pixel size by sampling the same area of the specimen with a coarser pixel grid will decrease the dose to the sample, but it will also decrease the number of pixels per atomic column, possibly reducing the ability to locate the atomic column positions and compromising the image precision. Fourth, increasing the pixel size by decreasing the microscopes image magnification while keeping the same number of pixels in the image will decrease the dose to the sample, but it could have a similar effect as the third method.

In addition to the Pt nanocatalyst results, this chapter also shows that 1-2 pm image precision is possible by NRR and averaging HAADF STEM image series of a 5-6 nm Au nanoparticle even though a very coarsely sampled image and decreased exposure time were used to minimize the electron dose. These imaging conditions minimize the damage to the nanoparticle and capture the whole nanoparticle in the same image. The high precision STEM image reveals bond length contraction around the entire Au nanoparticle surface, and no bond length variation along a twin boundary that separates the nanoparticle into two grains.(*242*)

9.2. Material Synthesis

Steven Bradley and Sergio Sanchez from UOP Honeywell supplied the Pt NP catalyst TEM sample. It was created by impregnating amorphous silica with a total of 0.35% Pt followed by a heat treatment at 525 °C as described by Jackson *et al.*(*243*), resulting in 1-7 nm Pt NPs scattered on a silica support. The TEM sample was prepared by dispersing crushed catalyst material onto a lacey carbon support TEM grid.

The ~5 nm diameter colloidal Au nanoparticles were synthesized using the phosphorus method in aqueous solution. The Au nanoparticle STEM sample was prepared by dispersing colloidal Au nanoparticles onto a nonpourous 5 nm thick Si membrane window grid. Prior to STEM experiments, the sample was annealed under vacuum for 48 hours at 200°C and then plasma cleaned in a Fischione plasma cleaner in 25% oxygen−75% argon mixture for ∼5 min to reduce organic carbon surface contamination.

9.3. Pt Nanocatalyst Atomic Surface Structure

Figure 9.1 shows results from the NR registration of a HAADF STEM series of a [011] 6.5 nm Pt catalyst NP on a silica support. A lower electron dose compared to the experimental single crystal results shown in Chapter 8, implemented by increasing the pixel size and reducing the number of frames in the series, was used for this experiment to minimize electron irradiation damage of the Pt NP. The series consists of 176 HAADF STEM images with 256 by 256 pixels, 13 μs/pixel dwell time, and 21.45 pm/pixel sampling. The series was truncated to the first 56 images for analysis, beyond which the

motion of surface atoms was more visible and large sample drift caused lack of overlap with the original sample area. Figure 9.1(a) shows the first image of the series. Figure 9.1(b) shows the NR registered, then averaged image on an absolute intensity scale. It was acquired with a total dose of 4,450 C/cm^2 and a total dwell time of 0.728 msec/pixel. The Pt column labeled as M has an integrated intensity of 2.6 x 10^6 e$^-$. The Pt atomic column positions were determined by fitting each to a single 2D Gaussian function using the methods discussed in Chapter 7.4. Figure 9.1(c) and (d) are representative fit residuals of one interior and one surface Pt column marked by M and I respectively. They show some diagonal structure due to either sample mis-tilt or residual aberrations like astigmatism, but because they are symmetric about the column position, they have very little effect on the extracted atomic column position.

The precision in the Pt NP average image was determined from 53 interior Pt atom columns at least 5 atomic planes from the surface. The standard deviation of the measured *a* and *b* separations, defined in Figure 9.1(b), yields σ_a = 2.5 pm and σ_b = 1.3 pm, while the fit position uncertainties yield σ_x = 1.5 pm and σ_y = 1.6 pm. The reduced precision compared to the Si and Ga results in chapter 8 arises from a decreased SNR due to the lower dose required to avoid damage, and the lower scattering power of the very small NP. The similarity of the two measures of precision indicates the instability and the SNR precision limits are about the same in this experiment.

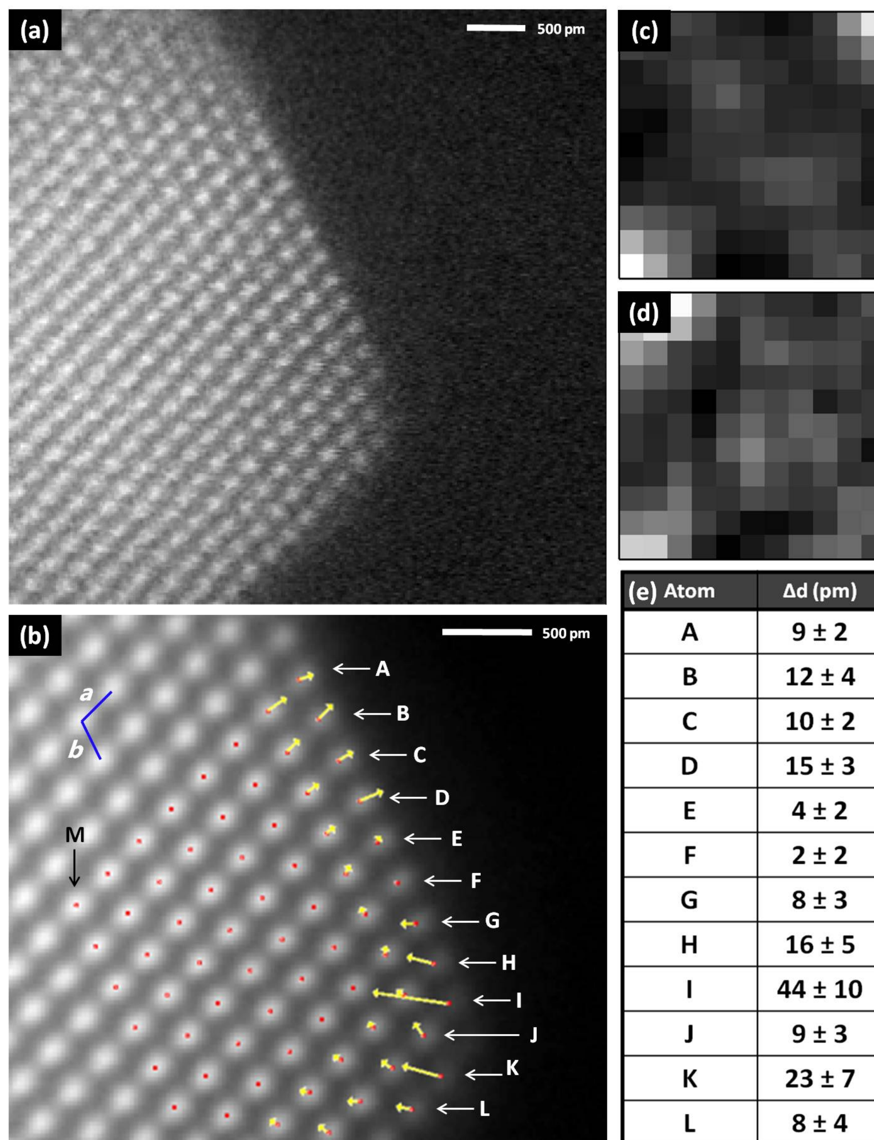

(e) Atom	Δd (pm)
A	9 ± 2
B	12 ± 4
C	10 ± 2
D	15 ± 3
E	4 ± 2
F	2 ± 2
G	8 ± 3
H	16 ± 5
I	44 ± 10
J	9 ± 3
K	23 ± 7
L	8 ± 4

Figure 9.1: (a) The first raw HAADF STEM image of the Pt NP [011] series. (b) The average image after the NR registration. The red markers are the atomic column positions determined from fitting, and the yellow arrows are magnified atom column displacement vectors. (c) and (d) The fit residuals for the columns M and I, respectively, in (b). The maximum intensity in (c) is 2.8 % of the column peak intensity due to slight overlap with a neighboring atom column. (e) The displacement magnitudes of the labeled atoms in (b).(*241*)

Figure 9.1(b) shows the displacements of the surface Pt atoms with respect to the atomic lattice of the particle interior. A perfect reference lattice was constructed by calculating the average *a* and *b* of interior atomic columns, creating a perfect grid of positions from the average *a* and *b*, registering that grid to the fitted atomic column positions from the precision area, and then extending the perfect grid to all atomic columns. The average displacement between the reference lattice positions and the interior atom column positions is 2.0 pm, consistent with the measured image precision. The red markers in Figure 9.1(b) indicate the Pt atom column positions from fitting. The yellow arrows in Figure 9.1(b) indicate the magnitude and direction of the measured displacements (length is longer than the image scale) away from the reference lattice positions of the atomic columns. The measured displacements of the labeled atom columns in Figure 9.1(b) are shown in the table in Figure 9.1(e). The uncertainties in the displacements are the average of the *x* and *y* fit position uncertainties weighted by the angle of the displacement vector.

The 2D projection nature of STEM images makes it impossible to extract the [011] component of the atom displacements along the electron beam direction. Within this limitation, the displacements of atom columns A though D show bond length expansion primarily along $[1\bar{1}1]$ away from the NP center, while atom columns G though L show bond length contraction primarily along $[01\bar{1}]$ towards the NP center. Some bond length expansion is also seen in the sub surface $(1\bar{1}1)$ plane under atom columns A-D. All the displacement uncertainties for atom columns A-D and G-L are smaller than the measured displacement. The small displacement of columns E and F are similar to

the uncertainties, but these are the transition surface atoms between the bond length contraction of atoms columns G-L and bond length expansion of atom columns A-D. The corner atom column marked as I shows the largest bond length contraction of 18.5 ± 4.1% of the 2D lattice parameters *a* or *b*. The $(1\bar{1}1)$ facet atom column marked as D shows the largest bond length expansion of 6.4 ± 1.1%.

Flat metal surface atoms have been observed to have bond contraction using a variety of experimental techniques(*244*, *245*). This can be explained due to the electrostatic force created by the electronic charge at the surface rearranging itself to minimize its kinetic energy(*246*, *247*), or the lower coordination of surface atoms(*248*). Both these explanations predict a larger bond contraction of corner atoms near facet edges and steps, consistent with our observation of bond length contraction near the NP tip. Our observations of varying magnitude and direction of the contraction, along with the observed expansion of the $(1\bar{1}1)$ surface facet, are not captured by the previous experiments and theory of 2D surfaces. This disconnect emphasizes the need for experiments and calculations to be conducted on real 3D structures and not on just idealized 2D surfaces.

Our results both agree and disagree with previous microscopic investigations. Chang *et al.* conducted comparable measurements on Pt nanocatalysts on a carbon support using aberration-corrected TEM exit-wave reconstruction(*249*, *250*). Huang *et al.* used coherent electron nanodiffraction on faceted Au NPs dispersed on graphene(*251*). The bond length contraction near the corner in Figure 9.1(b) is in reasonable agreement with Huang's report of 22 pm contraction of edge and corner

bonds, but in disagreement with Chang's report of 14-30 pm bond length expansion of a similar (110)-(1x1) reconstructed $(1\bar{1}1)/(\bar{1}\bar{1}1)$ corner. However, Chang also reports DFT calculations, which predict a slight contraction of a (110)-(1x1) reconstructed $(1\bar{1}1)/(\bar{1}\bar{1}1)$ corner, in reasonable agreement with our results. We report expansion of a $(1\bar{1}1)$ surface, and so does Chang, but Huang reports only contraction of similar surfaces. Huang's method, coherent electron nanodiffraction, measures the shape function of the nanoparticles and is most sensitive to the nanoparticle edges and corners instead of gradual changes on surface facets. Therefore, small expansions of flat surface facets might be difficult for nanodiffraction to capture, possibly explaining the discrepancies with our results. We report very little lateral displacements (vectors pointing along the nanoparticle surface), but Chang reports significant lateral displacements along the surface. The lateral displacements in Chang's results are attributed to microrisers (single atom steps) on the nanoparticle surface. These are not present on our nanoparticles and may be an explanation of this discrepancy. However the lateral displacements in Chang's results appear random, implying their experiment is not capturing the real behavior of the surface atoms, possible because of atom motion during image acquisition. Now, high precision STEM imaging is another technique quantitatively capable of addressing these discrepancies, and will allow further measurements of NP surfaces in order to determine the correct surface structures.

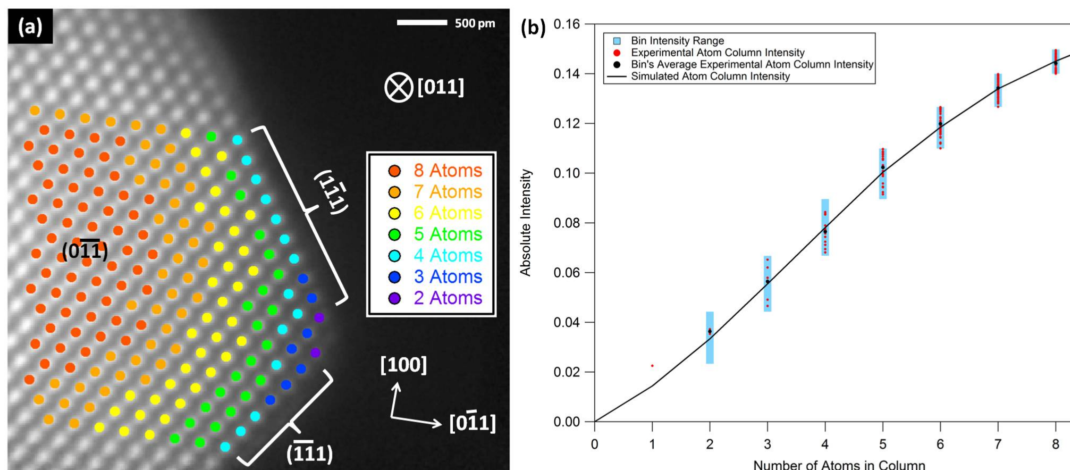

Figure 9.2: (a) The number of atoms in each column determined by comparing the experimental absolute intensities to simulations. (b) Comparison of the experimental and simulated Pt atom column intensities. The light blue intensity ranges signify the bin intensity ranges for each number of Pt atoms in a column. The boundaries of the blue intensity ranges were determined by conducting a cubic interpolation of the simulated intensity vs. number of Pt atoms data and setting bin boundaries at the interpolated intensity value of the midpoint between numbers of atoms in a column. The red circle markers indicate the experimental Pt column intensities in the bin they were assigned to. The black circle markers indicate the average experimental Pt column intensity of each bin. The black line indicates the simulated Pt column intensity as a function of the number of Pt atoms in the column.(*241*)

To extract three-dimensional information from the two-dimensional image in Figure 9.1(b), we determined the number of atoms in each Pt column of the experimental image using LeBeau's standardless atom counting method(*239*), in which the experimental intensity is compared to simulations(*41*) by expressing both as a fraction of the incident probe intensity. The experimental intensity was calculated as the average in an 85 by 85 pm window centered on each Pt column marked in Figure 9.2(a). The silica support scattering of 0.095, estimated as the average intensity of a window off of the NP,

was subtracted from the experimental column intensities. For comparison, the experimental intensity of Pt column J in Figure 9.1(b) before background subtraction is 0.15285. Images of a Pt [011] atom column of varying thickness were simulated using 160 phonon configurations and a Debeye Waller factor for Pt of 0.3557 Å^2, taken from Peng *et al.*(*252*). The Pt [011] crystal was 33 Å x 31 Å, and was sampled with a 2048 x 2048 pixel wave function. The simulated images were convolved with a Gaussian to account for incoherent source broadening(*40*, *41*), then the average simulated intensity was calculated from the same sized window as the experimental image centered on the simulated Pt column as a function of thickness.

Figure 9.2(a) shows the number of atoms in each Pt column by comparing the experiment to the simulations. This area of the NP has between 1 and 8 atoms per Pt column. The well-defined terraces and monatomic steps arose naturally from the quantitative comparison and were not forced to occur. The NP has two {111} surfaces out of the image plane that are 4 atoms thick and thin to 2 atoms thick near the intersection of the two facets at the $(1\bar{1}1)/(\bar{1}\bar{1}1)$ corner. There is a flat $(0\bar{1}\bar{1})$ surface facet in the image plane in the 8 atoms thick region. Because of the 2D projection nature of STEM images, it is impossible to distinguish what surface (top or bottom) the monatomic surface steps occupy. However, assuming that the metal-support interaction results in a flat (011) plane against the silica support and all the steps are on the opposite surface(*253*), the particle consists of 1-2 atom wide $(0\bar{1}\bar{1})$ terraces that have monatomic $(1\bar{1}1)$ and $(\bar{1}\bar{1}1)$ steps propagating from the out-of-plane $(1\bar{1}1)$ and $(\bar{1}\bar{1}1)$ facets to the

in-plane $(0\bar{1}\bar{1})$ facet. The edges that create this terraced structure generally run parallel to the $(1\bar{1}1)$ and $(\bar{1}\bar{1}1)$ surface facets.

There is intensity consistent with 1 atom at the very tip of the NP corner between atoms I and K. The intensity at this position does not form a peak distinct enough for fitting to determine the position, but we speculate that there was a single atom here, and it was moving during acquisition. The summed intensity at this position is not less than one atom, so we believe it experienced large motions near its lattice site, probably excited by the electron beam, but it was not displaced from the NP by the electron beam.

Figure 9.2(b) shows the intensity values for experimental and simulated Pt columns containing 1 to 8 atoms. The experimental intensities are almost continuous when the number of atoms is larger and are well separated for small numbers of atoms. To assign each column a number of atoms, we created intensity bins defined by the midpoints between different numbers of atoms on a cubic spline fit to the simulated intensities (the black line in Figure 9.2(b)). These intensity bins are shown as the light blue ranges in Figure 9.2(b). The average of the experimental intensities within each bin (the black dots in Figure 9.2(b)) matches very close to the simulated intensity for that number of Pt atoms.

Unlike previous work(*19*), Poisson noise in the atom intensity is not the limiting factor in assigning a number of atoms to a particular column. In these results, the variability in the support scattering is a larger contribution to the uncertainty in the number of atoms in each column than the Poisson noise. Support scattering and other potential effects mean that ~40% of the atoms could have one more or one less atom than

shown in Figure 9.2(a). The assignments for the other ~60% of the atoms are unique. Extreme variation in support window size and location towards areas further away from the Pt NP alters Pt column intensities enough to at most shift the number of atoms per Pt column label up by 1 atom for at most 84 of the 188 Pt columns. The variation in support scattering from the background subtraction area is 71 e^- and the Poisson noise in the support scattering is 160 e^-, both of which are less than the 316 e^- bin width for the narrowest 8 atom bin. The Poisson noise for the mean intensity of the 8 atom bin is 165 e^-, which is about half the 316 e^- bin width. Properly combining the Poisson noise in the support scattering, the variation in support scattering, and the Poisson noise for the mean intensity of the 8 atom bin shows the uncertainty of the atom assignments in the 8 atom bin is 240 e^- ($\sqrt{(160^2 + 71^2 + 165^2)}$), which is 75% of the 8 atom bin width. Because these values are smaller than the bin widths, we expect to see clusters in intensity near the middle of the bins, instead we see nearly uniform distribution of intensities from especially in the 5-8 atomic columns. Possible explanations for this include things like sample mis-tilt, residual aberrations, variation in local Debye-Waller factor based on the NP structure, and the failure of the phase-grating approximation for single atoms of heavy elements like Pt. The explanation does not include the Poisson noise and variation in support scattering by themselves since their components are smaller than the bin widths.

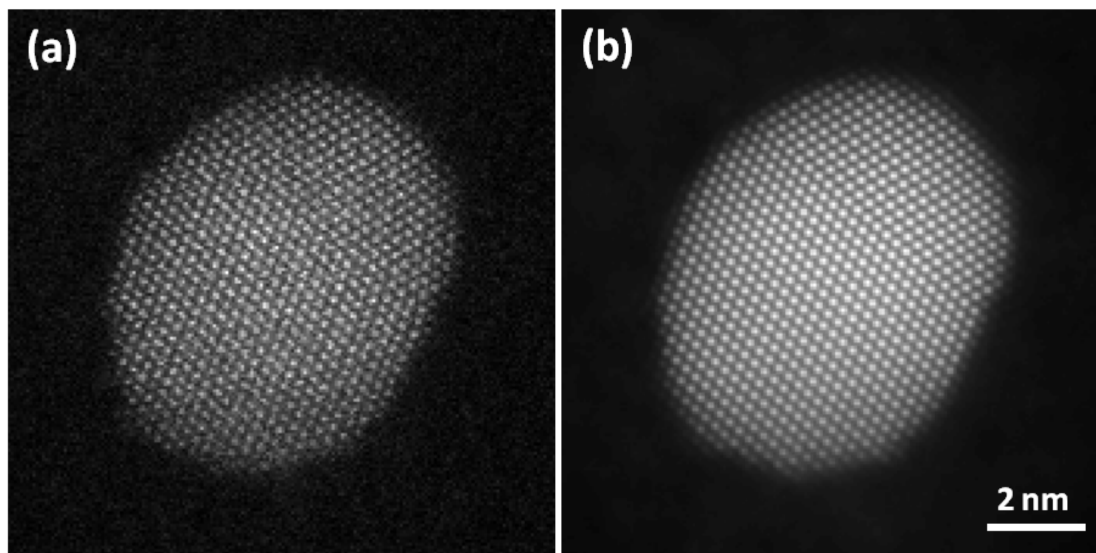

Figure 9.3: (a) The first raw HAADF STEM image of the 240 image series of a Au nanoparticle along [110]. (b) The average image after the NRR of the Au nanoparticle image series.(*242*)

9.4. Au Nanoparticle Atomic Surface Structure

A HAADF STEM image series consisting of 240 images of a Au NP along [110] was acquired with 256 x 256 pixels with ~60 pm/pixel and a 5 μs/pixel dwell time, using a total dose of ~850 C/cm^2. This dose is still high, but it is 1% of the dose previously used for sub-pm precision on single crystal samples and 19% of the dose used for a few picometer precision on a Pt nanoparticle. Figure 9.3(a) shows the first image of the 240 HAADF STEM image series of the Au NP. The 240 image series was NRR and averaged to increase image SNR and to remove all sizes of distortions introduced by instabilities during image series acquisition. Figure 9.3(b) shows the averaged image after NRR, representing the average sample structure over the series acquisition time and displaying enhanced SNR ratio compared to the first frame in Figure 9.3(a). Fast processes like thermal displacements and atom displacements from electron beam

momentum transfer are not captured because of the long acquisition time, and atomic column distortions from circular symmetry are likely due to the electron probe's residual lower order aberrations.

The Au nanoparticle displays two grains separated by a twin boundary, providing two separate areas for determining image precision. The atomic columns at least 5 planes away from the NP surfaces and twin boundary were used for the precision analysis. Their positions were determined by fitting a 2D Gaussian function to a 4 by 4 pixel area using the methods discussed in Chapter 7.4, and are shown by the red markers in Figure 9.4(a) and (b) for the top and bottom grains respectively. The interatomic separations were calculated in the *a* and *b* directions (defined in Figure 9.4(a)) for the top grain and the *c* and *d* directions for the bottom grain. The image precision σ, defined as the standard deviation of the interatomic separations(*241*, *254*), is measured to be σ_a = 2.00 pm, σ_b = 1.96 pm, σ_c = 1.38 pm and σ_d = 1.90 pm. Even though the pixel size in this data set is 59.93 pm/pixel, and only a 4 pixel by 4 pixel area was used to do each atomic column fitting, 1-2 pm precision is still achieved, allowing atomic columns to be located with a precision of 3% of the pixel size. The picometer-scale precision in course-samples images enables the measurement of lattice strains to ~1% that are commonly associated with defects, interfaces, ion displacements, and surface relaxation at lower image magnification and lower dose than our previous work.

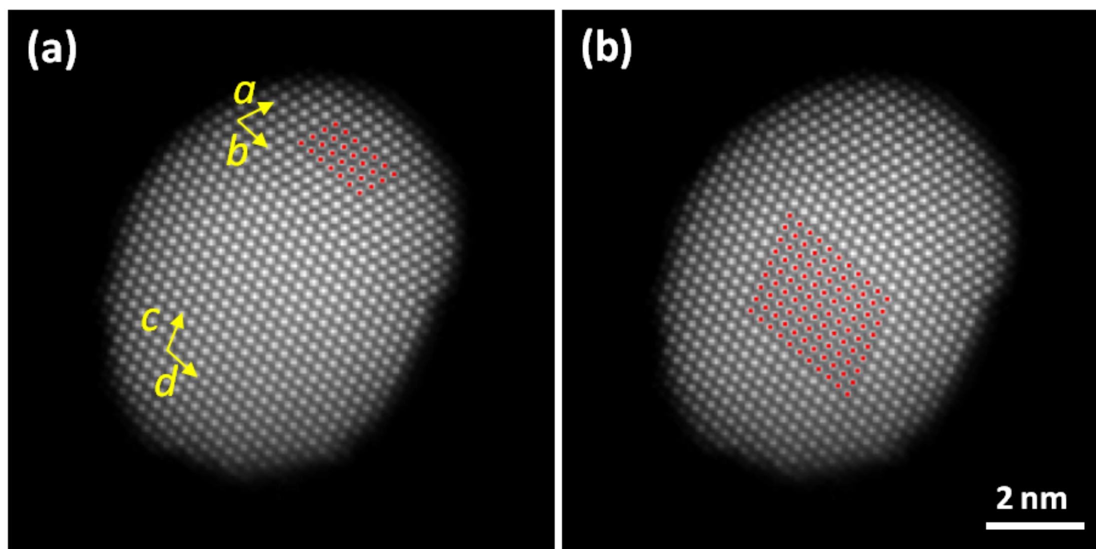

Figure 9.4: The NRR and averaged image with the (a) top grain's and (b) bottom grain's precision area fit positions labeled by red markers. The yellow arrows signify the directions of the measured interatomic separations for the precision analysis.(*242*)

The bond length variation of the Au NP was measured in a similar way as the Pt NP, as shown in Figure 9.5. A perfect reference grid was constructed for each grain separately to measure the surface atom displacements. The red and blue markers in Figure 9.5(a) represent the perfect reference grid where the atomic columns would be if no strain were present in the nanoparticle. Each atomic column of the nanoparticle was fit to a 2D Gaussian function to find its position, as shown by the red markers in Figure 9.5(b). The yellow arrows in Figure 9.5(b) are magnified displacement vectors between the fit positions and the perfect grid, and represent the bond length variation near the nanoparticle surface. Figure 9.5(c) is a magnified image of the area within the green rectangle in Figure 9.5(b) showing more detail of the bond length variations. In Figure 9.5(c), the displacement vector labeled by the letter A represents 39 pm, and the blue

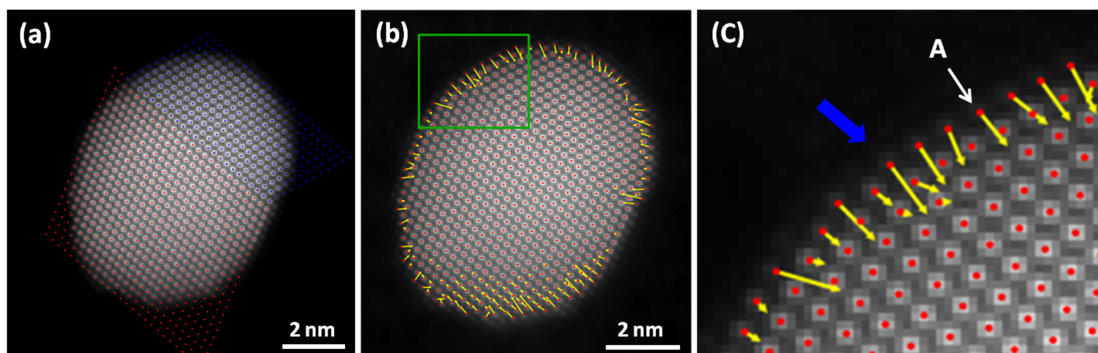

Figure 9.5: (a) The NRR and averaged image with the top and bottom grain's perfect grid labeled by blue and red markers respectively. (b) and (c) The NRR and averaged image with the fit positions labeled by red markers and the magnified displacement vectors marked by the yellow arrows. (c) A magnified image of the area within the green box in (b) with the twin boundary marked by the blue arrow.(*242*)

arrow marks the twin boundary. Similar to the PT NP data, the displacement component along the Au [110] beam direction cannot be extracted because STEM produces projection images. However, within this limitation, the Au NP displays only bond length contraction around its surface. Edge and corner atoms are observed to have larger bond length contraction than atoms present in the middle of surface facets, and the observed bond length contraction is primarily towards the NP center with very little lateral displacement. As expected, there is no bond length variation along the twin boundary.

These observations of Au NP bond length contraction agree with theoretical and experimental results. Average bond length contraction at flat metal surfaces(*244*, *245*) can be theoretically explained by the lower coordination of surface atoms strengthening and shortening the remaining bonds(*248*), or the electronic surface charge rearranging to minimize the energy and creating an electrostatic force that shortens the bonds(*246*, *247*). Both explanations predict a larger bond length contraction of corner atoms near facet

edges and steps, consistent with these observations. Microscopic investigations of faceted Au NPs dispersed on graphene using coherent electron nanodiffraction by Huang *et al.* agree with our results(*255*). Their report of bond length contraction of surface atoms as large as 22 pm for edge and corner bonds is in reasonable agreement with our observations.

High precision STEM and TEM imaging usually involves a large electron dose to the sample because it requires taking many images of the same structure to increase SNR. Therefore, for beam sensitive materials, high precision imaging is usually difficult and sometimes not possible. With beam sensitive materials, any methods to decrease electron dose and still get the quantitative information from a sample are beneficial. The results show that increasing the image pixel size almost as large as possible while maintaining atomic resolution still allows for pm-scale image precision using NRR and averaging. The coarse sampling from lowering the image magnification decreases the electron dose to the sample, reducing electron beam damage, and allows for imaging larger sample structures. This could be used for imaging whole nanoparticles with pm-scale precision (as shown here), or imaging other large structure with far reaching strain fields such as surfaces, extended defects, and interfaces.

Another strategy to reduce dose is to reduce the number of images that are registered and averaged. In the single crystal results presented in Chapter 8, precision saturated approximately half way through the data series after about 200 images. That analysis has not been duplicated here. However, in general, experiments using NRR of identical frames can trade off electron dose for SNR and precision after acquisition by

limiting the number of frames used. This balance can be chosen during post-processing depending on the magnitude of the displacements of interest and the beam sensitivity of the sample.

9.5. Conclusions

Picometer-precision enabled by NRR and averaging makes it possible to measure the small but crucial atomic displacements typical for surfaces. This technique was used to measured pm- scale bond length variations at the surface of a Pt nanocatalyst, showing large bond length contraction at a $(1\bar{1}1)/(\overline{1}\overline{1}1)$ corner but significant expansion along a $(1\bar{1}1)$ surface facet. NRR also allowed determination of 3D structural information of the Pt nanocatalyst with <1 atom uncertainty using the standardless atom counting technique, overcoming the previously seen Poisson noise limit.

1-2 pm image precision has been achieved by NRR and averaging a series of short exposure course sampled HAADF STEM images of a 5-6 nm Au nanoparticle. These imaging conditions substantially reduce the dose to the sample by having a large pixel size and low exposure time, while still achieving high precision in locating atomic columns. NRR allows for reduced magnification, capturing the whole Au nanoparticle in one high precision image. The high precision image reveals only bond length contraction around the nanoparticle surface, and no bond length variation along a twin boundary that separates the nanoparticle into two grains. Atoms present at the surface edges and corners show larger bond length contraction than atoms near the center of surface facets, consistent with theory and previous microscopic investigations(*255*). High-precision

measurements of nanocatalyst and nanoparticle surfaces, like those presented here, may enable new insight into the correlation between structure and function.

Chapter 10: Atomic Resolution EDX on Ca-doped $NdTiO_3$

10.1. Introduction

A highly desirable capability of STEM is its integration with microanalysis techniques, such as EELS and EDS. As discussed in Chapters 2.7 and 2.8, these techniques are regularly used in materials science and engineering to determine the material composition of structures like films, grains, extended defects, and nanostructures, but they can also probe material composition on the atomic level(*58*, *256*, *257*). The STEM detector geometry allows simultaneously acquisition of HAADF STEM images, EELS spectrum images, and EDS spectrum images, enabling more information to be derived from a single image experiment. However, the acquisition of atomically resolved EDS data still requires relatively high electron doses when compared to HAADF and EELS imaging because of the small signal. The high electron doses are achieved through either long pixel dwell times, usually >1 ms(*257*, *258*), or through summing the counts from multiple fast dwell time spectrum images that have been rigidly registered inline during acquisition to account for sample drift(*259*, *260*). Both of these methods produce image degradation from significant spatial drift and instabilities during acquisition. Long pixel dwell time spectrum images result in distorted images(*258*), and the summed spectrum images using short pixel dwell times result in smaller distortions but also smaller on-column X-ray intensity.

Chapters 7 – 9 show that NRR of HAADF STEM images has achieved the best image spatial precision by correcting image distortions and allowing high SNR images. The same image distortions and SNR issues that limit the precision and ability to detect

faint materials signals in HAADF STEM images also plague EELS and EDS spectrum images. Here we show that NRR of EDS spectrum images result in similar enhanced precision and chemical SNR.

Two aspects limiting the success of NRR of spectrum images are 1) the amount of signal the detector can capture, and 2) the detector spectrum acquisition speed. Both EELS and EDS rely on the inelastic scattering of incident electrons in the material. Because EELS collects the majority of incident electrons and separates them based on what energy loss they experienced while interacting with the sample, it captures almost all of the inelastic scattering events and usually has high SNR compared to EDS. EDS on the other hand relies on capturing the X-Rays emitted from inelastic scattering events, and is therefore at a disadvantage compared to EELS for two reasons. First, not all inelastic scattering events produce X-Rays, making inelastic events less detectable using EDS. Second, X-Rays from inelastic scattering events are emitted in all directions and angles from the sample, and EDS detectors only capture a very small area of the possible scattering solid angle, reducing the percentage of detected X-Rays. A typical solid angle for an EDX detector is 0.3 str, only collecting about 2 percent of the total solid angle. In addition, some of the generated X-Rays are reabsorbed by the sample, sample holder, microscope, and EDS detector window, further reducing the percentage of detected X-Rays. Despite these drawbacks, EDS has some advantages compared to EELS. EDS has significantly better signal to background that EELS and it can capture a much larger spectral energy range than EELS.

FEI has recently developed a new technology that utilizes a new high brightness gun and a quad X-Ray detector system to enhance their EDS system(*261*, *262*). The high brightness gun allows for 5 times more beam current in the same size probe compared to old electron guns, allowing for 5 times more X-Ray generation per unit time. The quad X-Ray silicon drift detector (SDD) system provides up to 10 times more detector sensitivity than their old technology by increasing the detector solid angle and removing the detector window that absorbs some of the incoming X-Rays. The windowless detector technology optimizes the detection of both light and heavy elements, and the detector electronics have been upgraded to allow EDS spectral rates of up to 100,000 spectra per second.

The deciding factor in choosing whether to implement NRR with EELS or EDS is the detector spectrum acquisition speed. NRR can only correct the distortions caused by instabilities that are actually sampled in the image series. Instabilities that are slower than the pixel dwell time can be captured and corrected with NRR. Instabilities that are faster that the pixel dwell time are averaged over during the acquisition and cannot be corrected, reducing the image quality. Pixel dwell times between 5-50 μs have shown successful results using NRR of HAADF STEM image series because the correct distortions are captured. For EELS, the fastest dwell times with current technology is on the order of 1-30 ms, much too slow to capture the relevant image distortions for NRR. This makes NRR of EELS spectrum images not possible until spectrum acquisition speeds can be improved. For EDS, the fastest dwell times with the technology on UW-Madison's FEI Titan STEM instrument is similar, on the order of 1-50 ms. However, the

new EDS technology has acquisition speeds on the order of 10-50 μs, much faster than EELS and old EDS technology, and similar to regular HAADF STEM NRR times. This makes it possible to simultaneously acquire HAADF STEM images and EDS spectrum images, and then do NRR.

The simultaneous acquisition of HAADF and EDS signals allows for NRR of EDS spectrum image series. EDS spectrum images acquired with dwell times of around 10-50 μs have extremely low SNR, even with the new high brightness gun and a quad X-Ray detector system. Most of the pixels in each frame will have 0 or 1 count, and an atomic resolution image will not be readily visible. Image series of this quality cannot be registered because of the low SNR. However, the HAADF image series at this dwell time have much higher SNR and can be easily registered using NRR. Therefore, the NRR pixel deformations can be calculated from the HAADF STEM image series and then applied to the simultaneously acquired EDS spectrum image, enabling the NRR of EDS spectrum image series.

Here, I demonstrate that the NRR of simultaneously acquired HAADF STEM image series and EDS spectrum image series of Ca-doped $Nd_{2/3}TiO_3$ is possible and improves the spectrum image quality compared to two other common EDS spectrum image acquisition techniques using similar electron doses: 1) a single long dwell time spectrum image and 2) the sum of a inline drift-corrected spectrum image series. EDS spectrum images that have been NRR are free of the large distortions present in the other two methods, and have better resolution. In the future, this technique may enable the detection of weak chemical signals, such as interstitial or substitutional dopant atom

signals, simultaneously with the high precision HAADF STEM image that can be used to measure the local strain around the point defect.

10.2. Material Synthesis

The Ca-doped $Nd_{2/3}TiO_3$ ceramics were prepared by Feridoon Azough, Demie Kepaptsoglou, Quentin M. Ramasse, Berhnard Schaffer, and Robert Freer from The University of Manchester and The SuperSTEM Laboratory in the UK(*263*). The samples were synthesized using the conventional mixed oxide method. The starting materials were high-purity $CaCO_3$, Nd_2O_3 and TiO_2 powders. The Nd_2O_3 powder was dried for 6 hours at 900°C and then all powders were wet-milled using zirconia balls and propan-2-ol for 24 hours in a vibratory mill. Then the powders were dried for 24 hours at 85°C followed by calcination for 4 hours at 1100°C. The powders were compacted into pellets (20 mm diameter by 15 mm thickness) using 50 MPa of uniaxial pressure. The pellets were sintering in alumina crucibles for 4 hours at 1450°C in air with heating and cooling rates of 180°C/hour.(*263*)

10.3. NRR of EDS Spectrum Images

Because the pixel dwell times for these NRR STEM experiments need to on the order of 10-50 μs, the FEI Titan STEM at the University of Wisconsin – Madison could not be used. I collaborated with Sarah Haigh and Thomas Slater from The University of Manchester in the U.K. who used an aberration-corrected microscope with the new quad X-Ray detector technology along with a high brightness electron gun that allows for 10-

50 μs dwell times. They acquired the data sets presented here. The current microscope software does not allow for automatic acquisition and saving of EDS spectrum image series. Therefore, the spectrum image series were acquired and saved manually, one spectrum image at a time. Each spectrum image had to be saved before the next could be acquired.

Three spectrum images were acquired with different methods from nearby areas of the same sample to compare the resulting spectrum image quality. A probe current of 300 pA and a spectrum image size of 256 x 256 x 2048 pixels was used for all experiments. The spatial pixel size was ~34 pm/pixel and the energy dispersion was 0.01 keV/channel with a -0.48 keV offset of the first channel. All three methods to acquire spectrum images used approximately the same electron dose. The three spectrum images were acquired with the following methods: 1) A single long dwell time spectrum image acquired using a pixel dwell time of 5 ms. 2) A sum of 100 separate fast dwell time spectrum images that were registered during acquisition using the inline drift correction software. The drift correction software utilizes rigid registration of images of a nearby reference region of the sample to calculate the drift of the imaged area and then accounts for that drift in between each image acquisition. A pixel dwell time of 50 μs/pixel was used. 3) A sum of 98 separate fast dwell time spectrum images that were NRR after acquisition. The calculated pixel shifts from the NRR of the simultaneously acquired HAADF STEM image series were used to register the EDS spectrum image series. 100 separate spectrum images were acquired, but only 98 were used because the NRR failed to register 2 of the frames due to extreme distortions. These two frames were not

included in the final summed spectrum image. A pixel dwell time of 50 μs/pixel was used was used for each image in the series. The total number of X-Ray counts in each of the three methods are 1) 2.05932 x 10^6, 2) 2.24446 x 10^6, and 3) 1.95272 x 10^6. The slightly reduced value for the NRR and summed spectrum image is due to only using 98 spectrum images in the sum and the slight reduction in the original image area due to sample drift, which does not occur in the other two methods.

The NRR of the EDS spectrum image series was complex and required some algorithm development. First, the simultaneously acquired HAADF STEM series was NRR registered like normal and the distortion vector for each pixel in the series was calculated. Then 2048 separate image series, one for each energy channel, containing 98 images each were created from the 98 EDS spectrum images. To do this, the first channel's image was extracted from each of the 98 spectrum images and inserted into a new image series in order. Then, the second channel's image was extracted from each of the 98 spectrum images and inserted into a different new image series in order. This was done for all 2048 channels, producing 2048 separate image series, one for each energy channel. Next, the pixel distortion vectors calculated by the NRR of the HAADF series were applied to each one of the 2048 channel image series. Then, the 2048 channel image series were disassembled (opposite of how they were assembled) and reassembled to create 98 spectrum images corresponding to the original spectrum images except they have been NRR. Lastly, the 98 NRR spectrum images were summed together to produce the final spectrum image. These algorithms can be found at the github link given in Chapter 7.4.

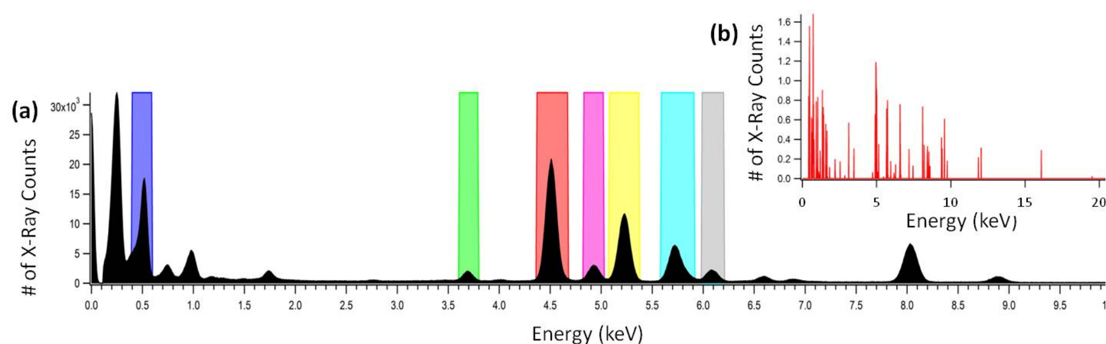

Figure 10.1: (a) Integrated spectrum of the whole NRR and summed spectrum image series. (b) Spectrum of one pixel from one NRR spectrum image from the 98 spectrum image series.

Figure 10.1 (a) shows the integrated spectrum profiles of the whole NRR and summed spectrum image series. The dark blue window represents the area of the oxygen Kα peak. The green window represents the area of the calcium Kα peak. The red window represents the area of the titanium Kα peak. The pink window represents the area of the titanium Kβ peak. The yellow window represents the area of the neodymium Lα peak. The light blue window represents the area of the neodymium Lβ peak. The grey window represents the area of the neodymium Lβ4 peak. The other peaks are smaller peaks from sample elements, or from carbon contamination (0.25keV), the copper sample holder (8-9 keV), and the Si detector (1.75 keV). Figure 10.1(b) shows the spectrum profile of one pixel from one spectrum image from the 98 spectrum image series, displaying very few counts. There are non-integer counts because the NRR algorithm implements sub-pixel shifts using bilinear interpolation.

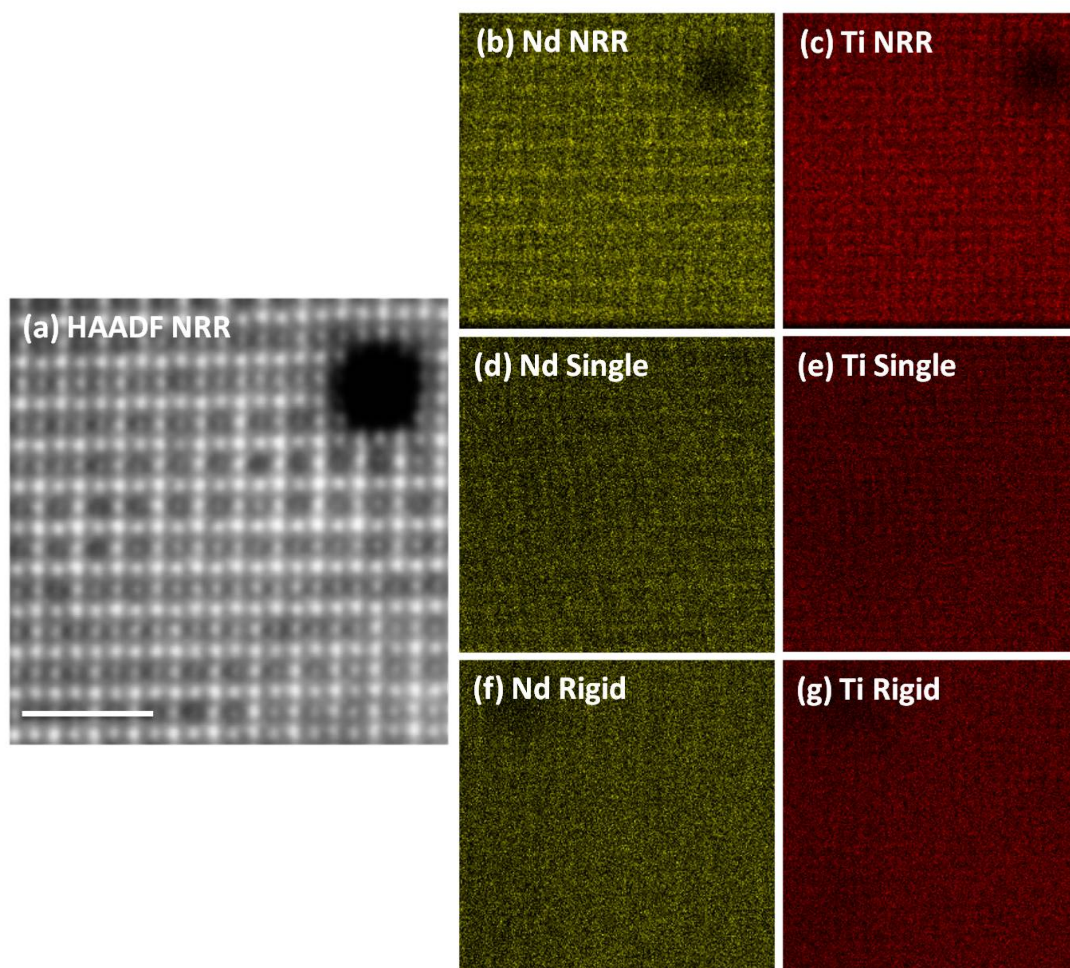

Figure 10.2: (a) NRR and averaged HAADF STEM image of $Nd_{2/3}TiO_3$. (b)-(g) EDS elemental maps using the Nd Lα peak (b)(d)(f) and the Ti Kα peak (c)(e)(g). (b)&(c) Maps from a sum of 98 SIs after NRR. (d)&(e) Maps from a single long exposure SI. (f)&(g) Maps from a sum of 100 drift-corrected SIs. The total counts in each of the 3 SI methods are approximately constant. No images have been smoothed. Scale bar in (a) is 2.5 nm.

Figure 10.2 shows the (a) NRR and averaged HAADF STEM image, as well as the extracted Nd Lα (b, d, f) and Ti Kα (c, e, g) elemental maps using each of the three spectrum image methods. (b) and (c) are elemental maps from the NRR and summed

spectrum image. (d) and (e) are elemental maps from the single long dwell time spectrum image. (f) and (g) are elemental maps from the sum of 100 drift-corrected spectrum images. The HAADF STEM image in (a) shows much higher SNR than the EDS elemental maps in (b) – (g), highlighting the benefit of calculating the NRR pixel distortions from the HAADF image series instead of the EDS spectrum image series. The extracted maps from the single long dwell time spectrum image in Figures 10.2 (d) and (e) show large image distortions from sample drift and other instabilities compared to the extracted maps from the NRR and summed spectrum image. The extracted maps from the sum of 100 drift-corrected spectrum images in Figures 10.2 (f) and (g) show much less image distortions compared to the single long dwell time spectrum image because they have been rigidly registered during acquisition. However, the elemental maps from both the single long dwell time spectrum image and the sum of 100 drift-corrected spectrum images show much lower resolution compared to the NRR and summed spectrum image elemental maps. This can be attributed to the NRR moving intensity that came from an atom column back to that atom column despite being moved away from it in the original image due to instabilities. Figure 10.2 shows that NRR and summing spectrum images achieves much less image distortion (enhancing image precision) and much better atomic column contrast and resolution compared to the other two common EDS spectrum image techniques.

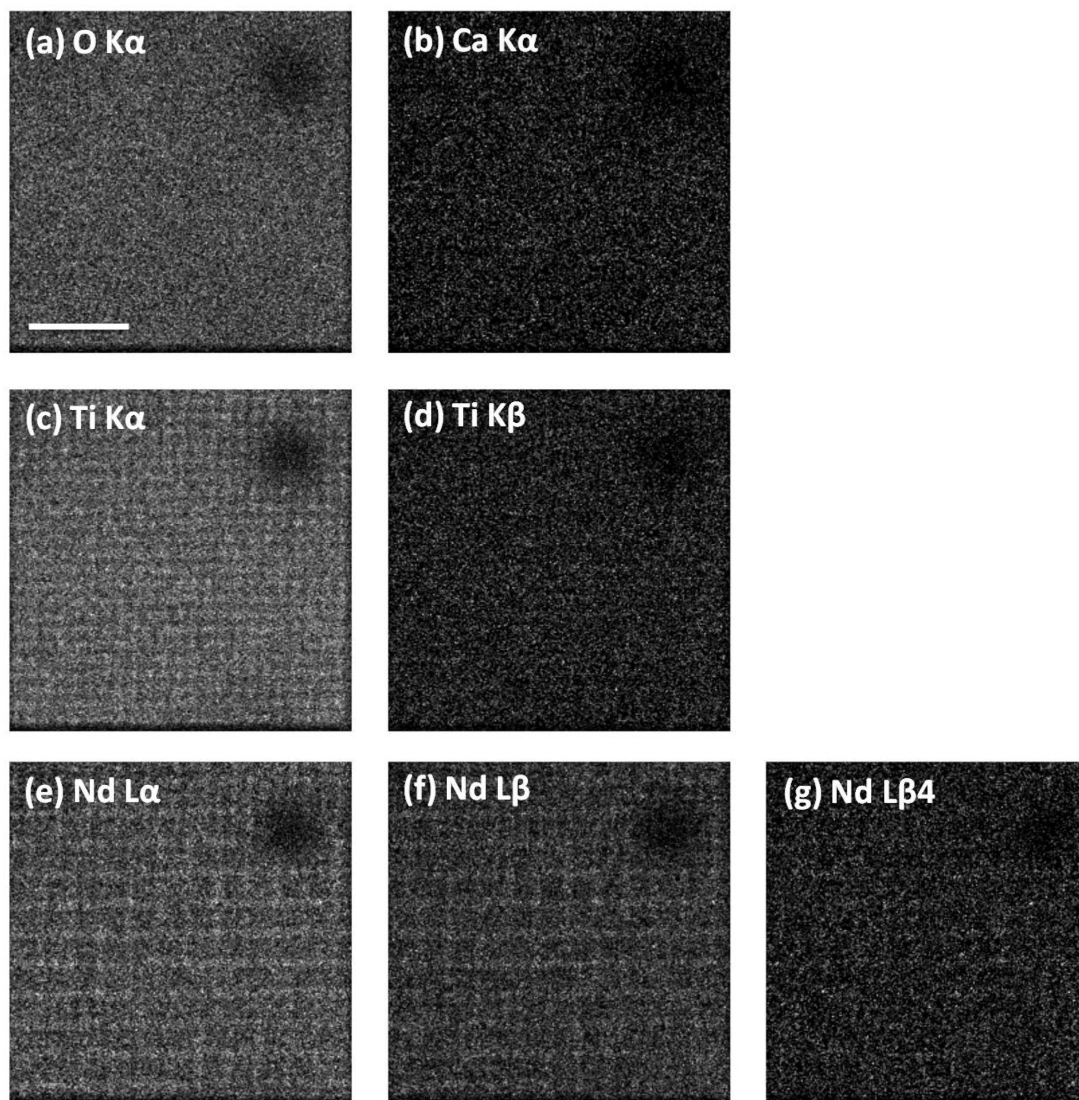

Figure 10.3: Extracted EDS elemental maps using the (a) O Kα peak, (b) Ca Kα peak, (c) Ti Kα peak, (d) Ti Kβ peak, (e) Nd Lα peak, (f) Nd Lβ peak, and (g) Nd Lβ4 peak from the NRR and summed spectrum image. Scale bar in (a) is 2.5 nm.

Figure 10.3 shows (a) O Kα peak, (b) Ca Kα peak, (c) Ti Kα peak, (d) Ti Kβ peak, (e) Nd Lα peak, (f) Nd Lβ peak, and (g) Nd Lβ4 peak elemental maps extracted from the NRR and summed spectrum image. The high intensity peaks in Figure 10.1(a)

signify high signal and therefore correspond to the elemental maps in Figure 10.3 that show good atomic resolution (c, e, and f). The O and Ca elemental maps show no clear atomic localization. The smaller Ti (d) and Nd (g) peaks show some localization, but much less than the larger peak elements of (c), (e), and (f).

NRR of STEM EDS spectrum images is possible and it improves the STEM EDS spectrum image data quality. This may enable future experiments of dopant point defects, such as those from Fe(*264*) or Nb doping(*265*, *266*) in STO. Single atom EDS has not yet been achieved, but with the possibility of enhancing the chemical SNR in spectrum images using NRR and making faint chemical signals more visible, single atom EDS might be possible. In addition, the enhanced spatial precision from NRR of simultaneous HAADF STEM images could allow precise measurements of the point defect atomic structures. The combination of these two capabilities in one experiment has potential to give unique insights into point defect structures and may help link their structure – property relationships. These capabilities could also be beneficial in determining the atomic structure and chemistry at materials interfaces and surfaces.

10.4. Conclusions

An EDS spectrum image series of Ca-doped $Nd_{2/3}TiO_3$ was NRR by using the pixel distortions calculated from the NRR of a simultaneously acquired HAADF STEM image series. The spectrum image quality was improved by using NRR compared to two other common EDS spectrum image acquisition techniques that used a similar electron doses: 1) a single long dwell time spectrum image and 2) a sum of inline drift-corrected

spectrum image series. The NRR of EDS spectrum image produces extracted elemental maps that are free of the distortions present in the other two methods, and show improved atom column contrast and resolution. In the future, this technique may enable the detection of weak chemical signals, such as interstitial or substitutional dopant atoms, simultaneously with the high precision HAADF STEM image that can be used to measure the local strain around the point defect. It will also be useful for determining the atomic structure and chemistry at materials interfaces and surfaces.

Appendix 1: Wedge Polishing Manual

1. Cleave/Cut sample into 2 pieces of a desired size.
2. Clean with ethanol/acetone and rinse with methanol.
3. Epoxy together using 1(dark)-8(light) ratio of Allied High Tech Epoxy Bond 110. Clamp together and heat (100C) until epoxy has set.
4. Cut piece to desired TEM sample size using wire saw. Use black wax to secure piece to black bar. (Heat is needed). Cut pieces. Remove black wax with TCE bath. Rinse with ethanol/acetone and methanol 3 times after TCE bath without letting the acetone dry.
5. Mount sample to metal stage using CrystalBond (Heat is needed). Use as little as possible.
6. Align Polisher to 0 degree tilt. Make sure main plate is inserted to the flattest position. For UW-Madison polisher, make sure the platen plate mounting alignment is such that the hole on the bottom of the platen marked with a "Z" fits into the peg on the polisher marked with a triangle. This alignment makes the platen as flat as possible. Make sure head can rotate freely by removing pin. Set weight to full. Put metal plate (PPF) on. Tape micrometer to platen using double stick tape. Lower polish head until 100 pressure. Rotate head fully using full rotate mode and change tilt until pressure is constant at 100. Put pin back in 3rd hole to lock rotation.

7. Polish sample side 1:

Thin to (um)	Diamond Paper	RPM	Notes
1000	30	100	
700	15	100	
650	6	75	
600	3	50	
Remove 10	1	50	
Remove 3 to 5	0.5	30	green lube
Remove 1	0.1	30	green lube
until no scratches	0.02 (red felt)	50	blue colloidal/last 30 seconds use water

8. Without removing sample from water, use micro-organic soap on Q-tip to wipe sample 4 times.
9. Remove sample from metal stage. Heat metal stage until the CrystalBond melts.
10. Polish glass stage completely flat with the same polishing head alignment as previously used and place sample on glass stage. Apply very thin layer of super glue to glass stage. Flip sample and mount to glass stage trying not to overhang sample but keeping it very close to the flat edge. Press on sample with toothpick to remove air bubbles.
11. Put sample in desiccator overnight to set and remove air.
12. Polish sample to 750 um on 30 um paper at 100 rpm.

13. Align tilt degree for polishing head. Planarize head. 2 degree = 2.5 rotations clockwise. Set rotation clockwise.
14. Polish sample side 2:

Thin to (um)	Diamond Paper	RPM	Notes
250	15	100	
150	6	75	
60	3	50	
	1	50	until edges are red for silicon, check every 10 um
	0.5	30	green lube
	0.1	30	green lube/ until edges are orange for Si and fringes are visible
	0.02 (red felt)	30-50	blue colloidal/ last 30 seconds use water

15. Without removing sample from water, use micro-organic soap on Q-tip to wipe sample 4 times.
16. Remove sample from stage. Put filter paper in beaker to fit beaker. Fill beaker with acetone. Put stage and sample in beaker and wait till sample falls off.
17. Soak tweezer and new scope stage in 409 orange cleaner to remove oils.
18. Use M-bond to attach sample to new stage. Let M-bond dry for 10 minutes and then heat it for 30 minutes to set M-bond and make it conductive.
19. Label and record sample.

Appendix 2: NRR and Quantitative STEM Manual

These procedures were created for the FEI Titan STEM instrument at the UW-Madison Materials Science Center.

Experimental Quantitative STEM Manual

1) In STEM mode, conduct a normal high-resolution alignment using the probe corrector on a standard gold sample. Alignment should be done with spot size 8 and a 70 μm C2 aperture. The aberration corrector should be sufficiently tuned to achieve 0.8 Angstrom resolution.
2) To achieve the best precision results, the sample of interest must be thin (<15 nm), free from amorphous surface material, and sufficiently clean from hydrocarbon surface contamination so that contamination build does not occur under STEM beam illumination. If needed, the sample should be plasma cleaned and/or annealed at a low temperature (~100 °C) in a vacuum oven sample-cleaning chamber to remove hydrocarbon surface material.
3) Once the microscope is tuned for high-resolution STEM, insert the sample of interest, find the area of interest, tilt very precisely to the correct crystal zone axis, and fine-tune the focus, sample height, and stigmators to achieve a good atomic resolution image.
4) Next it is time to set up the quantitative intensity scale. This intensity scale can be used to compare the experimental STEM image intensity to simulated image intensities to allow for quantitative analysis of the STEM image intensity. Move

to an area of the sample that has no sample so you are looking at vacuum. With the beam blanked, acquire a continuous HAADF STEM search image at around 5 Mx magnification. Under the "STEM imaging" panel, choose to view the "scope". Set the "brightness" in the "STEM Detector" panel so the intensity on the scope is positioned about 1/3 of the way up the possible scope range. Now steer the electron probe to the middle of the HAADF STEM detector. Set the "contrast" in the "STEM Detector" panel so the intensity on the scope is positioned about 2/3 of the way up the possible scope range. Once the brightness and contrast have been set to use the middle 1/3 of the scope's intensity (this may take a few iterations), acquire and save a HAADF STEM image with the beam blanked and with the full probe on the HAADF STEM detector. These images document the HAADF image intensity of the full electron probe and of zero electron probe. From this point on in your experiment, do not change the brightness or contrast settings and do not press the auto C/B button.

5) Next you want to take an image of electron probe using the GIF CCD camera. The gain of the GIF is known (## electrons/count) and this will allow you to put your HAADF STEM images on an absolute intensity scale of # of collected electrons. Switch the microscope to EFTEM mode and in Digital Micrograph use the EF-CCD camera to view the electron probe. You may need to change the camera length to ensure the whole electron probe is in the CCD field of view. Remove the HAADF detector and make sure no sample is in the way of the electron probe. Acquire an image with the GIF CCD using a frame time of about

15-20 seconds.

6) IGOR code in the precision measurements procedure will automatically put your HAADF STEM images on an absolute intensity scale using the information in the images you just acquired.

Experimental NRR STEM Series Acquisition Manual

1) Once the HRSTEM alignment is complete, the absolute intensity scale has been set up (optional), the area of interest on your sample is found, and the sample is tilted to the correct zone axis, you can acquire STEM image series for NRR. NRR works best when sample drift is small. This may require letting the microscope sit with your sample inserted and the area of interest found for a couple of hours.
2) You acquire the STEM image series using the preview acquisition mode. In the preview acquisition options flap-out menu you can change the number of images in the series, the pixel dwell time, and the number of pixel in each image. A good starting point for these parameters is 512 images, 10 μs/pixel, and 256 by 256 pixels.
3) After these settings are set, and you do your last minute focus and stigmator adjustments, click preview and the image series will start acquiring.
4) You can acquire simultaneous HAADF and ABF using this method if the ABF detector is inserted and set up properly. Note: simultaneous HAADF and ABF results in an image series where every two image in the series are the same. So if

a 512 image series is acquired, you will only end up with 256 unique frames.

5) In the upper menu bar there is an option to view the series slider. I recommend viewing the slider during acquisition so you know how far along the series acquisition is. You have to manually turn of the preview acquisition by clicking the preview button when you have acquired all the images you want. If you do not manually stop the preview acquisition, after the acquisition has reached the total number of images you want, more images will continue to be acquired but the images at the start of the series will be erased to maintain the total number of frames you want.

NRR Procedure

1) Once image series are acquired in TIA they can be post-processed. It is a good idea to preprocess the series using the IGOR functions in the "Stack Preprocess" IGOR procedure to remove duplicate frames and frames that have extremely large distortions.
2) Load the .ser file that contains the image series into IGOR using the SER file loader.
3) Use the "FrameDifference" and DeleteDupes" functions to delete the duplicate frames. This needs to be done if you acquired simultaneous HAADF and ABF images.
4) Use the "OneFramePS", "StackWindowPS", and "DeletelowPS" functions to delete the frames that have large distortions.

5) To save the series in the correct format for NRR, you will need the "IMI Double Precision File Loader" procedure compiled in IGOR. In the data / save waves menu choose "Save series to IMI files". This will save the entire series to .DAT files which are used as inputs for the NRR algorithm.
6) Put all of these .DAT files into a new folder and copy a version of the "matchSeries_paramters" file into this folder. Open the parameter file and change any of the parameters you see fit.
7) Using Win SCP or equivalent software, transfer the whole folder onto the ODIE compute cluster or the CONDOR head node.
8) Using SecureCRT or an equivalent software, access the directory you just transferred that has all the .DAT files and the parameter file. To run the NRR algorithm, the matchSeries code needs to be complied and you need access to it in your bin. There are detailed instructions in the "read me" file that comes with the quacmesh/matchSeries/NRR code.
9) Run the NRR with the command "~/bin/matchSeries matchSeries_paramters". The first half of the command is the link to the matchSeries executable. The second half of this command is the name of the parameter file. It is a good idea not to run this on the ODIE head node or the CONDOR submit node. Learn how to submit a job to run the NRR code.
10) The final images you want are in the results/ stage3 folder that is created by matchSeries. The images you want are the WinRAR files, which are compressed double precision .DAT images of the results. Once they are uncompressed, you

can open these up in IGOR using the functions in the “IMI Double Precision File Loader” procedure.

11) To have the NRR output the aligned image series, you need to rerun the matchSeries code a second time using the command “~/bin/matchSeries matchSeries_paramters 2”. The 2 in the command tells the code to run in a different mode that calculates and outputs the deformed images. They are outputed with names “defTempl_”.

IGOR Analysis of Atomic Column Positions

1) Open the image in IGOR and compile the “precision measurements” procedure.
2) Put the image on an absolute intensity scale if needed for your analysis. Use functions “AbsoluteIntensity” or “CountstoElectrons”, depending on what you need.
3) Crop the image to only use the area that used all the images in the series in the average. This part of the image will have the same signal to noise ratio. You can use the “cropimage” function, or if you have the “numSamples” image, you can use the “NumSamplesCrop” function which automatically finds the correct image area and crop it.
4) To automatically find initial guesses for the atom column positions, use the functions “PeakPositions” or “SegmentedPeakPositions”. “PeakPositions” will try to find all the peak position at one time. This works well if you have a well behaved image, but if there are large thickness variations across the image or

areas of the image with different materials this function will fail. Instead, use the "SegmentedPeakPositions" function which analyzes smaller regions of the image to more accurately find all the atom columns in the image.

5) Next use the "GaussianFit" function to fit each atomic column that was found by the "PeakPosition" functions. There are other functions in the procedure that have been created for fitting different types of images, such as dumbbells and ABF images. The x,y fit position coordinates of each atomic column can be found in the waves "x0" and "y0".
6) The IGOIR procedure has more detailed instructions on how to use each function and describes their inputs and outputs.

References:

1. A. B. Yankovich *et al.*, Stable p-type conduction from Sb-decorated head-to-head basal plane inversion domain boundaries in ZnO nanowires., *Nano Lett.* **12**, 1311–6 (2012).

2. A. B. Yankovich *et al.*, Absence of Lateral Composition Fluctuations in Aberration-corrected STEM Images of an InGaN Quantum Well at Low Dose, *MRS Proc.* **1432**, mrss12–1432–g04–03 (2012).

3. P. M. Voyles, D. a Muller, J. L. Grazul, P. H. Citrin, H.-J. L. Gossmann, Atomic-scale imaging of individual dopant atoms and clusters in highly n-type bulk Si., *Nature* **416**, 826–9 (2002).

4. A. V. Crewe, J. Wall, J. Langmore, Visibility of single atoms, *Science (80-.).* **168**, 1338–1340 (1970).

5. L. D. Marks, Experimental studies of small particle structures, *Reports Prog. Phys.* **57**, 603–649 (1994).

6. J. J. Liu, Advanced Electron Microscopy of Metal-Support Interactions in Supported Metal Catalysts, *ChemCatChem* **3**, 934–948 (2011).

7. P. D. Nellist, S. J. Pennycook, Direct imaging of the atomic configuration of ultradispersed catalysts, *Science (80-.).* **274**, 413–415 (1996).

8. M. M. J. Treacy, Pt agglomeration and entombment in single channel zeolites: Pt/LTL, *Microporous Mesoporous Mater.* **28**, 271–292 (1999).

9. D. J. Smith, Development of aberration-corrected electron microscopy, *Microsc. Microanal.* **14**, 2–15 (2008).

10. C. J. D. Hetherington *et al.*, High-resolution TEM and the application of direct and indirect aberration correction., *Microsc. Microanal.* **14**, 60–7 (2008).

11. O. L. Krivanek, N. Dellby, A. R. Lupini, Towards sub-Å electron beams, *Ultramicroscopy* **78**, 1–11 (1999).

12. A. Bleloch, A. Lupini, Imaging at the picoscale, *Mater. Today* , 42–48 (2004).

13. H. Müller, S. Uhlemann, P. Hartel, M. Haider, Advancing the Hexapole Cs-Corrector for the Scanning Transmission Electron Microscope, *Microsc. Microanal.* **12**, 442–455 (2006).

14. M. Haider, S. Uhlemann, E. Schwan, Electron microscopy image enhanced, *Nature* **392**, 768–769 (1998).

15. D. Alloyeau, B. Freitag, S. Dag, L. Wang, C. Kisielowski, Atomic-resolution three-dimensional imaging of germanium self-interstitials near a surface: Aberration-corrected transmission electron microscopy, *Phys. Rev. B* **80**, 1–6 (2009).

16. A. a Gunawan, K. A. Mkhoyan, A. W. Wills, M. G. Thomas, D. J. Norris, Imaging "invisible" dopant atoms in semiconductor nanocrystals., *Nano Lett.* **11**, 5553–7 (2011).

17. R. Erni, M. Rossell, C. Kisielowski, U. Dahmen, Atomic-Resolution Imaging with a Sub-50-pm Electron Probe, *Phys. Rev. Lett.* **102**, 096101 (2009).

18. S. J. Pennycook, P. D. Nellist, Eds., *Scanning Transmission Electron Microscopy: Imaging and Analysis* (Springer, 2011).

19. J. M. LeBeau, S. D. Findlay, L. J. Allen, S. Stemmer, Standardless atom counting in scanning transmission electron microscopy, *Nano Lett.* **10**, 4405–4408 (2010).

20. M. De Graef, *Introduction to Conventional Transmission Electron Microscopy* (Cambridge, 2003).

21. D. B. Williams, C. B. Carter, *Transmission Electron Microscopy*.

22. A. K. Petford-Long, A. N. Chiaramonti, Transmission Electron Microscopy of Multilayer Thin Films*, *Annu. Rev. Mater. Res.* **38**, 559–584 (2008).

23. P. L. Gai, J. J. Calvino, Electron Microscopy in the Catalysis of Alkane Oxidation, Environmental Control, and Alternative Energy Sources, *Annu. Rev. Mater. Res.* **35**, 465–504 (2005).

24. R. Tenne, G. Seifert, Recent Progress in the Study of Inorganic Nanotubes and Fullerene-Like Structures, *Annu. Rev. Mater. Res.* **39**, 387–413 (2009).

25. K. Sato, T. J. Konno, Y. Hirotsu, Atomic structure imaging of L1[sub 0]-type FePd nanoparticles by spherical aberration corrected high-resolution transmission electron microscopy, *J. Appl. Phys.* **105**, 1–5 (2009).

26. M. Lentzen *et al.*, High-resolution imaging with an aberration-corrected transmission electron microscope., *Ultramicroscopy* **92**, 233–242 (2002).

27. M. Varela *et al.*, Materials Characterization in the Aberration-Corrected Scanning Transmission Electron Microscope, *Annu. Rev. Mater. Res.* **35**, 539–569 (2005).

28. a Chuvilin, U. Kaiser, On the peculiarities of CBED pattern formation revealed by multislice simulation., *Ultramicroscopy* **104**, 73–82 (2005).

29. S. J. Pennycook, Z-Contrast Transmission Electron Microscopy: Direct Atomic Imaging of Materials, *Annu. Rev. Mater. Sci.* **22**, 171–195 (1992).

30. P. Hartel, H. Rose, C. Dinges, Conditions and reasons for incoherent imaging in STEM, *Ultramicroscopy* **63**, 93–114 (1996).

31. S. Hillyard, R. F. Loane, J. Silcox, Annular dark-field imaging: resolution and thickness effects, *Ultramicroscopy* **49**, 14–25 (1993).

32. D. D. Perovic, C. J. Rossouw, A. Howie, Imaging elastic strains in high-angle annular dark field scanning transmission electon microscopy, *Ultramicroscopy* **52**, 353–359 (1993).

33. S. D. Findlay *et al.*, Robust atomic resolution imaging of light elements using scanning transmission electron microscopy, *Appl. Phys. Lett.* **95**, 1–3 (2009).

34. E. Okunishi *et al.*, Visualization of Light Elements at Ultrahigh Resolution by STEM Annular Bright Field Microscopy, *Microsc. Microanal.* **15**, 164 (2009).

35. S. D. Findlay *et al.*, Dynamics of annular bright field imaging in scanning transmission electron microscopy., *Ultramicroscopy* **110**, 903–23 (2010).

36. S. D. Findlay *et al.*, Direct Imaging of Hydrogen within a Crystalline Environment, *Appl. Phys. Express* **3**, 116603 (2010).

37. S. D. Findlay *et al.*, Annular Bright Field Scanning Transmission Electron Microscopy Imaging Dynamics, *Microsc. Microanal.* **16**, 80–81 (2010).

38. P. W. Hawkes, E. Kasper, *Principles of electron optics* (Academic Press, London, 1994).

39. P. W. Hawkes, Aberration correction past and present., *Philos. Trans. A. Math. Phys. Eng. Sci.* **367**, 3637–64 (2009).

40. J. LeBeau, S. Findlay, L. Allen, S. Stemmer, Quantitative Atomic Resolution Scanning Transmission Electron Microscopy, *Phys. Rev. Lett.* **100**, 1–4 (2008).

41. J. M. LeBeau, S. Stemmer, Experimental quantification of annular dark-field images in scanning transmission electron microscopy, *Ultramicroscopy* **108**, 1653–1658 (2008).

42. R. Ishikawa, A. R. Lupini, S. D. Findlay, S. J. Pennycook, Quantitative Annular Dark Field Electron Microscopy Using Single Electron Signals, *Microsc. Microanal.* **20**, 99–110 (2014).

43. S. D. Findlay, J. M. LeBeau, Detector non-uniformity in scanning transmission electron microscopy., *Ultramicroscopy* **124**, 52–60 (2013).

44. K. E. MacArthur, L. B. Jones, P. D. Nellist, How flat is your detector? Non-uniform annular detector sensitivity in STEM quantification, *J. Phys. Conf. Ser.* **522**, 012018 (2014).

45. T. Mehrtens *et al.*, Measurement of the indium concentration in high indium content InGaN layers by scanning transmission electron microscopy and atom probe tomography, *Appl. Phys. Lett.* **102**, 132112 (2013).

46. H. Sawada, M. Watanabe, I. Chiyo, Ad hoc auto-tuning of aberrations using high-resolution STEM images by autocorrelation function, *Microsc. Microanal.* **18**, 705–710 (2012).

47. C. Dwyer, R. Erni, J. Etheridge, Measurement of effective source distribution and its importance for quantitative interpretation of STEM images, *Ultramicroscopy* **110**, 952–957 (2010).

48. J. LeBeau *et al.*, High-angle scattering of fast electrons from crystals containing heavy elements: Simulation and experiment, *Phys. Rev. B* **79**, 1–6 (2009).

49. J. M. LeBeau, S. D. Findlay, L. J. Allen, S. Stemmer, Position averaged convergent beam electron diffraction: theory and applications, *Ultramicroscopy* **110**, 118–25 (2010).

50. T. Malis, S. Cheng, R. Egerton, EELS Log-Ratio Technique for Specimen-Thickness Measurment in the TEM, *J. Electron Microsc. Tech.* **8**, 193–200 (1988).

51. R. F. Egerton, *Electron Energy-loss Spectroscopy in the Electron Microscope, 2nd Edition* (Springer, 1996).

52. J. M. Zuo, J. C. H. Spence, Automated structure factor refinement from convergent-beam patterns, *Ultramicroscopy* **35**, 185–196 (1991).

53. J. M. LeBeau, A. J. D'Alfonso, N. J. Wright, L. J. Allen, S. Stemmer, Determining ferroelectric polarity at the nanoscale, *Appl. Phys. Lett.* **98**, 052904 (2011).

54. J. Hwang, J. Y. Zhang, J. Son, S. Stemmer, Nanoscale quantification of octahedral tilts in perovskite films, *Appl. Phys. Lett.* **100**, 191909 (2012).

55. E. J. Kirkland, *Advanced Computing in Electron Microscopy, 1st Edition* (Springer, 1998).

56. D. a Muller, B. Edwards, E. J. Kirkland, J. Silcox, Simulation of thermal diffuse scattering including a detailed phonon dispersion curve., *Ultramicroscopy* **86**, 371–80 (2001).

57. W. Sigle, Analytical Transmission Electron Microscopy, *Annu. Rev. Mater. Res.* **35**, 239–314 (2005).

58. M.-W. Chu, S. C. Liou, C.-P. Chang, F.-S. Choa, C. H. Chen, Emergent Chemical Mapping at Atomic-Column Resolution by Energy-Dispersive X-Ray Spectroscopy in an Aberration-Corrected Electron Microscope, *Phys. Rev. Lett.* **104**, 1–4 (2010).

59. L. Gunawan *et al.*, Locating La atoms in epitaxial Bi[sub 3.25]La[sub 0.75]Ti[sub 3]O[sub 12] films through atomic resolution electron energy loss spectroscopy mapping, *Appl. Phys. Lett.* **95**, 192902 (2009).

60. O. L. Krivanek *et al.*, Vibrational spectroscopy in the electron microscope, *Nature* **514**, 209–212 (2014).

61. Z.-Z. Li, Z.-Z. Chen, W. Huang, S.-H. Chang, X.-M. Ma, The transparence comparison of Ga- and Al-doped ZnO thin films, *Appl. Surf. Sci.* **257**, 8486–8489 (2011).

62. H. Liu, V. Avrutin, N. Izyumskaya, Ü. Özgür, H. Morkoç, Transparent conducting oxides for electrode applications in light emitting and absorbing devices, *Superlattices Microstruct.* **48**, 458–484 (2010).

63. U. Ozgur, D. Hofstetter, H. Morkoc, ZnO Devices and Applications : A Review of Current Status and Future Prospects, *Proc. IEEE* **98**, 1255 (2010).

64. S. J. Pearton, D. P. Norton, K. Ip, Y. W. Heo, T. Steiner, Recent advances in processing of ZnO, *J. Vac. Sci. Technol. B* **22**, 932 (2004).

65. T. Minami, Present status of transparent conducting oxide thin-film development for Indium-Tin-Oxide (ITO) substitutes, *Thin Solid Films* **516**, 5822–5828 (2008).

66. J. a. Sans, G. Martínez-Criado, J. Pellicer-Porres, J. F. Sánchez-Royo, a. Segura, Thermal instability of electrically active centers in heavily Ga-doped ZnO thin films: X-ray absorption study of the Ga-site configuration, *Appl. Phys. Lett.* **91**, 221904 (2007).

67. a. Ougazzaden *et al.*, Growth of GaN by metal organic vapor phase epitaxy on ZnO-buffered c-sapphire substrates, *J. Cryst. Growth* **310**, 944–947 (2008).

68. a. V. Kvit *et al.*, Impurity distribution and microstructure of Ga-doped ZnO films grown by molecular beam epitaxy, *J. Appl. Phys.* **112**, 123527 (2012).

69. S.-K. Hong *et al.*, Control of crystal polarity in a wurtzite crystal: ZnO films grown by plasma-assisted molecular-beam epitaxy on GaN, *Phys. Rev. B* **65**, 115331 (2002).

70. a. R. Smith *et al.*, Determination of wurtzite GaN lattice polarity based on surface reconstruction, *Appl. Phys. Lett.* **72**, 2114 (1998).

71. D. Kohl, M. Henzler, G. Heiland, Low Temperature Sublimation Processes From Clean Cleaved Polar Surfaces of Zinc Oxide Crystals During First Heating, *Surf. Sci.* **41**, 403–411 (1974).

72. D. C. Look, D. C. Reynolds, J. W. Hemsky, R. L. Jones, J. R. Sizelove, Production and annealing of electron irradiation damage in ZnO, *Appl. Phys. Lett.* **75**, 811 (1999).

73. H. Y. Liu *et al.*, Highly conductive and optically transparent GZO films grown under metal-rich conditions by plasma assisted MBE, *Phys. status solidi - Rapid Res. Lett.* **4**, 70–72 (2010).

74. H. Y. Liu *et al.*, InGaN based light emitting diodes utilizing Ga doped ZnO as a highly transparent contact to p-GaN, *Phys. Status Solidi* **8**, 1548–1551 (2011).

75. H. Y. Liu *et al.*, No Title, *Proc. SPIE* **7939**, 79392E (2011).

76. H. Y. Liu *et al.*, No Title, *Proc. SPIE* **8262**, 826226 (2012).

77. a. B. Yankovich *et al.*, Hexagonal-based pyramid void defects in GaN and InGaN, *J. Appl. Phys.* **111**, 023517 (2012).

78. S. D. Findlay *et al.*, Robust atomic resolution imaging of light elements using scanning transmission electron microscopy, *Appl. Phys. Lett.* **95**, 191913 (2009).

79. J. S. Reid, Debye-Waller Factors of Zinc-Blende-Structure Materials - A Lattice Dynamical Comparison, *Acta Crystallogr. Sect. A* **39**, 1–13 (1982).

80. S. Sakong, P. Kratzer, Density functional study of carbon doping in ZnO, *Semicond. Sci. Technol.* **26**, 014038 (2011).

81. Y. Izawa *et al.*, No Title, *AIP Conf. Proc.* **1399**, 69 (2011).

82. H. Y. Xu *et al.*, F-doping effects on electrical and optical properties of ZnO nanocrystalline films, *Appl. Phys. Lett.* **86**, 123107 (2005).

83. J. G. Liu *et al.*, The influences of O/Zn ratio and growth temperature on carbon impurity incorporation in ZnO grown by metal-organic chemical vapor deposition, *J. Cryst. Growth* **312**, 2710–2717 (2010).

84. Y. Chen *et al.*, Plasma assisted molecular beam epitaxy of ZnO on c -plane sapphire : Growth and characterization, *J. Appl. Phys.* **84**, 3912–3918 (1998).

85. D. C. Look, Progress in ZnO materials and devices, *J. Electron. Mater.* **35**, 1299–1305 (2006).

86. M. D. McCluskey, S. J. Jokela, Defects in ZnO, *J. Appl. Phys.* **106**, 071101 (2009).

87. S. C. Su, X. D. Yang, C. D. Hu, Structural, optical and electronic properties of P doped p-type ZnO thin film, *Phys. B* **406**, 1533–1535 (2011).

88. Y.-C. Cheng, Y.-S. Kuo, Y.-H. Li, J.-J. Shyue, M.-J. Chen, Stable p-type ZnO films grown by atomic layer deposition on GaAs substrates and treated by post-deposition rapid thermal annealing, *Thin Solid Films* **519**, 5558–5561 (2011).

89. J. C. Fan *et al.*, Comprehensive study of the p-type conductivity formation in radio frequency magnetron sputtered arsenic-doped ZnO film, *J. Vac. Sci. Technol. A Vacuum, Surfaces, Film.* **29**, 03A103 (2011).

90. M. J. Joseph, H. T. Tabata, T. K. Kawai, p-Type Electrical Conduction in ZnO Thin Films by Ga and N Codoping, *Jpn. J. Appl. Phys.* **38**, L1205–L1207 (1999).

91. J. G. Lu *et al.*, p-type conduction in N–Al co-doped ZnO thin films, *Appl. Phys. Lett.* **85**, 3134–3135 (2004).

92. L. L. Chen *et al.*, p-type behavior in In–N codoped ZnO thin films, *Appl. Phys. Lett.* **87**, 1–3 (2005).

93. T. P. Rao, M. C. S. Kumar, Realization of stable p-type ZnO thin films using Li–N dual acceptors, *J. Alloys Compd.* **509**, 8676–8682 (2011).

94. E. S. Kumar, J. Chatterjee, N. Rama, N. DasGupta, M. S. R. Rao, A codoping route to realize low resistive and stable p-type conduction in (Li, Ni):ZnO thin films grown by pulsed laser deposition., *ACS Appl. Mater. Interfaces* **3**, 1974–1979 (2011).

95. G. Wang, S. Chu, N. Zhan, H. Zhou, J. Liu, Synthesis and characterization of Ag-doped p-type ZnO nanowires, *Appl. Phys. A* **103**, 951–954 (2011).

96. M. K. Gupta, N. Sinha, B. Kumar, p-type K-doped ZnO nanorods for optoelectronic applications, *J. Appl. Phys.* **109**, 1–5 (2011).

97. B. Xiang *et al.*, Rational synthesis of p-type zinc oxide nanowire arrays using simple chemical vapor deposition., *Nano Lett.* **7**, 323–328 (2007).

98. M.-P. Lu *et al.*, Piezoelectric nanogenerator using p-type ZnO nanowire arrays., *Nano Lett.* **9**, 1223–1227 (2009).

99. T. Yamamoto, H. Katayama-Yoshida, Physics and control of valence states in ZnO by codoping method, *Phys. B Condens. Matter* **302-303**, 155–162 (2001).

100. A. Kohan, G. Ceder, D. Morgan, C. Van de Walle, First-principles study of native point defects in ZnO, *Phys. Rev. B* **61**, 15019–15027 (2000).

101. D. Look, J. Hemsky, J. Sizelove, Residual Native Shallow Donor in ZnO, *Phys. Rev. Lett.* **82**, 2552–2555 (1999).

102. S. C. Su, X. D. Yang, C. D. Hu, Structural, optical and electronic properties of P doped p-type ZnO thin film, *Phys. B Condens. Matter* **406**, 1533–1535 (2011).

103. Y.-C. Cheng, Y.-S. Kuo, Y.-H. Li, J.-J. Shyue, M.-J. Chen, Stable p-type ZnO films grown by atomic layer deposition on GaAs substrates and treated by post-deposition rapid thermal annealing, *Thin Solid Films* **519**, 5558–5561 (2011).

104. M. J. Joseph, H. T. Tabata, T. K. Kawai, p-Type Electrical Conduction in ZnO Thin Films by Ga and N Codoping, *Jpn. J. Appl. Phys.* **38**, 1205–1207 (1999).

105. J. G. Lu *et al.*, p-type conduction in N–Al co-doped ZnO thin films, *Appl. Phys. Lett.* **85**, 3134 (2004).

106. T. P. Rao, M. C. S. Kumar, Realization of stable p-type ZnO thin films using Li–N dual acceptors, *J. Alloys Compd.* **509**, 8676–8682 (2011).

107. E. S. Kumar, J. Chatterjee, N. Rama, N. DasGupta, M. S. R. Rao, A codoping route to realize low resistive and stable p-type conduction in (Li, Ni):ZnO thin films grown by pulsed laser deposition., *ACS Appl. Mater. Interfaces* **3**, 1974–9 (2011).

108. M. K. Gupta, N. Sinha, B. Kumar, p-type K-doped ZnO nanorods for optoelectronic applications, *J. Appl. Phys.* **109**, 083532 (2011).

109. B. Xiang *et al.*, Rational synthesis of p-type zinc oxide nanowire arrays using simple chemical vapor deposition., *Nano Lett.* **7**, 323–8 (2007).

110. M.-P. Lu *et al.*, Piezoelectric nanogenerator using p-type ZnO nanowire arrays., *Nano Lett.* **9**, 1223–7 (2009).

111. T. Aoki *et al.*, p-Type ZnO Layer Formation by Excimer Laser Doping, *Phys. Status Solidi* **229**, 911–914 (2002).

112. F. X. Xiu *et al.*, High-mobility Sb-doped p-type ZnO by molecular-beam epitaxy, *Appl. Phys. Lett.* **87**, 152101 (2005).

113. L. J. Mandalapu, Z. Yang, F. X. Xiu, D. T. Zhao, J. L. Liu, Homojunction photodiodes based on Sb-doped p-type ZnO for ultraviolet detection, *Appl. Phys. Lett.* **88**, 092103 (2006).

114. E. Przeździecka, E. Kamińska, I. Pasternak, a. Piotrowska, J. Kossut, Photoluminescence study of p-type ZnO:Sb prepared by thermal oxidation of the Zn-Sb starting material, *Phys. Rev. B* **76**, 10–13 (2007).

115. S. Chu *et al.*, Sb-doped p-ZnO∕Ga-doped n-ZnO homojunction ultraviolet light emitting diodes, *Appl. Phys. Lett.* **92**, 152103 (2008).

116. X. H. Pan *et al.*, Optical properties of antimony-doped p-type ZnO films fabricated by pulsed laser deposition, *J. Appl. Phys.* **105**, 113516 (2009).

117. F. Wang *et al.*, An aqueous solution-based doping strategy for large-scale synthesis of Sb-doped ZnO nanowires., *Nanotechnology* **22**, 225602 (2011).

118. G. Wang *et al.*, ZnO homojunction photodiodes based on Sb-doped p-type nanowire array and n-type film for ultraviolet detection, *Appl. Phys. Lett.* **98**, 1–3 (2011).

119. S. Chu *et al.*, Electrically pumped waveguide lasing from ZnO nanowires., *Nat. Nanotechnol.* **6**, 4–8 (2011).

120. U. Wahl *et al.*, Direct Evidence for As as a Zn-Site Impurity in ZnO, *Phys. Rev. Lett.* **95**, 1–4 (2005).

121. U. Wahl, J. G. Correia, S. Decoster, T. Mendonça, Lattice location of the group V elements As and Sb in ZnO, *Phys. B Condens. Matter* **404**, 4803–4806 (2009).

122. S. Limpijumnong, S. Zhang, S.-H. Wei, C. Park, Doping by Large-Size-Mismatched Impurities: The Microscopic Origin of Arsenic- or Antimony-Doped p-Type Zinc Oxide, *Phys. Rev. Lett.* **92**, 1–4 (2004).

123. B. Puchala, D. Morgan, Stable interstitial dopant - vacancy complexes in ZnO, *To be Publ.* , 1–4 (2011).

124. S. Limpijumnong, S. Zhang, S.-H. Wei, C. Park, Doping by Large-Size-Mismatched Impurities: The Microscopic Origin of Arsenic- or Antimony-Doped p-Type Zinc Oxide, *Phys. Rev. Lett.* **92**, 1–4 (2004).

125. B. Puchala, D. Morgan, Stable interstitial dopant–vacancy complexes in ZnO, *Phys. Rev. B* **85**, 195207 (2012).

126. J. Goldberger, D. J. Sirbuly, M. Law, P. Yang, ZnO nanowire transistors., *J. Phys. Chem. B* **109**, 9–14 (2005).

127. P. Hohenberg, W. Kohn, Inhomogeneous Electron Gas, *Phys. Rev.* **136**, 864–871 (1964).

128. G. Kresse, J. Hafner, Ab initio molecular dynamics for liquid metals, *Phys. Rev. B* **47**, 558–561 (1993).

129. G. Kresse, J. Hafner, Ab initio molecular-dynamics simulation of the liquid-metal-amorphous-semiconductor transition in germanium, *Phys. Rev. B* **49**, 14251 (1994).

130. G. Kresse, J. Furthmüller, Efficiency of ab-initio total energy calculations for metals and semiconductors using a plane-wave basis set, *Comput. Mater. Sci.* **6**, 15–50 (1996).

131. G. Kresse, J. Furthmüller, Efficient iterative schemes for ab initio total-energy calculations using a plane-wave basis set., *Phys. Rev. B* **54**, 11169–11186 (1996).

132. G. Kresse, D. Joubert, From ultrasoft pseudopotentials to the projector augmented-wave method, *Phys. Rev. B* **59**, 1758–1775 (1999).

133. J. P. Perdew, K. Burke, M. Ernzerhof, Generalized Gradient Approximation Made Simple., *Phys. Rev. Lett.* **77**, 3865–3868 (1996).

134. J. P. Perdew, K. Burke, M. Ernzerhof, Generalized Gradient Approximation Made Simple., *Phys. Rev. Lett.* **77**, 3865–3868 (1997).

135. V. I. Anisimov, F. Aryasetiawan, A. I. Lichtenstein, First-principles calculations of the electronic structure and spectra of strongly correlated systems : the LDA + U method, *J. Phys. Condens. Matter* **9**, 767–808 (1997).

136. P. Erhart, K. Albe, A. Klein, First-principles study of intrinsic point defects in ZnO: Role of band structure, volume relaxation, and finite-size effects, *Phys. Rev. B* **73**, 205203 (2006).

137. A. Rečnik, N. Daneu, T. Walther, W. Mader, Structure and Chemistry of Basal-Plane Inversion Boundaries in Antimony Oxide-Doped Zinc Oxide, *J. Am. Ceram. Soc.* **84**, 2657–2668 (2001).

138. M. Shiojiri *et al.*, High-Resolution HAADF STEM of Inversion Boundaries in Sb 2 O 3 -Doped Zinc Oxide, *America (NY).* **8**, 494–495 (2002).

139. T. Yamazaki *et al.*, Quantitative high-resolution HAADF-STEM analysis of inversion boundaries in Sb(2)O(3)-doped zinc oxide., *Ultramicroscopy* **98**, 305–16 (2004).

140. M. a. McCoy, R. W. Grimes, W. E. Lee, Inversion domain boundaries in ZnO ceramics, *J. Mater. Res.* **11**, 2009–2019 (2011).

141. M. Ruhle, M. Wilkens, Defocusing contrast of cavities I. theory, *Cryst. Lattice Defects* **6**, 129–140 (1975).

142. H. Schmid, E. Okunishi, T. Oikawa, W. Mader, Structural and elemental analysis of iron and indium doped zinc oxide by spectroscopic imaging in Cs-corrected STEM., *Micron* (2011), doi:10.1016/j.micron.2011.05.011.

143. W. Yu, W. Mader, Displacement field measurement of metal sub-lattice in inversion domains of indium-doped zinc oxide, *Ultramicroscopy* **110**, 411–417 (2010).

144. W. Jo, C. Park, D.-Y. Kim, Characterization of pyramidal inversion boundaries in Sb2O3-doped ZnO by using electron back-scattered diffraction (EBSD)., *Acta Crystallogr. A.* **63**, 229–33 (2007).

145. J. S. Park *et al.*, Growth of Polarity-Controlled ZnO Films on (0001) Al2O3, *J. Electron. Mater.* **37**, 736–742 (2007).

146. Q. H. Li, Q. Wan, Y. X. Liang, T. H. Wang, Electronic transport through individual ZnO nanowires, *Appl. Phys. Lett.* **84**, 4556 (2004).

147. C.-Y. Chen *et al.*, Surface effects on optical and electrical properties of ZnO nanostructures, *Pure Appl. Chem.* **82**, 2055–2073 (2010).

148. H. Y. Liu *et al.*, Donor behavior of Sb in ZnO, *J. Appl. Phys.* **112**, 033706 (2012).

149. S. Chu *et al.*, Electrically pumped waveguide lasing from ZnO nanowires., *Nat. Nanotechnol.* **6**, 506–510 (2011).

150. K. C. Pradel, W. Wu, Y. Ding, Z. L. Wang, Solution-derived ZnO homojunction nanowire films on wearable substrates for energy conversion and self-powered gesture recognition., *Nano Lett.* **14**, 6897–905 (2014).

151. X. Ren *et al.*, White Light-Emitting Diode From Sb-Doped p-ZnO Nanowire Arrays/n-GaN Film, *Adv. Funct. Mater.* **25**, 2182–2188 (2015).

152. S. Nakamura, M. Senoh, S. Nagahama, N. Iwasa, Room-temperature continuous-wave operation of InGaN multi-quantum-well-structure laser diodes with a long lifetime, *Appl. Phys. Lett.* **70**, 868–870 (1997).

153. S. J. Pearton, F. Ren, A. P. Zhang, K. P. Lee, Fabrication and performance of GaN electronic devices, *Mater. Sci. Eng.* **30**, 55–212 (2000).

154. H. Morkoç *et al.*, Large-band-gap SiC, III-V nitride, and II-VI ZnSe-based semiconductor device technologies, *J. Appl. Phys.* **76**, 1363 (1994).

155. S. Nakamura *et al.*, InGaN-Based Multi-Quantum-Well-Structure Laser Diodes, *Jpn. J. Appl. Phys.* **35**, L74–L76 (1996).

156. R. G. Powell, N. Lee, Y. Kim, J. E. Greene, Heteroepitaxial by reactlve-ion wurtzite and zinc-blende structure GaN grown molecular-beam epitaxy : Growth kinetics , and properties, *J. Appl. Phys.* **73**, 189–204 (1993).

157. J. Xie *et al.*, Low dislocation densities and long carrier lifetimes in GaN thin films grown on a SiN[sub x] nanonetwork, *Appl. Phys. Lett.* **90**, 041107 (2007).

158. Y. Narukawa *et al.*, Role of self-formed InGaN quantum dots for exciton localization in the purple laser diode emitting at 420 nm, *Appl. Phys. Lett.* **70**, 981 (1997).

159. R. Singh, D. Doppalapudi, T. D. Moustakas, L. T. Romano, Phase separation in InGaN thick films and formation of InGaN/GaN double heterostructures in the entire alloy composition, *Appl. Phys. Lett.* **70**, 1089 (1997).

160. N. a. El-Masry, E. L. Piner, S. X. Liu, S. M. Bedair, Phase separation in InGaN grown by metalorganic chemical vapor deposition, *Appl. Phys. Lett.* **72**, 40–42 (1998).

161. H. K. Cho *et al.*, Effect of growth interruptions on the light emission and indium clustering of InGaN/GaN multiple quantum wells, *Appl. Phys. Lett.* **79**, 2594 (2001).

162. I. Ho, G. B. Stringfellow, Solid phase immiscibility in GaInN, *Appl. Phys. Lett.* **69**, 2701 (1996).

163. A. Wakahara, T. Tokuda, X.-Z. Dang, S. Noda, A. Sasaki , Compositional inhomogeneity and immiscibility of a GaInN ternary alloy, *Appl. Phys. Lett.* **71**, 906 (1997).

164. N. Sharma, P. Thomas, D. Tricker, C. Humphreys, Chemical mapping and formation of V-defects in InGaN multiple quantum wells, *Appl. Phys. Lett.* **77**, 1274 (2000).

165. T. P. Bartel, P. Specht, J. C. Ho, C. Kisielowski, Phase separation in In x Ga 1− x N, *Philos. Mag.* **87**, 1983–1998 (2007).

166. T. M. Smeeton, M. J. Kappers, J. S. Barnard, M. E. Vickers, C. J. Humphreys, Electron-beam-induced strain within InGaN quantum wells: False indium “cluster” detection in the transmission electron microscope, *Appl. Phys. Lett.* **83**, 5419 (2003).

167. R. A. Oliver, M. J. Galtrey, C. J. Humphreys, High resolution transmission electron microscopy and three-dimensional atom probe microscopy as complementary techniques for the high spatial resolution analysis of GaN based quantum well systems, *Mater. Sci. Technol.* **24**, 675–681 (2008).

168. X. Li *et al.*, InGaN based light emitting diodes with Ga doped ZnO as transparent conducting oxide, *Phys. Status Solidi* **207**, 1993–1996 (2010).

169. P. M. Voyles, J. L. Grazul, D. a Muller, Imaging individual atoms inside crystals with ADF-STEM., *Ultramicroscopy* **96**, 251–73 (2003).

170. L. A. Giannuzzi, F. A. Stevie, *Introduction to Focused Ion Beams: Instrumentation, Theory, Techniques and Practice* (2005), pp. 213–214.

171. X. Xiong, S. C. Moss, X-ray studies of defects and thermal vibrations in an organometallic vapor phase epitaxy grown GaN thin film, *J. Appl. Phys.* **82**, 2308 (1997).

172. K. Iakoubovskii, K. Mitsuishi, Y. Nakayama, K. Furuya, Thickness measurements with electron energy loss spectroscopy., *Microsc. Res. Tech.* **71**, 626–31 (2008).

173. X. H. Wu *et al.*, Structural origin of V-defects and correlation with localized excitonic centers in InGaN/GaN multiple quantum wells, *Appl. Phys. Lett.* **72**, 692 (1998).

174. Y. Chen *et al.*, Pit formation in GaInN quantum wells, *Appl. Phys. Lett.* **72**, 710 (1998).

175. I.-H. Kim, H.-S. Park, Y.-J. Park, T. Kim, Formation of V-shaped pits in InGaN/GaN multiquantum wells and bulk InGaN films, *Appl. Phys. Lett.* **73**, 1634 (1998).

176. J. Off *et al.*, Investigations on the V-defect formation in GaInN-GaN multi quantum well structures, *Phys. Status Solidi* **216**, 529 (1999).

177. K. Watanabe *et al.*, Formation and structure of inverted hexagonal pyramid defects in multiple quantum wells InGaN/GaN, *Appl. Phys. Lett.* **82**, 718 (2003).

178. A. Sanchez *et al.*, V-defects and dislocations in InGaN/GaN heterostructures, *Thin Solid Films* **479**, 316–320 (2005).

179. W. Qian, M. Skowronski, M. De Graef, Microstructural characterization of GaN films grown on sapphire by organometallic vapor phase epitaxy, *Appl. Phys. Lett.* **66**, 1252–1254 (1995).

180. P. Vennegues, B. Beaumont, M. Vaille, P. Gibart, Microstructure of GaN epitaxial films at different stages of the growth process on sapphire (0 0 0 1), *J. Cryst. Growth* **173**, 249–259 (1997).

181. P. Vennéguès, B. Beaumont, M. Vaille, P. Gibart, Study of open-core dislocations in GaN films on (0001) sapphire, *Appl. Phys. Lett.* **70**, 2434 (1997).

182. Z. Liliental-Weber, Y. Chen, S. Ruvimov, J. Washburn, Nanotubes and Pinholes in GaN and their Formation Mechanism, *Mater. Sci. Forum* **258-263**, 1659–1664 (1997).

183. W. Qian *et al.*, Open-core screw dislocations in GaN epilayers observed by scanning force microscopy and high-resolution transmission electron microscopy, *Appl. Phys. Lett.* **67**, 2284 (1995).

184. J. Rouviere, M. Arlery, B. Daudin, G. Feuillet, O. Briot, Transmission electron microscopy structural characterization of GaN layers grown on (0001) sapphire, *Mater. Sci. Eng. B* **50**, 61–71 (1997).

185. P. Vennegues *et al.*, Influence of high Mg doping on the microstructural and optoelectronic properties of GaN, *Mater. Sci. Eng. B* **93**, 224–228 (2002).

186. P. Vennéguès *et al.*, Atomic structure of pyramidal defects in Mg-doped GaN, *Phys. Rev. B* **68**, 1–8 (2003).

187. Z. Liliental-Weber *et al.*, Ordering in bulk GaN:Mg samples: defects caused by Mg doping, *Phys. B Condens. Matter* **273-274**, 124–129 (1999).

188. Z. Liliental-Weber *et al.*, Mg-doped GaN: Similar defects in bulk crystals and layers grown on Al[sub 2]O[sub 3] by metal–organic chemical-vapor deposition, *Appl. Phys. Lett.* **75**, 4159 (1999).

189. Z. Liliental-Weber *et al.*, Influence of Dopants on Defect Formation in GaN, *Phys. Status Solidi* **228**, 345–352 (2001).

190. Z. Liliental-Weber, T. Tomaszewicz, D. Zakharov, J. Jasinski, M. O'Keefe, Atomic Structure of Defects in GaN:Mg Grown with Ga Polarity, *Phys. Rev. Lett.* **93**, 1–4 (2004).

191. H. Morkoc, private communication.

192. B. Beaumont *et al.*, A Two-Step Method for Epitaxial Lateral Overgrowth of GaN, *Phys. Status Solidi* **176**, 567–571 (1999).

193. P. Gibart, Metal organic vapour phase epitaxy of GaN and lateral overgrowth, *Reports Prog. Phys.* **67**, 667–715 (2004).

194. M. Ali *et al.*, Void shape control in GaN re-grown on hexagonally patterned mask-less GaN, *J. Cryst. Growth* **315**, 188–191 (2011).

195. S. Bals, S. Van Aert, G. Van Tendeloo, D. Ávila-Brande, Statistical estimation of atomic positions from exit wave reconstruction with a precision in the picometer range, *Phys. Rev. Lett.* **96**, 096106 (2006).

196. K. Kimoto *et al.*, Local crystal structure analysis with several picometer precision using scanning transmission electron microscopy, *Ultramicroscopy* **110**, 778–782 (2010).

197. Y.-M. Kim *et al.*, Probing oxygen vacancy concentration and homogeneity in solid-oxide fuel-cell cathode materials on the subunit-cell level, *Nat. Mater.* **11**, 888–94 (2012).

198. B. Berkels *et al.*, Optimized imaging using non-rigid registration, *Phys. Rev. X (under Rev.* (2013).

199. J. Modersitzki, *Numerical Methods for Image Registration* (Oxford University Press, 2004).

200. J. Fischer, B., Modersitski, Fast diffusion registration, *M. Z. Nashed, O. Scherzer (Eds.), AMS Spec. Sess. Interact. Inverse Probl. Image Anal. Inverse Probl. Image Anal. Med. Imaging* **313**, 117–127 (2002).

201. W. Briggs, *A Multigrid Tutorial* (Society for Industrial and Applied Mathematics, Philadelphia, 1987).

202. W. Hackbusch, *Multigrid Methods and Applications* (Springer-Verlag, Berlin, 1985).

203. L. Jones, P. D. Nellist, STEM image post-processing for instability and aberration correction for transfer function extension, *J. Phys. Conf. Ser.* **371**, 012001 (2012).

204. N. Braidy, Y. Le Bouar, S. Lazar, C. Ricolleau, Correcting scanning instabilities from images of periodic structures, *Ultramicroscopy* **118**, 67–76 (2012).

205. D. G. Morgan, Q. M. Ramasse, N. D. Browning, Application of two-dimensional crystallography and image processing to atomic resolution Z-contrast images, *J. Electron Microsc. (Tokyo).* **58**, 223–244 (2009).

206. A. Sanchez *et al.*, An approach to the systematic distortion correction in aberration-corrected HAADF images, *J. Microsc.* **221**, 1–7 (2006).

207. A. F. Brilot *et al.*, Beam-induced motion of vitrified specimen on holey carbon film, *J. Struct. Biol.* **177**, 630–637 (2012).

208. J. Tersoff, New empirical approach for the structure and energy of covalent systems, *Phys. Rev. B* **37**, 6991–7000 (1988).

209. B. Farid, R. W. Godby, Cohesive energies of crystals, *Phys. Rev. B* **43**, 248–250 (1991).

210. M. Mostoller, M. F. Chisholm, T. Kaplan, New Extended Point Defect Structure in Diamond Cubic Crystals, *Phys. Rev. Lett.* **72**, 1494–1497 (1994).

211. Resolution refers to the smallest distance between two objects in an image at which the objects appear distinct. Precision is the statistical spread of repeated distance measurements in an image.

212. C. Kisielowski, B. Freitag, X. Xu, S. P. Beckman, D. Chrzan, Sub-angstrom imaging of dislocation core structures : how well are experiments comparable with theory ?, *Philos. Mag.* **89**, 4575–4588 (2006).

213. C. L. Jia, L. Houben, a. Thust, J. Barthel, On the benefit of the negative-spherical-aberration imaging technique for quantitative HRTEM, *Ultramicroscopy* **110**, 500–505 (2010).

214. C.-L. Jia *et al.*, Atomic-scale study of electric dipoles near charged and uncharged domain walls in ferroelectric films, *Nat. Mater.* **7**, 57–61 (2008).

215. M. Saito *et al.*, Local crystal structure analysis with 10-pm accuracy using scanning transmission electron microscopy., *J. Electron Microsc. (Tokyo).* **58**, 131–136 (2009).

216. X. Sang, J. M. LeBeau, Revolving scanning transmission electron microscopy: correcting sample drift distortion without prior knowledge., *Ultramicroscopy* **138**, 28–35 (2014).

217. L. Houben, A. Thust, K. Urban, Atomic-precision determination of the reconstruction of a 90 degree tilt boundary in YBa2Cu3O7-delta by aberration corrected HRTEM, *Ultramicroscopy* **106**, 200–214 (2006).

218. K. Kimoto *et al.*, Local crystal structure analysis with several picometer precision using scanning transmission electron microscopy., *Ultramicroscopy* **110**, 778–782 (2010).

219. R. Hovden, H. L. Xin, D. a. Muller, Channeling of a subangstrom electron beam in a crystal mapped to two-dimensional molecular orbitals, *Phys. Rev. B* **86**, 195415 (2012).

220. P. J. E. Aldred, M. Hart, The electron distribution in silicon II . Theoretical interpretation, *Proc. R. Soc. Lond. A. Math. Phys. Sci.* **332**, 239–254 (1973).

221. R. F. Loane, P. Xu, J. Silcox, Thermal vibrations in convergent-beam electron diffraction, *Acta Crystallogr. Sect. A Found. Crystallogr.* **47**, 267–278 (1991).

222. Y. Peng, P. Nellist, S. Pennycook, HAADF-STEM imaging with sub-angstrom probes: a full Bloch wave analysis, *J. Electron Microsc. (Tokyo).* **53**, 257–266 (2004).

223. C. L. Jia *et al.*, Determination of the 3D shape of a nanoscale crystal with atomic resolution from a single image., *Nat. Mater.* **13**, 1044–9 (2014).

224. S. J. L. Billinge, I. Levin, The problem with determining atomic structure at the nanoscale, *Science (80-.).* **316**, 561–565 (2007).

225. S. J. L. Billinge, The nanostructure problem, *Physics (College. Park. Md).* **3**, 25 (2010).

226. M. Schrinner *et al.*, Single Nanocrystals of Platinum Prepared by Partial Dissolution of Au-Pt Nanoalloys, *Science (80-.).* **323**, 617–620 (2009).

227. V. Mazumder, Y. Lee, S. Sun, Recent Development of Active Nanoparticle Catalysts for Fuel Cell Reactions, *Adv. Funct. Mater.* **20**, 1224–1231 (2010).

228. Y. Zhou *et al.*, Enhancement of Pt and Pt-alloy fuel cell catalyst activity and durability via nitrogen-modified carbon supports, *Energy Environ. Sci.* **3**, 1437–1446 (2010).

229. Y. Sun, L. Zhuang, J. Lu, X. Hong, P. Liu, Collapse in crystalline structure and decline in catalytic activity of Pt nanoparticles on reducing particle size to 1 nm., *J. Am. Chem. Soc.* **129**, 15465–15467 (2007).

230. T. Ahmadi, Z. Wang, T. Green, A. Henglein, M. El-Sayed, Shape-Controlled Synthesis of Colloidal Platinum Nanoparticles, *Science (80-.).* **272**, 1924–1926 (1996).

231. R. Narayanan, M. a El-Sayed, Changing catalytic activity during colloidal platinum nanocatalysis due to shape changes: electron-transfer reaction, *J. Am. Chem. Soc.* **126**, 7194–7195 (2004).

232. R. Narayanan, M. a. El-Sayed, Effect of Catalytic Activity on the Metallic Nanoparticle Size Distribution: Electron-Transfer Reaction between Fe(CN) 6 and Thiosulfate Ions Catalyzed by PVP−Platinum Nanoparticles, *J. Phys. Chem. B* **107**, 12416–12424 (2003).

233. R. Narayanan, M. a. El-Sayed, Shape-Dependent Catalytic Activity of Platinum Nanoparticles in Colloidal Solution, *Nano Lett.* **4**, 1343–1348 (2004).

234. J. Greeley, J. K. Nørskov, M. Mavrikakis, Electronic structure and catalysis on metal surfaces, *Annu. Rev. Phys. Chem.* **53**, 319–348 (2002).

235. J. Norskov, M. Scheffler, H. Toulhoat, Density functional theory in surface science and heterogeneous catalysis, *MRS Bull.* **31**, 669–674 (2006).

236. P. Juhás, D. M. Cherba, P. M. Duxbury, W. F. Punch, S. J. L. Billinge, Ab initio determination of solid-state nanostructure., *Nature* **440**, 655–8 (2006).

237. M. J. Cliffe, M. T. Dove, D. A. Drabold, A. L. Goodwin, Structure Determination of Disordered Materials from Diffraction Data, *Phys. Rev. Lett.* **104**, 125501 (2010).

238. S. Van Aert, K. J. Batenburg, M. D. Rossell, R. Erni, G. Van Tendeloo, Three-dimensional atomic imaging of crystalline nanoparticles, *Nature* **470**, 374–377 (2011).

239. J. M. LeBeau, S. D. Findlay, L. J. Allen, S. Stemmer, Standardless atom counting in scanning transmission electron microscopy, *Nano Lett.* **10**, 4405–4408 (2010).

240. M. C. Scott *et al.*, Electron tomography at 2.4-ångström resolution., *Nature* **483**, 444–7 (2012).

241. A. B. Yankovich *et al.*, Picometre-precision analysis of scanning transmission electron microscopy images of platinum nanocatalysts., *Nat. Commun.* **5**, 4155 (2014).

242. A. B. Yankovich, B. Berkels, W. Dahmen, P. Binev, P. M. Voyles, High-precision scanning transmission electron microscopy at coarse pixel sampling for reduced electron dose, *Adv. Struct. Chem. Imaging* **1**, 5 (2015).

243. S. D. Jackson *et al.*, Supported metal catalysts: preparation, characterization, and function, *J. Catal.* **139**, 191–206 (1993).

244. K. P. Bohnen, K. M. Ho, Structure and dynamics at metal surfaces, *Surf. Sci. Rep.* **19**, 99–120 (1993).

245. T. Zambelli, J. Wintterlin, J. Trost, G. Ertl, Identification of the “Active Sites” of a Surface-Catalyzed Reaction, *Science (80-.).* **273**, 1688–1690 (1996).

246. M. W. Finnis, V. Heine, Theory of lattice contraction at aluminium surfaces, *J. Phys. F Met. Phys.* **4**, L37–L41 (1974).

247. R. Smoluchowski, Anisotropy of the electronic work function of metals, *Phys. Rev.* **60**, 661–674 (1941).

248. L. Pauling, Atomic Radii and Interatomic Distances in Metals, *J. Am. Chem. Soc.* **69**, 542–553 (1947).

249. L. C. Gontard *et al.*, Aberration-corrected imaging of active sites on industrial catalyst nanoparticles, *Angew. Chemie* **46**, 3683–3685 (2007).

250. L. Y. Chang, A. S. Barnard, L. C. Gontard, R. E. Dunin-Borkowski, Resolving the structure of active sites on platinum catalytic nanoparticles, *Nano Lett.* **10**, 3073–3076 (2010).

251. W. J. Huang *et al.*, Coordination-dependent surface atomic contraction in nanocrystals revealed by coherent diffraction, *Nat. Mater.* **7**, 308–313 (2008).

252. L.-M. Peng, G. Ren, S. L. Dudarev, M. J. Whelan, Debye–Waller Factors and Absorptive Scattering Factors of Elemental Crystals, *Acta Crystallogr. Sect. A Found. Crystallogr.* **52**, 456–470 (1996).

253. P. M. Ajayan, L. D. Marks, Evidence for sinking of small particles into substrates and implications for heterogeneous catalysis, *Nature* **338**, 139–141 (1989).

254. S. Bals, S. Van Aert, G. Van Tendeloo, D. Ávila-Brande, Statistical Estimation of Atomic Positions from Exit Wave Reconstruction with a Precision in the Picometer Range, *Phys. Rev. Lett.* **96**, 096106 (2006).

255. W. J. Huang *et al.*, Coordination-dependent surface atomic contraction in nanocrystals revealed by coherent diffraction., *Nat. Mater.* **7**, 308–313 (2008).

256. a. J. D'Alfonso, B. Freitag, D. Klenov, L. J. Allen, Atomic-resolution chemical mapping using energy-dispersive x-ray spectroscopy, *Phys. Rev. B* **81**, 2–5 (2010).

257. G. Kothleitner *et al.*, Quantitative Elemental Mapping at Atomic Resolution Using X-Ray Spectroscopy, *Phys. Rev. Lett.* **112**, 085501 (2014).

258. P. Longo, P. Thomas, A. Aitouchen, B. Schaffer, R. D. Twesten, Simultaneous EELS/EDS Composition Mapping at Atomic Resolution Using Fast STEM Spectrum-Imaging, *Micros. Today* **21**, 36–40 (2013).

259. P. Lu, L. Zhou, M. J. Kramer, D. J. Smith, Atomic-scale chemical imaging and quantification of metallic alloy structures by energy-dispersive X-ray spectroscopy., *Sci. Rep.* **4**, 3945 (2014).

260. P. Lu, J. Xiong, M. Van Benthem, Q. X. Jia, Atomic-scale chemical quantification of oxide interfaces using energy-dispersive X-ray spectroscopy, *Appl. Phys. Lett.* **102** (2013).

261. H. S. Von Harrach *et al.*, An integrated Silicon Drift Detector System for FEI Schottky Field, **15**, 8–9 (2009).

262. P. Schlossmacher, D. O. Klenov, B. Freitag, H. S. von Harrach, Enhanced Detection Sensitivity with a New Windowless XEDS System for AEM Based on Silicon Drift Detector Technology, *Micros. Today* **18**, 14–20 (2010).

263. F. Azough, D. Kepaptsoglou, Q. M. Ramasse, B. Schaffer, R. Freer, On the Origin of Nanochessboard Superlattices in A-Site-Deficient Ca-Stabilized Nd 2/3 TiO 3, *Chem. Mater.* **27**, 497–507 (2015).

264. R. A. De Souza *et al.*, Electrical and Structural Characterization of a Low-Angle Tilt Grain Boundary in Iron-Doped Strontium Titanate, *J. Am. Ceram. Soc.* **86**, 922–928 (2003).

265. T. Zhao *et al.*, Highly conductive Nb doped SrTiO epitaxial thin " lms grown by laser molecular beam epitaxy, *J. Cryst. Growth* **212**, 451–455 (2000).

266. K. M. Orito, T. S. Uzuki, S. S. Ekiguchi, H. O. Kushi, M. F. Ujimoto, Electrical Characterization of SrTiO 3 Thin Films Grown on Nb-Doped SrTiO 3 Single Crystals, *Jpn. J. Appl. Phys.* **39**, 166–171 (2000).

267. A. B. Yankovich *et al.*, Thickness variations and absence of lateral compositional fluctuations in aberration-corrected STEM images of InGaN LED active regions at low dose., *Microsc. Microanal.* **20**, 864–8 (2014).